Université du Québec
Institut National de la Recherche Scientifique
Centre des matériaux, de l'énergie et des télécommunications

Contribution Piézoélectrique au Processus de Dégradation Catalytique des Colorants Organiques à l'aide de Nanoparticules de Catalyseurs $BaTiO_3$

Par

Hossein Kalhori

Thèse présentée pour l'obtention du grade de Philosophiae Doctor (Ph.D.)
en sciences de Énergie et Matériaux

Jury d'évaluation

Président du jury	Prof. Daniel Guay
et examinateur interne	Institut National de la Recherche Scientifique
Examinateur externe	Prof. Luc Stafford
	Université de Montréal
Examinateur externe	Prof. Zuo-Guang Ye
	Simon Fraser University
Directeur de recherche	Prof. Alain Pignolet
	Institut National de la Recherche Scientifique
Codirecteur de recherche	Prof. Andreas Ruediger
	Institut National de la Recherche Scientifique

Acknowledgements

I would like to take this opportunity to express my deepest gratitude to the remarkable individuals who have played a significant role in the successful completion of my PhD thesis at INRS-EMT center. First and foremost, I would like to thank my loving wife, Akram. Your unwavering support, understanding, and encouragement have been my rock throughout this challenging journey. Your belief in me, even during moments of self-doubt, has been a constant source of inspiration. I am truly blessed to have you by my side.

I extend my heartfelt appreciation to my dedicated supervisors, Prof. Alain Pignolet and Prof. Andreas Ruediger. Your extensive knowledge, guidance, and unwavering support have been instrumental in shaping the outcome of my research. I am grateful for your commitment to my academic and personal growth, and for pushing me to strive for excellence. I am immensely grateful to the members of my jury, Prof. Daniel Guay, Prof. Luc Stafford, and Prof. Zuo-Guang Ye, for their invaluable contributions to my thesis evaluation. Your expertise, insightful feedback, and constructive criticism have significantly enhanced the quality and rigor of my work. I am honored to have received your guidance and appreciate the time and effort you dedicated to evaluating my research.

I would also like to extend my thanks to my esteemed colleagues, Dr. Catalin Harnagea, Dr. Ifeanyichukwu Amaechi, Dr. Thameur Hajlaoui, Dr. Andreas Doerfler, Dr. Azza Hadj Youssef, and Mr. Mohammad Bakhtbidar. Your collaboration, stimulating discussions, and camaraderie have enriched my research experience. I am grateful for the knowledge-sharing and support we have provided to one another. Furthermore, I would like to acknowledge the faculty, staff, and administration of INRS-EMT center for providing a conducive research environment and for their unwavering support throughout my academic journey. Your commitment to excellence has been instrumental in shaping my growth as a researcher.

Lastly, I would like to express my gratitude to all the friends, family members, and loved ones who have supported and encouraged me along this challenging path. Your belief in my abilities and your unwavering encouragement have been invaluable to me.

To each and every person mentioned above, and to those who have supported me in ways beyond words, I extend my heartfelt gratitude. Your contributions have been pivotal in my achievement, and I am forever grateful for the impact you have had on my life and my research.

With deepest appreciation,
Hossein Kalhori

RÉSUMÉ

Les fournisseurs d'eau du monde entier sont confrontés à un double défi : une demande croissante ainsi qu'une diminution de l'approvisionnement en eau et de sa qualité. Les approches innovantes sont de plus en plus prisées pour protéger l'environnement des différents contaminants industriels ainsi que pour améliorer les méthodes physiques, chimiques et biologiques de traitement des eaux usées déjà employées. Les nanoparticules piézoélectriques ont récemment été proposées comme catalyseurs pour le traitement des eaux usées. Nous montrons que l'activité catalytique observée n'est pas entièrement expliquée par l'effet piézoélectrique des nanoparticules. Étant donné que les ultrasons (en tant que source typique d'énergie mécanique) stimulent généralement les réactions catalytiques, telles que la sonocatalyse et la tribocatalyse, les réactions piézocatalytiques devraient avoir lieu simultanément. Bien que la catalyse à base piézoélectrique ait fait l'objet de recherches utilisant une variété de matériaux piézoélectriques, sa capacité à distinguer la tribocatalyse ou la sonocatalyse omniprésente n'en est qu'à ses débuts. Ceci soulève des inquiétudes quant à la valeur de la contribution piézoélectrique supplémentaire. Pour distinguer les effets sono-tribo et piézocatalytiques, la première section de ce travail examine les activités catalytiques du titanate de baryum piézoélectrique ($BaTiO_3$) et du dioxyde de titane non piézoélectrique (TiO_2). Pour mieux apprécier la fonction que jouent les différents paramètres physiques dans l'activité catalytique du $BaTiO_3$, il est utile de comparer les performances catalytiques du $BaTiO_3$ et du TiO_2 à différentes concentrations et températures. Dans la deuxième section, l'effet de la température est étudié comme un paramètre clé pour distinguer la contribution piézoélectrique dans les activités catalytiques du $BaTiO_3$, et ce, en raison de son piézopotentiel dépendant de la température. Pour ce faire, nous comparons les propriétés catalytiques des nano- et microparticules de titanate de baryum piézoélectrique ($BaTiO_3$) inférieurs à et avoisinants la température à laquelle la structure cristalline passe de la phase tétragonale piézoélectrique à basse température à la phase cubique non piézoélectrique à haute température. Dans le matériau massif (bulk), la transition de phase a lieu à une température d'environ 120 °C. Cependant, plus la taille des particules diminue, plus la température de transition baisse.

Différentes techniques de caractérisation ont été appliquées pour mieux comprendre les propriétés physiques et chimiques de ce processus. La morphologie et la phase cristalline des

nanoparticules ont été caractérisées en utilisant respectivement la microscopie électronique à transmission (MET) et la diffraction des rayons X (DRX). La température de transition de la phase ferroélectrique peut être calculée grâce à la spectroscopie Raman en fonction de la température, qui offre davantage d'informations sur les caractéristiques nano- et microstructurelles, car les paramètres et grandeurs piézoélectriques et la dynamique du réseau sont étroitement liées. Après le traitement par ultrasons de solutions auxquelles sont ajoutées des particules piézoélectriques dispersées de $BaTiO_3$ comme catalyseurs, l'absorbance optique des solutions contenant un polluant modèle, soit le méthylorange, a été contrôlée pour mesurer l'activité catalytique pour dégrader le méthylorange des nanoparticules de $BaTiO_3$. Les voies chimiques de la dégradation des colorants organiques ont été étudiées en utilisant des capteurs ainsi que la chromatographie liquide couplée à la spectrométrie de masse (LC-MS). En utilisant cette approche, nous démontrons qu'alors que la sonocatalyse (et la tribocatalyse) représente(nt) 10% de la réaction catalytique des nanoparticules de $BaTiO_3$, l'autre 90% de l'activité catalytique totale est attribué à leur contribution piézocatalytique.

Mots-clés: Nanoparticules de $BaTiO_3$, Piézocatalyse, Sonocatalyse, Traitement des eaux usées, Spectroscopie Raman, Dégradation des colorants.

ABSTRACT

Water suppliers around the world are faced with a dual challenge from rising demand and declining water supply and quality. Innovative approaches are increasingly appreciated to protect the environment from different industrial contaminants and to enhance the already used physical, chemical, and biological wastewater treatment methods. Piezoelectric nanoparticles have recently been proposed as catalysts for wastewater treatment. We show that the observed catalytic activity may not entirely be explained by the piezoelectric effect of nanoparticles. Due to the fact that ultrasonication (as a typical source of mechanical energy) typically stimulates catalytic reactions, such as sonocatalysis and tribocatalysis, piezocatalytic reactions should take place concurrently. Although piezoelectric-based catalysis has been researched utilising a variety of piezoelectric materials, its ability to discriminate against the omnipresent tribocatalysis or sonocatalysis is still in its infancy, raising concerns about the value of the additional piezoelectric contribution. To distinguish between sono-tribo- and piezocatalytic effects, the first section of this work looks at the catalytic activities of both piezoelectric barium titanate ($BaTiO_3$) and non-piezoelectric titanium dioxide (TiO_2). To better appreciate the function that various physical parameters play in the catalytic activity of $BaTiO_3$, it is helpful to compare the catalytic performance of $BaTiO_3$ and TiO_2 at different concentrations and temperatures. In the second section, the temperature effect is investigated as a key parameter to distinguish the piezoelectric contribution in the catalytic activities of $BaTiO_3$ owing to its temperature dependent piezopotential. In order to do this, we compare the catalytic properties of nano- and microparticles of piezoelectric barium titanate ($BaTiO_3$) below and close to the temperature at which the crystalline structure switches from the lower-temperature tetragonal, piezoelectric phase to the higher-temperature cubic, non-piezoelectric phase. In bulk, the phase transition takes place at a temperature of roughly 120 ^oC, but as the particle size decreases, the transition temperature drops.

Different characterization techniques were applied to better understand the physical and chemical properties in this process. The morphology and crystal phase of the nanoparticles were characterised using transmission electron microscopy (TEM) and X-ray diffraction (XRD), respectively. The ferroelectric phase transition temperature may be calculated thanks to temperature-dependent Raman spectroscopy, which offers even more information into the nano-

and microstructural features because the piezoelectric capabilities and the lattice dynamics are tightly connected. After ultrasonically processing the solution and adding the dispersed piezoelectric $BaTiO_3$ particles as catalysts, the optical absorbance of a solution containing the model pollutant methyl orange was monitored to measure the $BaTiO_3$ nanoparticles' catalytic activity. The chemical pathways of the organic dye degradations were studied using scavengers as well as the liquid chromatography mass spectrometry (LC-MS). Using this approach, we demonstrate that whereas sonocatalysis (and tribocatalysis) account for 10% of the catalytic reaction of $BaTiO_3$, the remaining 90% of the total catalytic activity is attributed to the piezocatalytic contribution.

Keywords: $BaTiO_3$ nanoparticles, Piezocatalysis, Sonocatalysis, Waste water treatment, Raman spectroscopy, Dye degradation

Sommaire en français

1- Introduction

L'approvisionnement en eau potable et le traitement des eaux usée font face à d'énormes défis avec une demande, mais aussi une pollution qui ne cesse de croître. Des approches innovantes sont de plus en plus prisées pour protéger l'environnement des différents contaminants industriels ainsi que pour améliorer les méthodes physiques, chimiques et biologiques de traitement des eaux usées déjà employées. Les nanoparticules de matériaux piézoélectriques ont récemment été proposées comme catalyseurs pour le traitement des eaux usées. Étant donné que d'autres réactions catalytiques, telles que la sonocatalyse et la tribocatalyse, peuvent avoir lieu conjointement avec les réactions piézocatalytiques lorsque soumis à des ultrasons, l'activité catalytique observée des nanoparticules de matériaux piézoélectriques n'est pas entièrement expliquée par le seul effet piézoélectrique et la contribution réelle des propriétés piézoélectriques n'a jamais été vraiment clairement déterminée. Dans ce sommaire, les résultats expérimentaux obtenus au cours de ce projet sont présentés et discutés en détail, avec pour but d'atteindre notre objectif, soit, de déterminer la contribution des propriétés piézoélectriques durant le processus de sono-piézocatalyse. Dans la prochaine section, les activités sono-piézocatalytiques de poudres de $BaTiO_3$ tétragonal piézoélectrique et de poudres de TiO_2 anatase non-piézoélectrique sont présentées, discutées et comparées. Les différences entre ces deux matériaux dont les surfaces catalytiquement actives sont similaires (l'un est piézoélectrique tandis que l'autre ne l'est pas) constituent un premier pas vers notre objectif. Comme discuté dans le deuxième chapitre de la thèse, la taille et la température sont deux facteurs importants qui contrôlent la nature piézoélectrique ou non du $BaTiO_3$ et qui déterminent sa structure crystalline soit dans sa phase ferroélectrique et piézoélectrique tétragonale ou dans sa phase paraélectrique cubique. Dans la section suivante, les effets de la température et de la taille des particules de $BaTiO_3$ sur le

potentiel piézoélectrique ou piézopotentiel sont discutés. Enfin, dans la dernière section, les résultats expérimentaux décrivant l'effet de la température et les effets de taille des nanoparticules de $BaTiO_3$, vialeur piézopotentiel, sur leur activité piézocatalytique sont présentés et discutés en détail. Finalement, quelques conclusions concernant les contributions relatives de la sonocatalyse et de la piézocatylyse lorsque des nanoparticules piézoélectriques de $BaTiO_3$ sont utilisées comme catalyseurs en sont déduites.

2- Activités catalytiques du $BaTiO_3$ et du TiO_2

Les récents efforts de recherche sur la piézocatalyse semblent avoir négligé d'analyser les contributions omniprésentes des processus sono- et tribocatalytiques. Lors de l'évaluation de l'activité catalytique des nanoparticules (NPs) piézoélectriques utilisées comme catalyseurs, la piézocatalyse, la sonocatalyse et même la tribocatalyse devraient se produire simultanément. Pour distinguer la tribocatalyse, la sonocatalyse et la piézocatalyse dans le processus catalytique de dégradation du méthylorange (MO) par ultrasonication en solution aqueuse, et pour quantifier la contribution piézoélectrique réelle à l'activité catalytique des nanoparticules de $BaTiO_3$, nous étudions et comparons les activités catalytiques de nanoparticules de mêmes tailles (100 nm) de la phase anatase du TiO_2 (matériau non piézoélectrique) et de $BaTiO_3$ (matériau ferroélectrique typique qui a des propriétés piézoélectriques amplement étudiée et bien connues). Notons ici que ces deux matériaux ont tous les deux une structure cristalline tétragonale (la phase anatase du TiO_2 possède en effet une structure tétragonale).

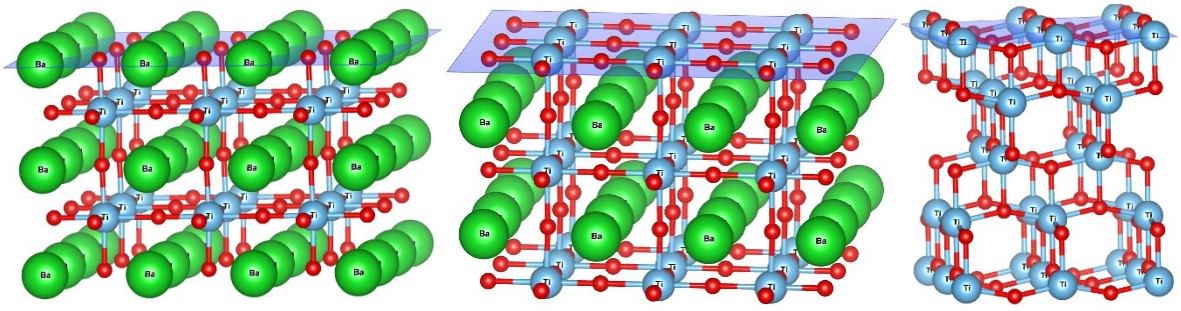

(a) (b) (c)

Figure 1 Schéma de la surface externe tétragonale du $BaTiO_3$ lorsque (a) le baryum et l'oxygène, (b) le titane et l'oxygène, constituent la dernière couche atomique de la surface (indépendamment des atomes d'oxygène qui sont présents dans les deux cas), et (c) la structure cristalline anatase TiO_2, qui a la même surface de terminaison que le $BaTiO_3$ lorsqu'elle est terminée par Ti et O, comme indiqué dans (b).

Le $BaTiO_3$ peut être vu structurellement comme deux sous-réseaux alternés de BaO et de TiO_2. Les surfaces du $BaTiO_3$ sont terminées soit par le sous-réseau de BaO, soit par le sous-réseau de TiO_2. (Figure 1 (a & b). Les surfaces de BaO ne présentent que peu ou pas d'activité catalytique (elles sont catalytiquement inactives, car la surface de BaO réagit facilement avec les contaminants environnementaux tels que le CO_2, ce qui donne du $BaCO_3$, totalement inactif pour de telles réactions catalytiques) [1]. Les seules surfaces du $BaTiO_3$ pouvant présenter une activité catalytique sont donc les surfaces terminées par le sous-réseau de TiO_2, avec une surface similaire à celle de TiO_2 anatase. Par conséquent, le TiO_2 peut donc être considéré comme le matériau *non-piézoélectrique* dont la structure atomique et l'activité catalytique est la plus proche de celle du $BaTiO_3$ *piézoélectrique*. De plus, comme les deux matériaux ont une bande interdite optique similaire d'environ 3,2 eV [2], leur propriétés optiques devraient être très similaires également. On s'attend donc à ce qu'ils aient des activités photocatalytiques et sonocatalytiques comparables, la seule différence significative étant que l'un de ces matériaux est piézoélectrique tandis que l'autre ne l'est pas. Nous supposons que la moitié de la surface libre des particules de $BaTiO_3$ est terminée par le baryum et l'oxygène, tandis que le reste de la surface libre est terminé par le titane et l'oxygène. Avec ces hypothèses, il est supposé que l'activité catalytique des surfaces libres <u>active</u> des nanoparticules de $BaTiO_3$, (donc la moitié des surface libres des nanoparticules de $BaTiO_3$) excluant la piézocatalyse, devrait être comparable à l'activité catalytique des surfaces libres des nanoparticules de TiO_2 anatase ne présentant aucune propriété piézoélectrique. La contribution des propriétés piézoélectriques du $BaTiO_3$ aux activités catalytiques du $BaTiO_3$ est donc déterminée en comparant l'activité catalytique des nanoparticules piézoélectriques de $BaTiO_3$ utilisées comme catalyseur avec celle des nanoparticules non-piézoélectriques de TiO_2 anatase utilisées comme catalyseur, dispersées en solution aqueuse et soumises à des vibrations ultrasoniques (ultrasonication). Il convient toutefois de souligner que, bien que structurellement similaires, les surfaces vicinales de titanate de baryum avec terminaison TiO_2 ne sont pas absolument identiques, ni structurellement ni électroniquement, aux surfaces de TiO_2 anatase ou rutile.

Le méthylorange (MO), un colorant organique, a été choisi comme polluant modèle dans cette étude. Il a été rapporté que les nanoparticules de $BaTiO_3$ sont chargées positivement dans un environnement au pH presque neutre [3]. Ainsi, on s'attend à ce que le MO anionique soit facilement adsorbé par les nanoparticules de $BaTiO_3$. Toutefois, pour être complet, l'efficacité de

la piézocatalyse des nanoparticules de $BaTiO_3$ a également été examinée avec un colorant cationique, à savoir la rhodamine B (RhB).

2-1 Caractérisations catalytiques

Les activités catalytiques des nanoparticules de $BaTiO_3$ et de TiO_2 ont été étudiées en suspension dans de l'eau « contaminée » par du MO en soumettant les solutions aqueuses à des vibrations ultrasoniques continues à une fréquence de 40 kHz dans un bain ultrasonique d'une puissance de 80 W. L'absorption optique d'une lumière monochromatique de longueur d'onde de 405 nm, laquelle se situe dans la bande d'absorption du MO, nous donne ensuite une indication quantitative de la décomposition de ce composé organique (plus précisément de sa concentration résiduelle dans la solution) après différents temps d'ultrasonication. En effet, plus la décomposition du MO est importante, moins il en reste dans la solution et moins l'absorption optique est importante. Notons que la disparition progressive du MO peut être évaluée même à l'œil nu, car la couleur de la solution change et devient moins intense, et finalement transparente. Les Figure 2 (a) et 2 (c) montrent les mesures d'absorption optique par spectrophotométrie UV-vis dans la gamme de longueurs d'onde de 250-640 nm et pour plusieurs temps d'ultrasonication de l'eau contaminée par du MO avec des nanoparticules de $BaTiO_3$ en suspensions comme catalyseurs, avec (Figure 2 (a)) et sans (Figure 2 (c)) la ligne de base. Il existe pour la solution contaminée avant ultrasonication un pic d'absorption à une longueur d'onde de 464 nm qui est attribué au MO. L'intensité de ce pic diminue clairement avec le temps, de sorte qu'après 3 heures, ce pic est significativement diminué. Le fait que la couleur de l'eau contaminée soit passée de l'orange clair au transparent suggère également que les nanoparticules de $BaTiO_3$ agissent effectivement comme des catalyseurs pour décomposer le colorant organique présent en solution dans l'eau. Cette figure comprend également des courbes et des images des flacons contenant la solution prises après des temps d'ultrasonication plus importants qui montrent une disparition presque complète du pic et une solution presque transparente après 6 heures, montrant ainsi de manière convaincante l'efficacité du $BaTiO_3$ pour dégrader le MO lorsque soumis à des ultrasons. Pour la solution contaminée par le MO avec les nanocatalyseurs de TiO_2 en suspension, les mêmes mesures d'absorption optique sont faites, dont les résultats ainsi que les images correspondantes des flacons contenant l'eau polluée prises après différents intervalles de

temps sont présentés dans les Figure 2 (b) et 2 (d), avec et sans la ligne de base. On voit clairement que la ligne de base des courbes d'absorption augmente avec le temps. Cela peut être une indication de la formation de sous-produits dont certains pics pourraient se superposer à celui du MO en utilisant comme catalyseurs des nanoparticules de TiO_2. Pour les estimations des concentrations résiduelles du colorant organique et donc de l'efficacité des nanocatalyseurs pour la dégradation du MO, les lignes de base (qui variaient beaucoup au cours du temps pour le cas des NPs de TiO_2 (Figure 2 (b)) ont été soustraites. La comparaison des résultats obtenus avec le $BaTiO_3$ et le TiO_2 révèle que les solutions contenant des nanoparticules de $BaTiO_3$ en suspension comme catalyseurs dégradent le MO plus rapidement et plus efficacement que celles contenant des nanoparticules de TiO_2 en suspension.

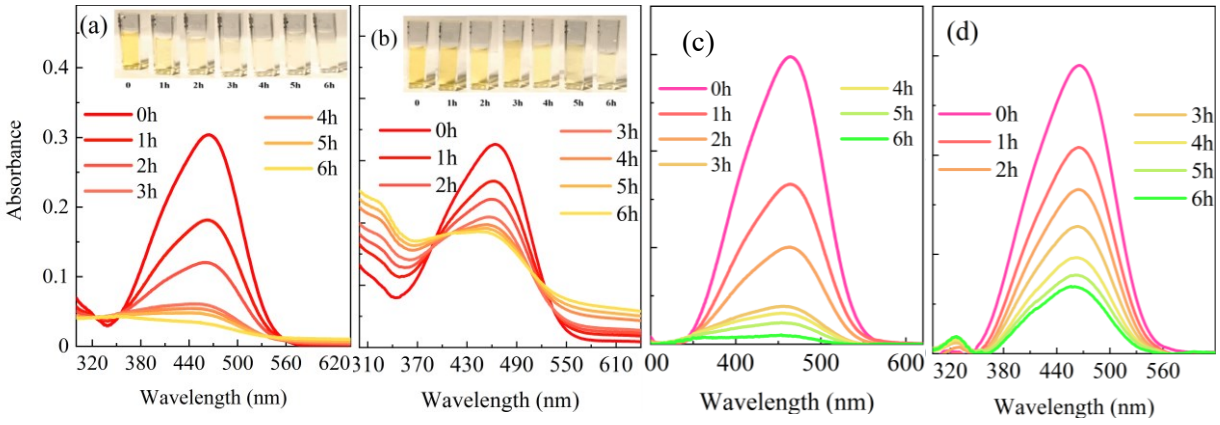

Figure 2 Spectrophotométrie UV-vis de l'eau contaminée obtenue avec (a) les nanocatalyseurs de $BaTiO_3$ et (b) de TiO_2 après différents temps de vibrations ultrasoniques, accompagnée des photographies montrant la variation des couleurs des solutions de MO après différents temps d'ultrasonication. (c) et (d) montrent les données correspondant à (a) et (b), respectivement, après que la ligne de base des graphiques a été supprimée.

Afin de confirmer et clarifier les processus de dégradation des colorants en utilisant ces deux nanomatériaux comme catalyseurs, une série d'études supplémentaires de contrôle a été réalisée. L'utilisation de la vibration ultrasonique sans catalyseur dans la solution n'entraîne pas de changement significatif de la concentration de MO. Les contaminants ne sont pas non plus réduits de manière appréciable par la simple addition de TiO_2 ou de $BaTiO_3$ à l'eau contaminée par le MO et par le simple mélange avec un agitateur magnétique sans aucune ultrasonication. Par contre, on constate que les colorants organiques comme le MO ou le RhB se dégradent et que leur concentration diminue en fonction du temps lorsque les nanoparticules de TiO_2 ou de $BaTiO_3$ sont utilisées comme agents catalytiques sous vibrations ultrasoniques, comme le montre

bien la Figure 3 (a). Le fait que le RhB soit un colorant organique cationique et que le MO soit un colorant organique anionique suggère que des résultats similaires peuvent être obtenus pour une large gamme de contaminants organiques de tous types. En utilisant les mêmes concentrations de matériaux catalytiques (0,5 g/L) pour les nanoparticules de TiO_2 et de $BaTiO_3$ dans une eau polluée par 4 mg/L de MO, il est clairement démontré qu'après 8 heures, les NPs de TiO_2 dégradent 50% du polluant MO, alors que plus de 80% du MO a été dégradé avec les NPs de $BaTiO_3$. Ces résultats montrent qu'avec les mêmes conditions ambiantes, l'efficacité catalytique des nanoparticules de $BaTiO_3$ pour décontaminer l'eau est nettement supérieure à celle du TiO_2, ce que nous attribuons aux propriétés piézoélectriques du $BaTiO_3$ et à son activité piézocatalytique.

L'efficacité de la dégradation des colorants devrait également dépendre de la concentration du catalyseur. L'efficacité catalytique en fonction de la concentration du catalyseur a été mesurée en fonction du temps pour différentes concentrations de nanopoudres de $BaTiO_3$. La dégradation du colorant augmente en effet de manière significative lorsque la concentration des NPs de $BaTiO_3$ passe de 0 à 0,5 g/L. Pour approfondir l'analyse quantitative de ces changements, nous utilisons le modèle de Langmuir-Hinshelwood souvent utilisée pour décrire les cinétiques de réaction en catalyse hétérogène. Ce modèle est ici utilisé dans la limite de faible concentration de MO et dans le cas où la réaction est limitée par la vitesse de réaction et non pas par celle d'absorption/désorption. Sous ces conditions, la constante de vitesse de réaction (K_{obs}) de la dégradation du colorant est donc décrite par l'équation suivante :

$$K_{obs} \times t = -ln\left(\frac{C_t}{C_o}\right) \qquad (1)$$

où C_0 est la concentration molaire initiale de la solution de colorant et C_t est la concentration molaire de la solution de colorant au temps t. La Figure 3 (b) montre les taux de réaction calculés pour les deux types de catalyseur à différentes concentrations. Les résultats pour $BaTiO_3$ et pour TiO_2 ont été simplement ajustés par des droites afin d'obtenir la dépendance des taux de réaction catalytique par rapport à la concentration des nanopoudres dispersées dans le liquide comme agents catalytiques. Les résultats obtenus sont des taux de réaction catalytique de 0,53 [L/g×h] et 0,22 [L/g×h] pour $BaTiO_3$ et TiO_2, respectivement. De plus, en considérant que la réaction de catalyse augmente avec la concentration des particules, il faut préciser que les concentrations utilisées dans nos expériences sont des concentrations massiques et non des concentrations

molaires et qu'en raison de leurs densités différentes, il y a un plus grand nombre de particules de TiO_2 que de particules de $BaTiO_3$ dans la solution pour une concentration massique donnée et pour une taille de particule identique. Si on corrige pour la différence de densité et qu'on exprime la constante de réaction K par particule ou mieux encore, puisque les particules ont des tailles similaires, par unité de surface réactive, les taux de réaction des NPs de TiO_2 dans la Figure 3 (b) devraient être réduits d'environ 40%, ce qui souligne encore davantage la différence d'activité catalytique entre le TiO_2 et le $BaTiO_3$, et démontre ainsi l'importance de la contribution piézocatalytique dans la dégradation du MO sous ultrasonication.

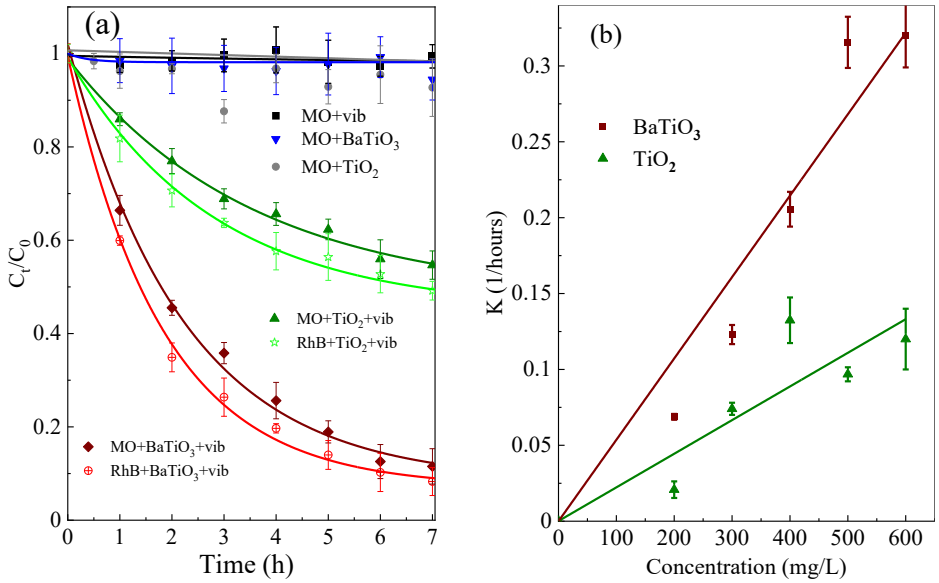

Figure 3 (a) Activités piézocatalytiques des nanoparticules de catalyseur de $BaTiO_3$ et de TiO_2 en fonction du temps pour la dégradation du MO et du RhB en solution, ainsi qu'en l'absence de catalyseur et lorsque les catalyseurs ont été agités avec l'eau contaminée sans la présence de vibration ultrasonique. (b) Cinétique de la piézo-sonodégradation du méthylorange (MO) calculée en mesurant les taux de réaction catalytique pour différentes concentrations de $BaTiO_3$ et de TiO_2.

3- Dépendance des activités catalytiques des nanoparticules de $BaTiO_3$ de leur taille et de la température

La température et la taille des nanoparticules piézoélectriques de $BaTiO_3$ sont les deux principaux paramètres affectant leurs activités piézocatalytiques ce qui est consistant avec le fait qu'il a été clairement montré que les propriétés piézoélectriques du $BaTiO_3$ dépendent fortement de ces deux paramètres [4, 5]. Dans cette étude, des poudres de $BaTiO_3$ avec trois tailles de grains différentes ont été étudiées et leurs activités catalytiques pour la dégradation du MO, un

colorant anionique bien connu, ont été caractérisées à différentes températures. La dépendance en taille et en température de l'activité catalytique devrait permettre d'évaluer la contribution des propriétés piézoélectriques à l'activité catalytique totale. Les mesures de l'activité piézocatalytique des poudres de $BaTiO_3$ sont effectuées en mesurant la décomposition des colorants organiques sous vibrations ultrasoniques en dessous du point d'ébullition de l'eau, tandis que l'évolution de la symétrie locale de ces poudres en fonction de la température a été étudiée par spectroscopie Raman dépendante de la température. Puisque la polarisation spontanée du $BaTiO_3$ est fortement dépendante de la température, surtout au voisinage de la température de transition, *et en supposant une faible dépendance à la température des autres composantes de la catalyse dans la gamme de température étudiée*, l'évolution de l'activité catalytique globale avec la température peut être utilisée pour séparer les réactions contrôlées par les propriétés piézoélectriques (piézocatalytiques) des autres réactions catalytiques possibles telles que la sonocatalyse. Dans cette section, il est montré que la dégradation piézocatalytique de polluants organiques sous ultrasons en utilisant des poudres de $BaTiO_3$ comme catalyseur dépend effectivement de la taille des grains de la poudre et présente une diminution soudaine lorsque l'on s'approche des températures de transition entre les phases ferroélectriques et paraélectriques pour la taille de grains étudiée.

3-1 Morphologie des particules

Les Figure 4 (a)-(c) montrent des images de microscopie électronique en transmission (MET) des nanoparticules de $BaTiO_3$. Pour la poudre de $BaTiO_3$ de 50 nm, les nanoparticules sont, dans une certaine mesure, monodispersées. Cependant, il y a une légère agglomération résultant de la courte durée d'ultrasonication de la poudre dispersée dans la solution. Dans le cas des nanoparticules de $BaTiO_3$ ayant des tailles de 100 nm et moins, l'image MET montre une morphologie de grain irrégulière avec une combinaison de formes cubiques et quasi-sphériques. D'après les résultats obtenus à partir des Figure 4 (a) et (b), les tailles moyennes des particules de ces deux échantillons sont estimées à 53,8±11,3 nm et 96,3±18,3 nm, respectivement. La poudre massive (*bulk powder*) est constituée de particules agglomérées, qui ont été quelque peu difficiles à disperser de manière homogène lors de l'ultrasonication. Le contraste sombre est dû à la contrainte de taille, spécifiquement au fait que les particules de taille micrométrique sont connues pour être moins transparentes au faisceau d'électrons. L'estimation de la taille moyenne des particules dans ce dernier cas est de 1,5±0,5 µm.

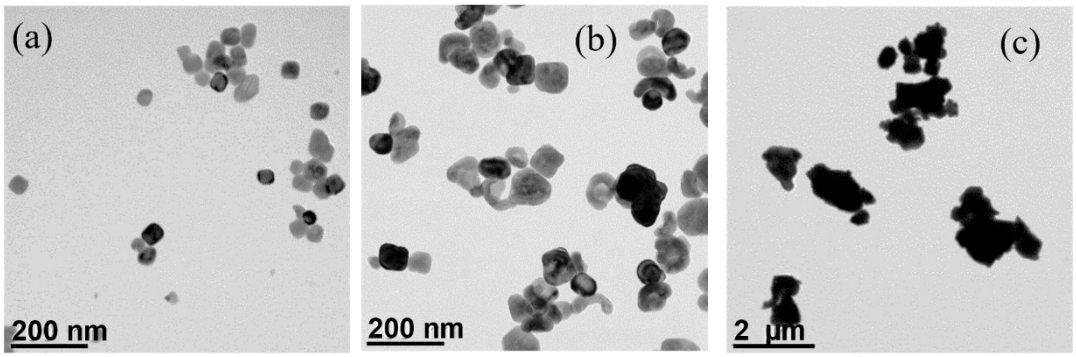

Figure 4 Micrographie MET donnant une idée de la forme des grains et de la distribution de taille relative des particules avec des tailles nominales de (a) 50 nm, (b) 100 nm, et (c) 2 µm.

3-2 Effets structurels

La diffraction des rayons X (DRX) est utilisée pour étudier la structure cristalline des poudres. Les résultats de la DRX sont présentés dans la Figure 5 (a), avec la position des pics de diffraction de rayons X principaux de la phase tétragonale du $BaTiO_3$ (JCPDS: 01- 089-1428). Les schémas de diffraction de rayons X des trois poudres de $BaTiO_3$ ayant 3 tailles de grains différentes sont similaires. La seule différence notable concerne les deux pics situés à $2\Theta = 45^o$ qui sont nettement séparés dans l'échantillon de poudre de 2 µm, et sont attribués aux plans (002) et (200), respectivement. Cette séparation révèle une distorsion tétragonale causée par un paramètre de maille hors plan *c* plus grand que le paramètre de maille dans le plan *a*. Les études théoriques suggèrent que cette distorsion tétragonale diminue avec la taille des particules [6]. En conséquence, le rapport *c* sur *a* pour chaque échantillon, qui est représentatif de la tétragonalité de sa structure cristalline, a été mesuré. Le rapport *c/a* mesuré diminue effectivement avec la taille des particules, donnant des valeurs de 1,0076 pour la poudre de 2 µm et de 1,0028 pour les particules de 50 nm. Les fonctions empiriques suivantes ont été proposées [7] pour décrire la relation entre la tétragonalité et la taille des particules :

$$\frac{c}{a}(d) = \frac{c}{a}(\infty)\left[1 - \frac{A}{d-d_1}\right] \qquad (2)$$

Dans laquelle *c/a(d)* est la tétragonalité de la structure cristalline pour une particule de taille *d*, $c/a(\infty)$ est la valeur de la tétragonalité du matériau massif (*bulk*), et A, et d_1 sont des paramètres d'ajustement. Les résultats de *c/a* en fonction de la taille des particules sont présentés à la Figure 5 (b). En considérant les ajustements, on peut dire que la tétragonalité des particules de 2 µm est proche des valeurs du matériau massif (*bulk*) rapportées dans la littérature [8]. Il est important de

noter que la diminution de *c/a* avec la taille des particules est due à la diminution du paramètre de maille *c*, qui gouverne également la diminution de la polarisation spontanée dans la structure cristalline du $BaTiO_3$. Le paramètre d'ajustement d_1 trouvé est 11,09 nm et représente, en accord avec les études précédentes, la taille critique des particules dans laquelle une polarisation spontanée peut être présente dans la structure du $BaTiO_3$ [9].

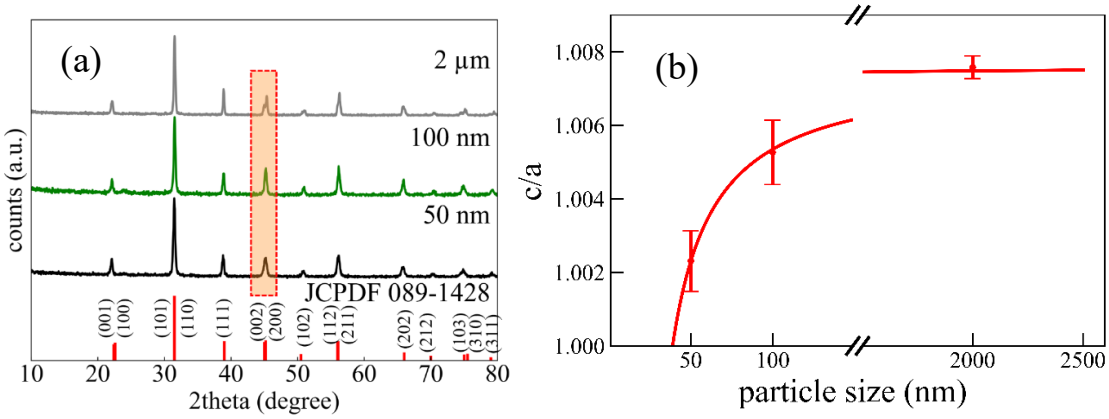

Figure 5 (a) Schémas de diffraction des rayons X de poudres de $BaTiO_3$ de différentes tailles, et (b) résultats des valeurs c/a calculées en fonction de la taille des particules.

3-3 La spectroscopie Raman

Indépendamment de leur dépendance en taille, il est bien connu que les propriétés piézoélectriques du $BaTiO_3$ dépendent fortement de la température, en particulier lorsqu'elles avoisinent la température de transition de la phase tétragonale ferroélectrique (et donc piézoélectrique) à la phase cubique paraélectrique (température de Curie T_C). L'effet de la température sur l'évolution structurelle du $BaTiO_3$ a été examiné par spectroscopie Raman. Une revue de la littérature révèle que le spectre Raman de premier ordre du $BaTiO_3$ tétragonal comprend 10 modes actifs de phonons, dont des modes optiques transversaux et longitudinaux. Ceux-ci ne tiennent pas compte de la division des modes optiques transversaux et longitudinaux, ni de la division due à la polarisation différente dans chaque direction cristallographique de la cellule unitaire (il y aurait alors 18 modes Raman actifs distincts et indépendants) [9]. Les spectres Raman de différentes tailles de poudres de $BaTiO_3$ ont été mesurés à plusieurs températures, et ce jusqu'à 140 °C, dans le but d'estimer leur température de Curie. Comme décrit dans la section précédente, les particules plus petites sont plus proches de la transition vers la phase cubique paraélectrique, et devraient donc avoir une température de transition de phase plus basse. Les données brutes Raman ont été corrigées en utilisant le facteur de correction

thermique de Bose-Einstein [10], permettant ainsi une comparaison directe des spectres obtenus à différentes températures.

$$I_C(\omega) = I(\omega)[n(\omega) + 1] \quad (3)$$

où $I_C(\omega)$ est l'intensité corrigée des spectres Raman, $I(\omega)$ est l'intensité Raman des spectres acquis expérimentalement, et $n(\omega)$ est le nombre d'occupation de Bose-Einstein (les phonons sont des bosons). $n(\omega) + 1 = \left[1 - \exp\left(-\frac{\hbar\omega}{kT}\right)\right]^{-1}$ ω étant la fréquence des phonons, T la température, et $\hbar$ et k sont les constantes de Planck et de Boltzmann, respectivement.

Les spectres Raman corrigés pour les échantillons de poudre d'une taille de 50 nm à différentes températures sont présentés dans la Figure 6 (a). On observe que les spectres Raman mesurés à température ambiante pour les poudres de 50 nm sont cohérents avec ceux rapportés dans la littérature [11]. Alors que la phase cubique de $BaTiO_3$ ne présente pas de mode Raman actifs et est dite « silencieuse », la phase tétragonale de $BaTiO_3$ présente des pics caractéristiques situés à 301 cm^{-1} et 715 cm^{-1}, qui sont attribués aux modes phonons B1 + E(TO3 + LO2) et A1 + E(LO3 + LO4), responsables de la vibration torsionnelle Ti-O dans les octaèdres de TiO_6. Les pics mesurés situés à 507 cm^{-1} sont attribués à TO3 de la symétrie A1. De plus, il y a deux pics situés à 180 cm^{-1} et 267 cm^{-1}, qui sont attribués aux modes TO1 et TO2 de la symétrie A1, respectivement. L'effet de l'augmentation de la température est clairement visible sur les modes caractéristiques susmentionnés (c'est-à-dire B1 + E et A1 + E) indiquant la tétragonalité, car l'intensité de leurs pics est réduite et élargie de manière asymétrique. La Figure 6 (b) montre l'intensité normalisée du pic (soit le rapport entre l'intensité du pic à 301 cm^{-1} et celui à 507 cm^{-1}, ce dernier étant indépendant de la température, divisé par ce même rapport d'intensité à température ambiante) pour le mode B1 + E pour chaque poudre. Comme le montre la Figure 6 (b), l'intensité diminue lorsque la température augmente. Cela indique que la phase tétragonale à température ambiante se transforme structurellement en phase cubique à haute température au-dessus d'une certaine température critique, connue sous le nom de température de Curie (T_c). Pour les poudres de 50 nm, 100 nm et 2 µm, les T_c obtenues sont respectivement de 102, 113 et 124 °C. Il faut noter ici que l'intensité normalisée du signal Raman affichée dans la Figure 6 (a) permet d'évaluer la tétragonalité de la structure de $BaTiO_3$. En effet, connaissant la distorsion cristalline à température ambiante (*c/a*), lorsque nous supposons une relation linéaire entre les

intensités de pic normalisées définies ci-dessus et *c/a*, la tétragonalité de chaque cristal à différentes températures peut être obtenue à partir des données Raman, comme indiqué dans la Figure 6 (b).

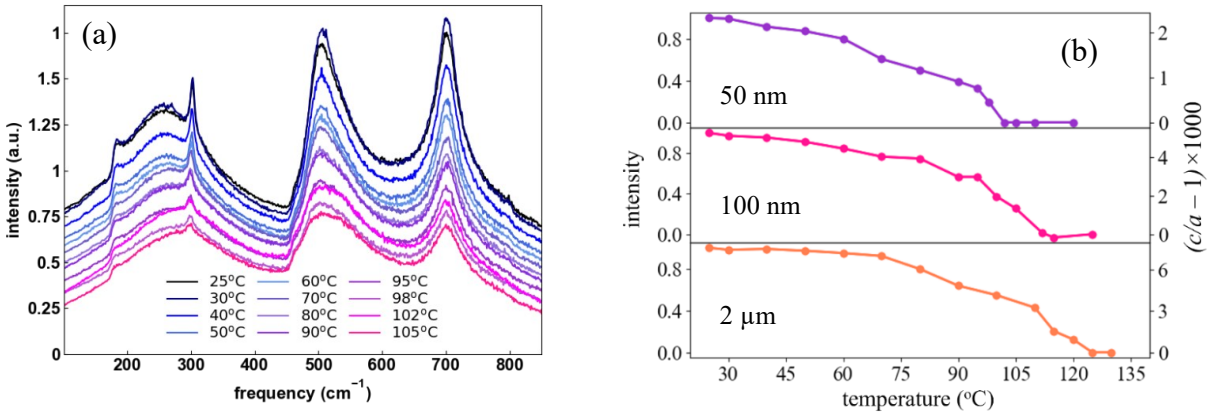

Figure 6 (a) Spectres Raman des poudres de 50 nm à différentes températures, (b) Intensité normalisée du pic de la ligne à 301 cm^{-1} à différentes températures, obtenue pour des poudres de différentes tailles.

3-4 Caractérisations de la piézocatalyse

Comme précédemment, les propriétés catalytiques assistées par ultrasons des particules de $BaTiO_3$ ont été étudiées en suivant la dégradation du méthylorange (MO), notre colorant organique modèle. La concentration des matériaux catalytiques dans chaque mesure a été fixée à 1 g/L. Selon la littérature pré-existante du domaine, cette concentration est la valeur optimale, et il a été rapporté qu'une concentration plus élevée n'améliore pas sensiblement la performance catalytique [12, 13]. Nos propres expériences confirment qu'effectivement l'augmentation de la concentration des particules de catalyseur au-delà de 1 g/L n'améliore pas significativement leur performance catalytique. Dans des expériences de contrôle, nous avons observé que l'ultrasonication sans la présence de matériau catalyseur, ainsi que la présence du matériau catalyseur sans ultrasonication n'entraînent aucun changement, et donc que la présence simultanée des ultrasons et du matériau catalyseur (par exemple les particules de $BaTiO_3$) est nécessaire pour que la réaction de décomposition des colorants organiques se produise.

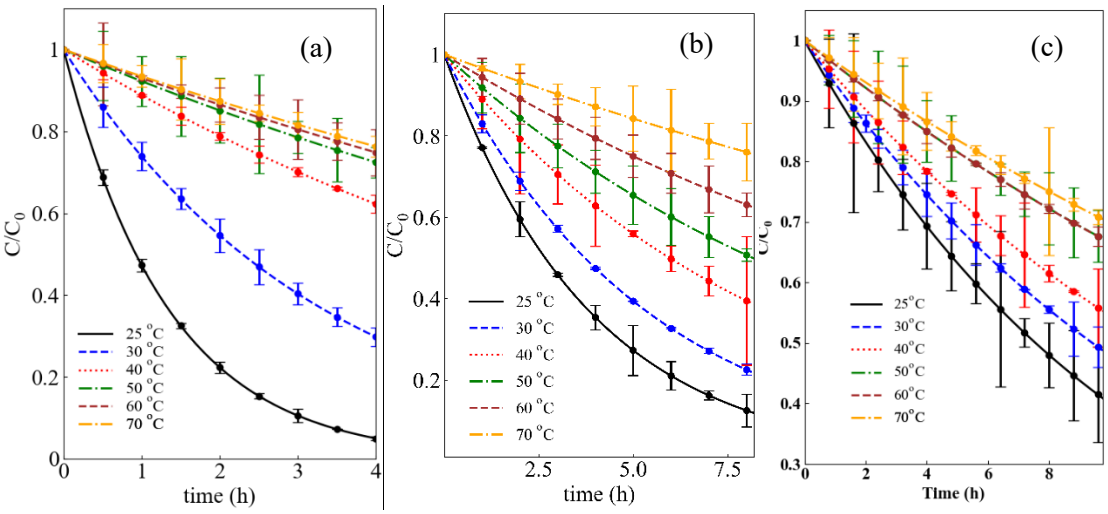

Figure 7 Dégradation du colorant methylorange après différents temps d'ultrasonication à différentes températures en utilisant comme catalyseur des poudres de $BaTiO_3$ avec une taille de (a) 50 nm, (b)100 nm et (c) 2000 nm.

L'expérience pour chaque échantillon a été réalisée à six températures différentes comprises entre 25 et 70 °C et les résultats de ces expériences sont présentés dans les Figure 7 (a)-(c). Parmi les différentes tailles de poudres de $BaTiO_3$, les échantillons avec la poudre de 50 nm montrent les meilleurs résultats de la dégradation catalytique du MO à température ambiante, tandis que les particules de $BaTiO_3$ de 2 µm donnent les plus faibles performances. En supposant une relation directe entre l'absorption de lumière et la concentration de MO présent dans la solution, on déduit que les poudre de 50 nm et 100 nm dégradent plus de 90% des colorants organiques après 4 heures d'ultrasonication (Figure 7 (a)). Il a également été observé pour tous les échantillons que le taux de dégradation des colorants diminue lorsque la température augmente. La vitesse de réaction de la dégradation du colorant a été obtenue à partir de l'équation (1). Les taux de réaction K_{obs} obtenus sont présentés dans la Figure 8 (a) en fonction de la température pour les différentes tailles de poudre. Il est marquant de constater que l'activité catalytique évaluée à partir du rapport mesuré expérimentalement (C_t/C_0) diminue de plus de 80% pour la poudre de $BaTiO_3$ de 50 nm lorsque la température augmente de 25°C à 70°C, alors que pour les poudres de $BaTiO_3$ de 2 µm et pour les poudres de $BaTiO_3$ de 100 nm, lesquelles ont des activités catalytiques beaucoup plus faibles à température ambiante, le taux de réaction (déjà faible) ne diminue pas de manière aussi radicale avec l'augmentation de la température. Les réactions de décomposition catalytique du MO par des nanoparticules de TiO_2 d'une taille de 100 nm (matériau non-piézoélectrique et couramment utilisées comme matériau catalyseur de référence

dans les réactions catalytiques) ont été étudiées et publiées dans une étude précédente de notre groupe [14]. Nous avons rapporté un meilleur taux de réaction catalytique pour la dégradation du MO sous ultrasonication pour les nanoparticules de $BaTiO_3$ que pour les nanoparticules de TiO_2 de même taille et de même morphologie. Ceci a été attribué à l'activité piézocatalytique du $BaTiO_3$, qui n'est pas présente dans le TiO_2. Les taux de réaction catalytique mesurés pour les nanocatalyseurs de TiO_2 anatase décrit dans la première partie du travail ont été ajoutés à la Figure 8 (a) pour comparaison. D'après ces résultats, les K_{obs} diminuent avec la température pour toutes les poudres de $BaTiO_3$. Ce comportement en température du taux de réaction se distingue nettement de celui de la nanopoudre de TiO_2 pour lequel le taux de réaction augmente légèrement avec la température. Cette légère augmentation de taux de réaction pour le TiO_2 lors de l'augmentation de la température, a également été observée dans d'autres études rapportée dans la littérature [15]. Cette différence marquée de la dépendance en température des taux de réaction catalytique des poudres de $BaTiO_3$ et de TiO_2 démontre clairement que les phénomènes physiques dominants à l'origine des réactions catalytiques dans les nanoparticules de $BaTiO_3$ et de TiO_2 sont différents. La dépendance en température de l'activité catalytique des particules de $BaTiO_3$ peut être bien expliquée par la dépendance en température des propriétés piézoélectriques du $BaTiO_3$ tétragonal. L'ampleur de l'effet piézoélectrique du $BaTiO_3$ dépend de l'ampleur de la déformation de sa structure cristalline par rapport à sa structure cubique centrosymétrique. Dans la phase tétragonale, cette déformation est caractérisée par le rapport *c/a*. Il est donc intéressant d'étudier la corrélation entre les taux de réaction catalytique et le rapport *c/a* des particules de $BaTiO_3$ de différentes tailles. Le rapport *c/a* à température ambiante a été obtenu pour chaque échantillon à partir de la caractérisation DRX et Raman discutée ci-dessus (Figure 5 (a)). Nous savons qu'il tombe à 1 à la température de transition de phase.

La Figure 8 (a) montre que l'activité catalytique des particules de $BaTiO_3$ de petites tailles dans un bain ultrasonique est plus importante et plus sensible à la température. Il est évident qu'avec la même concentration pondérale des catalyseurs dispersés dans l'eau contaminée, la surface effective disponible pour la réaction catalytique est plus grande pour les petites particules, ce qui n'a pas été pris en compte dans nos résultats jusqu'à présent. Afin de discuter de la relation entre le taux de réaction catalytique et le potentiel piézoélectrique, nous avons donc calculé un taux de réaction par unité de surface en divisant les taux de réaction obtenus par la surface effective des particules de catalyseur utilisées dans chaque mesure (les particules ont été considérées comme

sphériques avec un diamètre correspondant aux tailles moyennes obtenues à partir de l'analyse des images MET). Selon cette définition, S_{eff} est, pour chaque poudre correspondante, la surface nette des particules de catalyseur pour 1 g de poids. Ces résultats ainsi que le *c/a* obtenu à partir des spectres Raman à différentes températures peuvent nous donner une relation entre les taux de réaction en fonction des paramètres structurels (donc ce cas : la tétragonalité) pour chaque taille de particule. Ces vitesses de réaction effectives tracées en fonction du rapport *c/a* décrivant la tétragonalité des grains cristallins de $BaTiO_3$ sont présentées dans la Figure 8 (b). Contrairement aux taux de réaction de la Figure 8 (a), les taux de réaction effectifs obtenus à partir des différentes tailles de poudre sont maintenant comparables et sont plus importants dans les plus grandes particules. Ceci est dû à la dépendance en température de la polarisation ferroélectrique spontanée par rapport à la taille des particules et des coefficients piézoélectriques qui sont plus grands dans les particules de taille plus grande (parce qu'à la température de la mesure, elles sont plus éloignées de leur température de transition à la phase cubique paraélectrique), générant donc un piézopotentiel plus élevé pour promouvoir les réactions chimiques catalytiques [5].

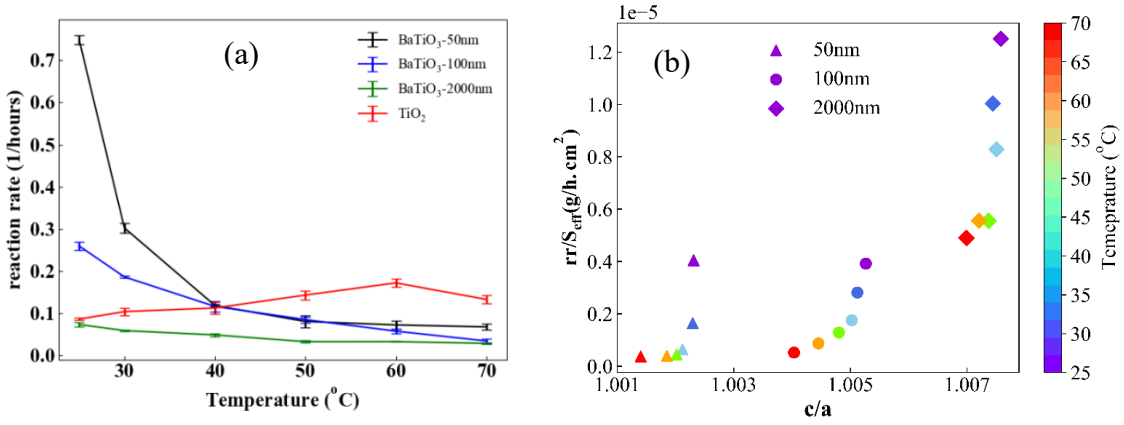

Figure 8 (a) Dépendance de la température des taux de réaction catalytique des poudres de $BaTiO_3$ de différentes tailles , ainsi que des particules de TiO_2 de 100nm. (b) Taux de réaction effectif des différentes poudres en fonction de la tétragonalité c/a obtenue à partir des spectres Raman à différentes températures (rr/S_{eff} est le taux de réaction divisé par la surface effective des particules catalytiques).

3-5 Mécanisme réactionnels des réactions catalytiques

En réalisant quelques expériences contrôlées, soit en ajoutant au système de solution contaminée des additifs piégeurs d'espèces réactives (scavengers) les détails du processus piézocatalytique ont été étudiés. De l'alcool tert-butylique (*TBA*), de la benzoquinone (BQ) et de l'acide d'éthylènediaminetétraacétique sous forme de sel disodique dihydraté (EDTA-2Na) qui

réagissent spécifiquement avec respectivement les radicaux libres ●OH, $\bullet O_2^-$ et les trous ont ainsi été ajoutés à la solution étudiée. Le rapport de concentration relatif (C/C_0) du MO lorsque la nanopoudre de $BaTiO_3$ de 100 nm a été utilisée comme catalyseur lors de l'ultrasonication a ensuite été déterminé en présence des différents piégeurs, comme le montre la Figure 9 (a). Pour le *TBA*, l'EDTA et le BQ, les taux de diminution ont été déterminés comme étant de 48 %, 94 % et 93 %, respectivement. Ces résultats suggèrent que l'ultrasonication avec les nanoparticules de catalyseur $BaTiO_3$ entraîne un nombre important de trous (et d'électrons qui donnent ensuite les radicaux libres de $^\bullet O_2^-$). Dans tous les cas, l'abondance des trous et d'électrons donne lieu à la génération de radicaux $^\bullet OH$ et $^\bullet O_2^-$ lorsqu'ils réagissent avec les molécules d'eau et avec l'oxygène dissous dans l'eau [16] :

$$BaTiO_3 + \text{vibration} \rightarrow BaTiO_3 + (h^+ + e^-) \quad (4)$$

$$O_2 + e^- \rightarrow {}^\bullet O_2^- \quad (5)$$

$$H_2O + h^+ \rightarrow {}^\bullet OH + H^+ \quad (6)$$

Comme le montre la Figure 9 (b), des résultats similaires ont également été obtenus en utilisant des nanoparticules de TiO_2 comme catalyseur en présence de ces même piégeurs de radicaux libres, montrant ainsi que les deux matériaux ont des mécanismes réactionnels catalytiques similaires. Dans la Figure 9 (c), les taux de réaction calculés de la dégradation du MO avec les nanpoudres de 100nm des catalyseurs $BaTiO_3$ et TiO_2 sont comparés en présence des différents piégeurs d'espèces réactives.

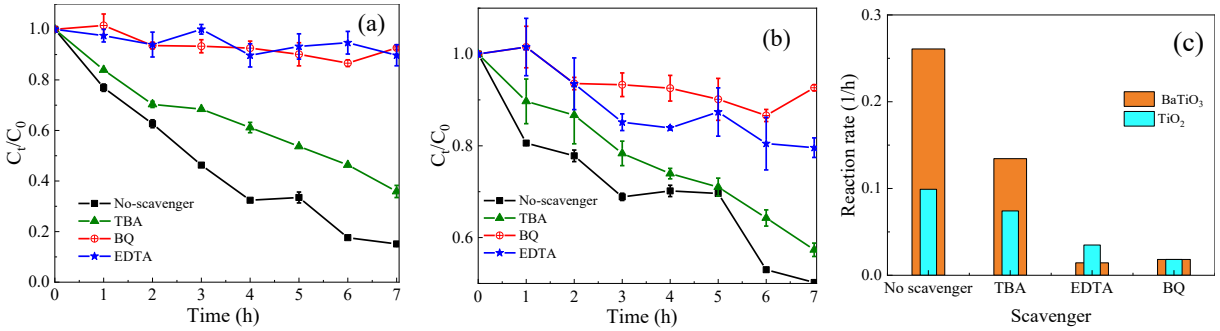

Figure 9 C/C_0 en fonction du temps de vibration ultrasonique en présence de piégeurs de radicaux libres pour les nanocatalyseurs (a) $BaTiO_3$, et (b) TiO_2, et (c) taux de réaction cinétique pour la dégradation du MO obtenus en présence des différents piégeurs.

Pour étudier la présence éventuelle de composés intermédiaires, ainsi que pour déterminer les produits finaux des réactions de dégradation du MO produites par la piézo-sonocatalyse ainsi que pour établir le mécanisme réactionnel de dégradation du MO, la chromatographie en phase liquide couplée à la spectrométrie de masse (LC-MS) a été utilisée. Cette analyse a été réalisée à partir d'un échantillon d'eau contaminée et soumis à différent durées d'ultrasonication, ceci après avoir retiré les nanoparticules de catalyseur de la solution. Les résultats de la caractérisation par LC-MS sont présentés dans la Figure 10 (a) pour le catalyseur $BaTiO_3$. Pour la solution contenant les NPs de $BaTiO_3$, un pic unique et intense apparaît à 3.0 min sur le chromatogramme, attestant de l'existence de MO dissous dans l'eau. L'intensité de ce pic diminue ensuite, ce qui indique que la concentration de MO pur diminue au fur et à mesure de sa dégradation pendant les vibrations ultrasoniques. Cependant, à t = 2h et aux temps ultérieurs, quelques pics supplémentaires révèlent que plusieurs produits intermédiaires ont été créés tout au long du processus de piézo-sonocatalyse. Il est important de noter que lorsque la durée de l'ultrasonication dans le $BaTiO_3$ augmente, l'intensité de chacun de ces pics diminue sensiblement (un comportement similaire est également observé pour les échantillons avec des catalyseurs de TiO_2). Ces pics représentent plusieurs sous-produits organiques qui ont été identifiés par spectroscopie de masse, par exemple, le pic à 1,99 min est principalement indicatif d'un produit avec m/z = 248 (produit D) et le pic majeur à 1,87 min est indicatif d'un produit avec m/z = 290 (produit C). En utilisant ces informations, un mécanisme possible pour la dégradation du MO est proposé dans la Figure 10 (b). Ces résultats indiquent que le radical libre $^{\bullet}OH$ produit par piézo-sonocatalyse attaque le MO, entraînant une substitution aromatique de l'un des cycles benzéniques pour un groupe hydroxyle et la création d'un produit intermédiaire B (m/z = 320). Le groupe méthyle de ce produit est ensuite remplacé par des atomes d'hydrogène dans l'étape suivante, donnant lieu à une variété de produits, comme le produit C (m/z = 290) [17, 18]. Sous l'attaque d'espèces actives comme le $^{\bullet}OH$, le produit C est à nouveau décomposé en produit D. Ce processus se poursuit jusqu'à ce que toutes les grosses molécules soient dégradées, laissant derrière elles des plus petites molécules.

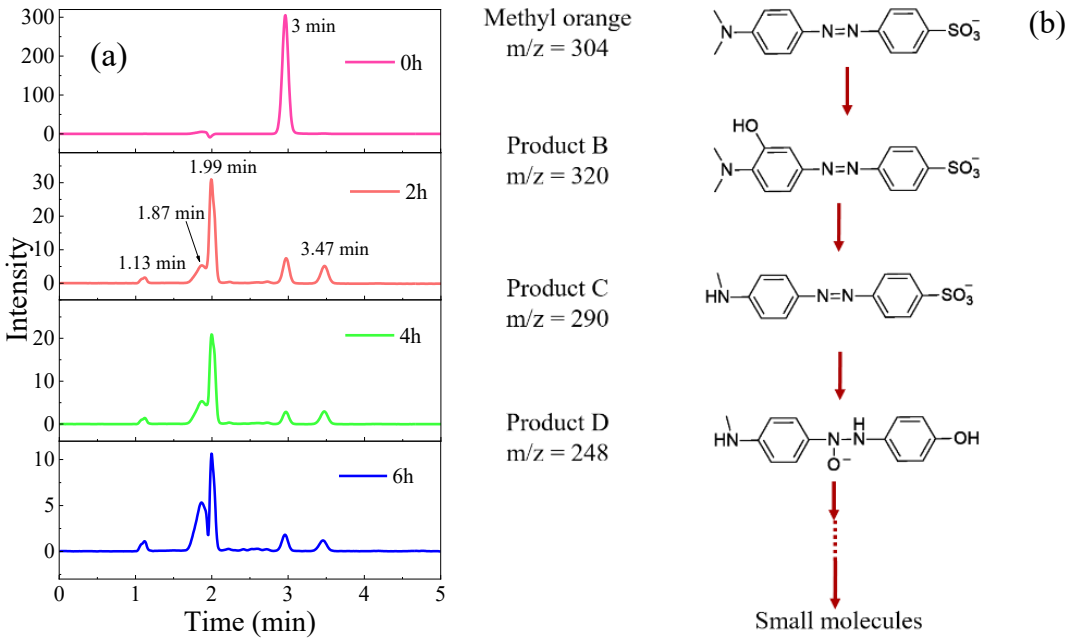

Figure 10 (a) Chromatogrammes obtenus pour différents temps d'ultrasonication à partir de l'eau contaminée par le MO dans laquelle les nanopoudres de $BaTiO_3$ ont été utilisées comme catalyseur, et (b) illustration schématique du mécanisme réactionnel proposé pour la dégradation du MO lorsque des nanoparticules de $BaTiO_3$ de 10 nm sont utilisées comme catalyseur de la réaction catalytique de dégradation.

4- Discussion

Logiquement, la piézocatalyse doit dépendre des coefficients piézoélectriques du matériau utilisé comme catalyseur. Il a été rapporté que parmi les différents coefficients piézoélectriques, c'est le coefficient de contrainte de cisaillement (d_{15}) qui est le plus important pour promouvoir les activités piézocatalytiques du $BaTiO_3$ [19, 20]. Selon la théorie de Landau-Ginzburg-Devonshire (LGD) [21], les différents coefficients piézoélectriques du $BaTiO_3$ peuvent être écrits comme suit:

$$d_{33} = 2\varepsilon_0 Q_{11} \eta_{33} P_s \quad (7)$$

$$d_{31} = 2\varepsilon_0 Q_{12} \eta_{33} P_s \quad (8)$$

$$d_{15} = \varepsilon_0 Q_{44} \eta_{11} P_s \quad (9)$$

Dans laquelle P_s est la polarisation spontanée, η_{ij} est la susceptibilité diélectrique, et Q_{ij} sont les coefficients électrostrictifs. Il a été montré que pour le $BaTiO_3$ tétragonal dans la gamme de température de 20-100 °C, d_{15} domine les deux autres coefficients, et de manière plus importante dans le cadre de notre discussion, il diminue lorsque la température augmente jusqu'à la

température de transition de la phase tétragonale à la phase cubique [22]. D'une part, il a été montré que l'augmentation de la température jusqu'à 90 °C diminue le coefficient piézoélectrique d_{15} des céramiques $BaTiO_3$ d'environ 50% par rapport à sa valeur à température ambiante [23]. Nous savons également que le coefficient piézoélectrique dépend de la taille des particules et qu'il augmente significativement d'environ deux ordres de grandeur lorsque la taille des particules de $BaTiO_3$ passe de quelques nanomètres à quelques micromètres [24, 25]. D'autre part, comme pour toute réaction électrochimique, il existe un potentiel électrochimique minimum pour que les réactions catalytiques se produisent [26]. Avec un piézopotentiel plus faible, ce seuil est moins susceptible d'être atteint lorsque la température augmente pour les poudres de plus petites tailles. Ceci explique bien pourquoi les taux de réaction catalytique diminuent drastiquement pour les plus petites nanoparticules de $BaTiO_3$ lorsque la température augmente. Le modèle d'écrantage, qui prédit que les potentiels de surface du catalyseur piézoélectrique inférieurs à un certain seuil ne peuvent pas produire d'espèces réactives et donc ne peuvent pas promouvoir de réactions chimiques, fournit une bonne explication du comportement en température du de taux de réaction catalytique observé. Ces résultats sont cohérents avec le modèle de "l'effet d'écrantage" expliquant le processus de piézocatalyse. Cependant, en raison de la complexité du système, le processus de réaction d'oxydoréduction électron-trou peut encore partiellement exister, lequel domine principalement le processus de sonocatalyse.

La dépendance à la température des activités catalytiques des nanoparticules de $BaTiO_3$ confirme donc la forte corrélation avec ses propriétés piézoélectriques. Un tel comportement n'a pas été observé pour des matériaux non-piézoélectriques tels que le TiO_2. Nous avons clairement montré que les réactions sonocatalytiques et tribocatalytiques ont des comportements différents de celui des réactions piézocatalytiques lorsque la température du milieu augmente. Contrairement aux réactions de piézocatalyse qui diminuent lorsque la température augmente, l'augmentation de la température peut aider la tribocatalyse à se dérouler, car la probabilité de friction des particules augmente à des températures plus élevées [27]. La sonocatalyse est également affectée positivement par la température, car c'est essentiellement la température des bulles locales de cavitation qui provoque des sauts d'électrons vers la bande de conduction lorsque les bulles s'effondrent. L'augmentation de la température du milieu stimule donc le déroulement de la sonocatalyse, comme indiqué dans la littérature [28]. Ainsi, les résultats de nos expériences

indiquent que les activités catalytiques des particules de $BaTiO_3$ sont dominées par leurs propriétés piézoélectriques. Bien que 70ºC soit inférieur à la température de transition de phase tétragonale à cubique du $BaTiO_3$ et que les nanoparticules devraient encore posséder des propriétés piézoélectriques à cette température, le piézopotentiel des nanoparticules de $BaTiO_3$ devient trop faible pour contribuer de manière significative à leur activité catalytique. À 70°C, les taux catalytiques mesurés pour les particules de $BaTiO_3$ de 50 nm et de 100 nm correspondent aux taux catalytiques mesurés pour les nanoparticules de TiO_2 de tailles similaires et pourraient donc plutôt être attribués - tant pour les nanoparticules de TiO_2 que de $BaTiO_3$ - à une sonocatalyse sans contribution de la piézocatalyse.

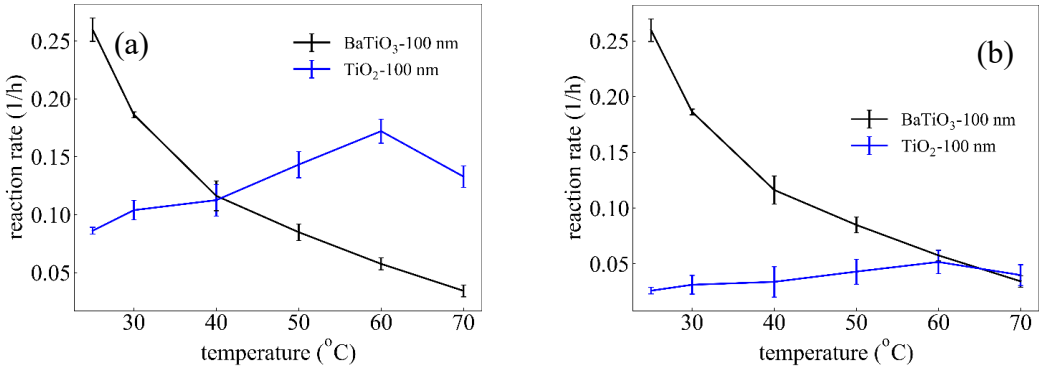

Figure 11 Le taux de réaction catalytique du TiO_2 par rapport aux nanoparticules de $BaTiO_3$ (a) avant et (b) après l'application des corrections de surface et de densité effectives.

Utilisant ces poudres piézoélectriques de différentes tailles, la différence entre les taux catalytiques mesurés à température ambiante et à des températures inférieures à 70°C avec les taux de réaction mesurés à 70ºC et à des température plus élevées devrait alors fournir une mesure quantitative de la contribution de la piézocatalyse pure. D'un point de vue quantitatif, la comparaison de 1g/L de nanopoudres de TiO_2 et de $BaTiO_3$ d'une taille de 100 nm en solution nécessite quelques corrections : Nous avons supposé que la moitié des surfaces libres des particules de $BaTiO_3$ sont terminées par du BaO et l'autre moitié par du TiO_2. Seules ces dernières surfaces sont catalytiquement actives. De plus, à masse égale, le nombre de particules de catalyseur dispersées dans la solution contaminée, sera pour le TiO_2, celui-ci ayant une densité plus faible, supérieur de 40 % au nombre de particules de $BaTiO_3$. Le taux de réaction catalytique des nanoparticules de TiO_2 de 100 nm comparé à celui des nanoparticules de $BaTiO_3$ avant et après les corrections (c'est-à-dire par unité de surface *active*) est illustré dans la Figure 11. Cela montre clairement que la vitesse de réaction catalytique corrigée du TiO_2 ne dépasse

jamais la valeur minimale mesurée pour le $BaTiO_3$, validant ainsi aussi bien notre hypothèse sur l'estimation de la surface active du $BaTiO_3$, que notre hypothèse sur l'addition de deux contributions distinctes à l'activité catalytique totale, à savoir la contribution sonocatalytiques (et possiblement tribocatalytique) et de la contribution piézocatalytique, cette dernière étant dominante pour le particules piézoélectriques de $BaTiO_3$.

Bien que 70 ^oC soit inférieur à la transition de phase tétragonale-cubique du $BaTiO_3$, il semble qu'au-delà de 70°C, le piézopotentiel du $BaTiO_3$ ne soit plus assez important pour jouer un rôle significatif dans l'activité du catalyseur à cette température, du moins pour les plus petites nanoparticules. En d'autres termes, la réaction catalytique à 70^oC et à température plus élevées s'explique par la sonocatalyse plutôt que par l'effet piézoélectrique. Avec une transition de phase tétragonale-cubique à 102 °C, inférieure à la température de Curie du matériau massif, les nanocatalyseur de $BaTiO_3$ de taille 50 nm sont ceux qui montrent le mieux la contribution de chaque effet. Les taux catalytiques du $BaTiO_3$ "corrigés" pour la surface réactive effective sont les suivants : le taux de réaction pour les nanoparticules de 50 nm de $BaTiO_3$ est de 0,07 1/h, ce qui représente environ 10 % de l'activité catalytique des particules de mêmes tailles de $BaTiO_3$ mesurées à température ambiante. En d'autres termes, la partie de la sonocatalyse (et des effets triboélectriques) contribuant aux activités catalytiques dans une telle expérience est d'environ 10 %, le reste étant attribué à l'activité piézocatalytique, la contribution de la piézocatalyse à température ambiante représente donc 90% de l'activité catalytique totale.

Il est important de réaliser, cependant, que la piézocatalyse diffère de l'électrocatalyse et de la photocatalyse car les matériaux piézoélectriques ont en général des largeurs de bande interdite élevées, une très faible conductivité électrique et une densité de charges libres très faible. Bien qu'il y ait présence d'un piézopotentiel, qui peut être élevé, les charges de surface sont des charges liées dues à la présence de dipôles orientés et il n'y a donc que peu ou pas de charges libres à disposition pour participer à la création des espèces radicales réactives. Lorsque le champ électrique généré par les charges liées à la surface interne du catalyseur piézoélectrique dépasse la tension de claquage de la solution, des charges libres y sont générées, qui si elles ont suffisamment d'énergie, produisent des radicaux libres dans la double couche de Helmholtz. Ceux-ci diffusent dans la solution vers les colorants organiques (l'agent contaminant modèle) où ils favorisent alors les réactions catalytiques de manière similaire aux cas de la photocatalyse ou de l'électrocatalyse.

Contents

Figures and Tables

Chapter 1

Chapter 2

Chapter 3

Chapter 4

Chapter 5

Chapter 1

MOTIVATION AND OBJECTIVES

1-1 Introduction

Undoubtedly clean drinking water supply and wastewater treatment belong to the main global challenges of the 21st century. Water corporations throughout the world are struggling with increased demand from one side and worsening water quality and quantity from the other side. Increased loads of emerging and unregulated pollutants including synthetic organic compounds, heavy metals, and various pathogens, as well as other contaminants combined with outdated treatment infrastructure require both water providers and consumers to explore and develop advanced processing technologies in order to keep up with sanitary standards. In agricultural areas, the accumulation of fertilizers and pesticides in surface and groundwater is an emerging barrier to the availability of clean and safe drinking water. The results of a study of 100 small streams in the united states have revealed an average of 62 pesticides (or subcomponent thereof) in each sample [29]. Additionally, hydrophilic and environmentally persistent pharmaceuticals pollutant such as the analgesics and anti-inflammatory drugs ibuprofen or acetaminophen, the

antibiotic amoxicillin or the beta-blocker metoprolol have been detected up to a few hundreds of nanograms per liter in groundwater samples [30]. The lack of toxicological data or studies on the chronic health effects of these chemicals have raised concerns about public and environmental health consequences of long-term exposure to low concentrations of these widely used pharmaceuticals as well as of some personal care products [31]. Some of these pharmaceuticals are also hormonally active and have been categorized as a subset of emerging pollutants that may induce health effects at even relatively low concentrations [32]. Fig. 1- 1 displays wastewater data plotted at the country scale in proportional terms (cubic meter per year per capita for production; and percentage of produced wastewater for reuse), facilitating direct comparisons between countries. Wastewater production per capita is notably highest in North America, over the double of western Europe, the next highest producing region per capita. When considering individual countries in these regions, the USA (211 $m^3 yr^{-1}$ per capita) and Canada (198 $m^3 yr^{-1}$ per capita), in addition to small, prosperous European countries (e.g. Andorra at 257 $m^3 yr^{-1}$ per capita, Austria at 220 $m^3 yr^{-1}$ per capita and Monaco at 203 $m^3 yr^{-1}$ per capita), are the highest producers per capita. Reversely, the reuse of the wastewater in Canada is minimal, meaning that most of the wastewater flows back into the ecosystem with or without being treated. It has been estimated that around 80 percent of the worldwide wastewater flows back into the ecosystem without any treatment that causes the drinking water of more than 1.8 billion people in the world to be contaminated. The strong increase of both the world population and the industrial use of water critically and urgently demands a corresponding increase in water treatments to secure a sufficient supply of clean water for the next generations. It is important to note that most of the wastewater produced by industries is organic pollutants.

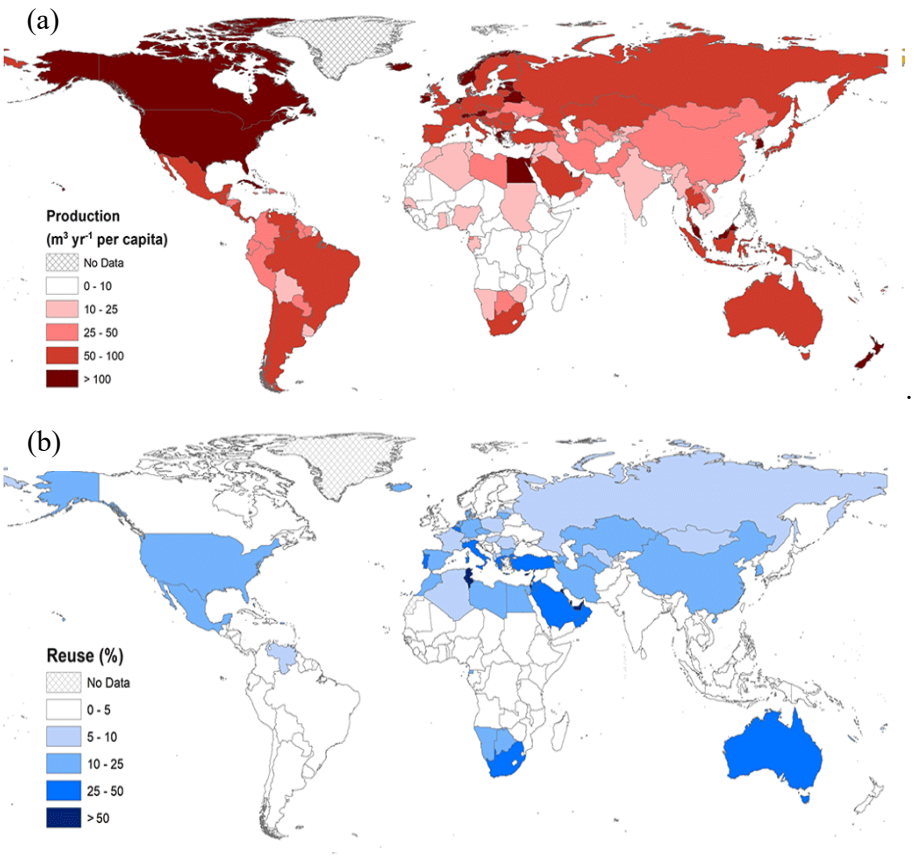

Fig. 1- 1 (a) Wastewater production (cubic meter per year per capita) and (b) reuse (%) at the country scale [33].

In the last 10 years, an increasing number of research studies have been devoted to potential applications of piezoelectric nanomaterials catalytic reactions promoting the decomposition of toxic organic compounds. Piezoelectrics are materials that, when submitted to an external mechanical stress, experience a built-in polarization change that yields the apparition of opposite charges on their opposite surfaces, and the build-up of a potential across of the piezoelectric material. The treatment of wastewater and its decontamination has been one of the main motivation to develop such nanomaterials to detoxify the polluted water via a process known as the advanced oxidation process (AOP) [34]. Photocatalysis in which the catalyst materials degrade the organic pollutants by catalytic reactions promoted by their sunlight irradiation is such an AOP process that is known since more than half a century. Despite their advantages such as their low-cost fabrication methods and the accessibility of sunlight, the efficiency of the photocatalytic systems is still quite low, and research to enhance the performance of such these

materials and systems is still ongoing. Piezo-photocatalysis is indeed one of the results of these efforts to enhance the efficiency of the photocatalytic processes [35]. In this process, the piezoelectric potential helps the photocatalytic reaction by enhancing the photoelectron migration process to the surface of the semiconductor materials, hence enhancing the chemical reactions with the organic dyes. Interestingly, it has been observed during these experiments that the piezoelectric materials were able to promote the catalytic reaction and thus decontaminate water even without sunlight irradiation, which is how the concept of piezocatalysis was born [36].

In a typical piezocatalytic reaction measurement experiment, the piezoelectric catalyst is dispersed in water that was previously contaminated by an organic dye pollutant, and a piezopotential is generated by the mechanical stress induced by sound waves. One important issue in measuring the performance of the piezocatalytic systems is the difficulty (or even the impossibility) of designing an experimental system in which the electron-hole generation is zero in the absence of piezoelectric excitation. In other words, there is not a unique experiment in which we can only measure the piezopotential catalytic effect. One of the main methods to apply the mechanical stress onto the surface of the nanomaterials in order to stimulate their internal piezopotential is via ultrasonication of the solution containing nanocatalysts and pollutants, i.e. to use ultrasonic baths. In this method, the mechanical waves of the ultrasound reach to the surface of the nanoparticles through water and induce a polarization change in the piezoelectric micro and nanomaterials. Typically, when using ultrasonic bath to transfer the mechanical energy of the ultrasonic waves to catalytic nanoparticles through water, not only piezocatalysis, but several different phenomena are likely to occur simultaneously, as for instance the generation and collapse of cavitation bubbles that causes local shock waves and generate large pressure pulses on the surface of the catalyst particles. The catalytic activity resulting of such experiment has been typically reported as being sonocatalysis [37, 38]. Another effect that is likely to occur in such a complicated system is the apparition of surface charges on the particles due to collisions and friction among the particles, a process called triboelectricity. The relative contribution of the piezoelectric effect to the overall catalytic activity and whether it is the dominant effect present in such these experiments is an issue not yet resolved. One important question is indeed to discriminate between the different effects present in such an experiment. In this thesis, we aim to discriminate between the different effects promoting the catalytic behavior,

resulting in the decomposition of the organic dyes, and estimate their relative contributions to the overall catalytic activity.

1-2 Polar materials

The properties of materials are critically dependent on their crystalline structure and of the symmetry thereof, and polar materials are a subset of materials who possess one or several preferential directions. Depending on their symmetry, crystals can be categorized into 32 different crystal classes.

In terms of electric behavior, a material is characterized by its electrical conductivity and dielectric properties. To account for the effects of both free and bound charge within materials, the so-called electric displacement is introduced. The electric displacement D_i in the direction i is given by:

$$D_i = \varepsilon_{ij} E_j \qquad (1\text{-}1)$$

Where ε_{ij} is the dielectric permittivity, and E_j is the electric field in the direction j. In piezoelectric materials, a mechanical stress induces an additional contribution to the electric displacement according to the following relation:

$$D_i = \varepsilon_{ij} E_j + d_{ik} T_k \qquad (1\text{-}2)$$

In which T_k is the mechanical stress in the direction k. The tensor d_{ik}[1] are called the piezoelectric coefficients. Among the 32 crystal classes mentioned earlier, 21 classes have non-centrosymmetric space groups, meaning that they have at least one non-vanishing component among their piezoelectric coefficients d_{ijk}. It should be mentioned here that there is an exception with space group 432, which in spite of being non-centrosymmetric, still is too symmetric to have non-zero piezoelectric coefficients. Among the 20 piezoelectric crystal classes, 10 classes have one or several particular directions, along which a dipolar electric moment could exist. The temperature dependence of this dipolar moment gives another additional contribution to the electric displacement according to the following formula:

[1] Actually, the piezoelectric permittivity d_{ijk} is a third-rank tensor. In order to abbreviate it, due to the symmetry of the $d_{ij,k}$ tensor, and using the Voigt notation, we can rewrite the piezoelectric permittivity as follows:

Tensor notation:	11	22	33	23,32	31,13	12,21
Voigt notation:	1	2	3	4	5	6

$$D_i = \varepsilon_{ij} E_j + d_{ik} T_K + p_i \Delta T \qquad (1\text{-}3)$$

These categories of crystals are called pyroelectrics, and p_i is called the pyroelectric coefficient in the direction i (which is necessarily a polar direction). If these existing dipolar(s) moment(s) in the direction of the polar direction - also called spontaneous polarization – can be reversibly switched between two stable states directed in opposite directions along the polar axis by the application of an external electric field, the crystal is called ferroelectric. The inherent spontaneous polarization P_i directly influences the electrical displacement:

$$D_i = \varepsilon_{ij} E_j + d_{ik} T_K + P_i \qquad (1\text{-}4)$$

The polarization P_i is temperature dependent: $P_i = P_i(T)$. The pyroelectric coefficient of eq.(3) is the temperature derivative of the spontaneous Polarization: $p_i = \frac{\partial P_i(T)}{\partial T}$. A graphical overview of these classifications is given in Fig. 1- 2. The main feature of ferroelectrics to be distinguished from pyroelectrics is the reversible spontaneous polarization with an applied electric field, and its most important characteristic is its dielectric hysteresis. The term "hysteresis loop" refers to the fact that ferroelectric domains with moments pointing in the same direction as the external electric field expand. Fig. 1- 3 shows a typical polarization hysteresis loop. The crystal is non-polarized at first, meaning that the polarization is randomly oriented, and the net polarization is zero. By applying a small electric field, the relation between P and E is look like a normal dielectric, so that by turning off the electric field, the net polarization turns back to zero. However, by applying a large electric field, cause the polarization to be aligned in one direction, and there will remain in that state even after the electric field is turned off. Therefore, it is important to note that ferroelectricity is not merely a structural property but is a phenomenological reality that may exist in some pyroelectric materials. In this figure, by increasing the external electric field the polarization reaches its saturation point of P_s in which all the electric moments are aligned in the direction of that external field. By decreasing this field down to zero, a remanent polarization of P_R remains in the structure of the ferroelectric material. Another external field opposed to the remanent polarization as big as the value of the coercive field is needed to bring the macroscopic polarization back to zero. The area of the ferroelectric hysteresis loop corresponds to the work needed to switch the polarization in the opposite direction and switch it back to its original direction. The Curie temperature in polar materials is the temperature threshold at which thermal agitation overcomes the ferroelectric order that

comes with the structural phase transition from the centrosymmetric to the non-centrosymmetric structure. When temperature increases from below the Curie temperature ad crosses the Curie temperature, the crystal structure changes from a non-centrosymmetric pyroelectric or ferroelectric phase (at $T<T_c$) to a paraelectric centrosymmetric phase (at $T>T_c$).

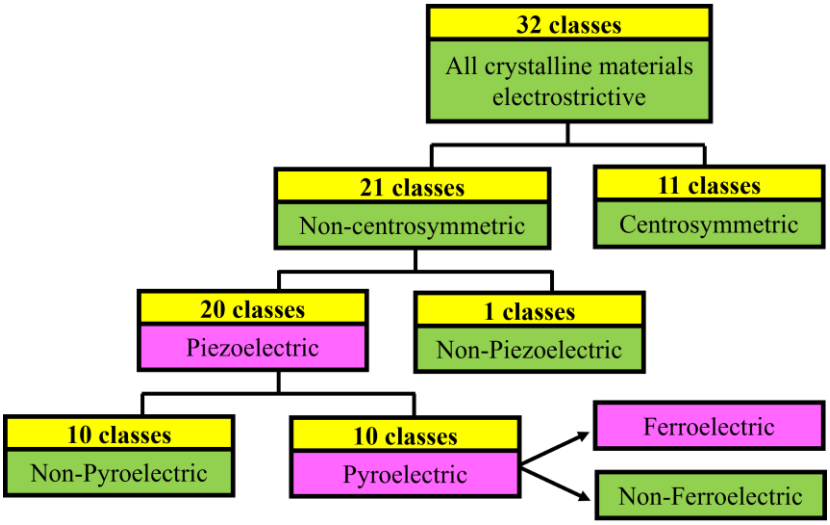

Fig. 1- 2 Classification of the crystals; among the 32 crystal classes, 20 classes exhibit piezoelectricity, and 10 out of the 20 piezoelectric crystals would be pyroelectric. If the electric field can reverse the polarization of the crystal, then the material is denoted a ferroelectric.

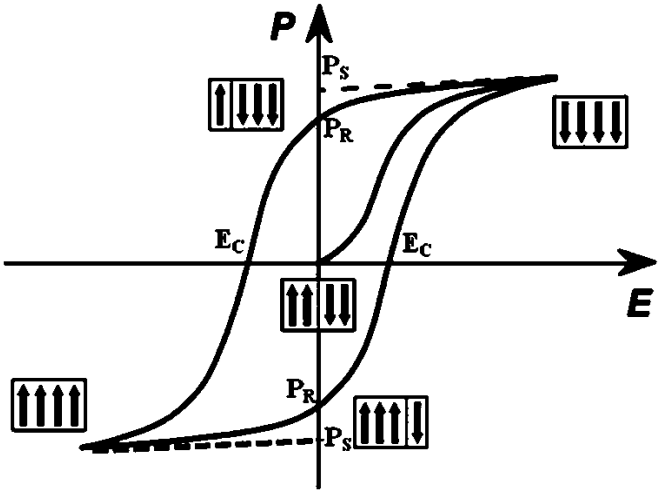

Fig. 1- 3 a typical hysteresis (P-E) loop of ferroelectric materials.

1-2-1 Piezoelectrics

The piezoelectric effect can be simply explained by a molecular model shown in Fig. 1- 4. In this model, the electric charge is generated as a result of a force exerted on the material. Before

applying an external mechanical stress, the centers of the negative and positive charges of each molecule coincide, resulting in the electric neutrality of the molecules as shown in Fig. 1- 4 (a). However, the local structure of the molecule can deform in the presence of an external mechanical stress, resulting macroscopically in an elastic deformation, and microscopically in the separation of the positive and negative centres of charge of the molecules and his the creation of tiny dipoles, as seen in Fig. 1- 4 (b). The opposite facing poles inside the piezoelectric material cancel each other, and a net charge remains at each external surface as is illustrated in Fig. 1- 4 (c). This effect in which a polarization appear in the structure of the material duo to the mechanical stress is called the piezoelectric effect.

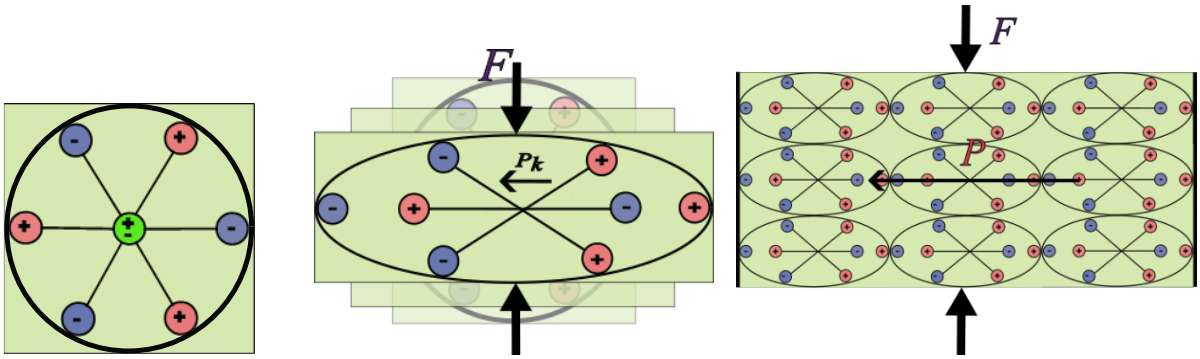

(a) (b) (c)

Fig. 1- 4 a simple schematic of the piezoelectricity of the molecular scale; (a) a molecule before the piezoelectric perturbation, (b) The molecule after being subjected to an external mechanical stress (F_k), the results a polarization P_k, and (c) the macroscopic polarization of the piezoelectric material after being subjected to the external stress.

The electric current, generated by the electromechanical effect at play in the piezoelectric material is shown in Fig. 1- 5. If conductive electrodes present at two opposite ends of the piezoelectric material are externally short circuited and a galvanometer is connected to the circuit as shown in Fig. 1- 5 (a), when no mechanical force exerted on the piezoelectric material, no current flows in the circuit and no current can be measured by the galvanometer without applying. Alternatively, when a mechanical force is applied on the piezoelectric material, it induces a polarization within the piezoelectric material and charge appear on its surface as shown in Fig. 1- 5 (b). This surface charges generate an electric field across the external electric circuit causing a flow of free charges through the conducting electrodes and wires to neutralize the stress-induced surface charges. Although the current is transient, the piezoelectric voltage across

the piezoelectric material is present as long as the force and deformation are present. This is the working principle of piezoelectric sensors. Piezoelectric materials could also be used for the reciprocal piezoelectric effect. The reverse or converse piezoelectric effect consist in applying a voltage across the piezoelectric material, which generate an electric field across the material, exerting a force on the small dipole moments present within the material and producing a contraction or an extension of the material, i.e. a variation of its dimension. This is how piezoelectric actuators work.

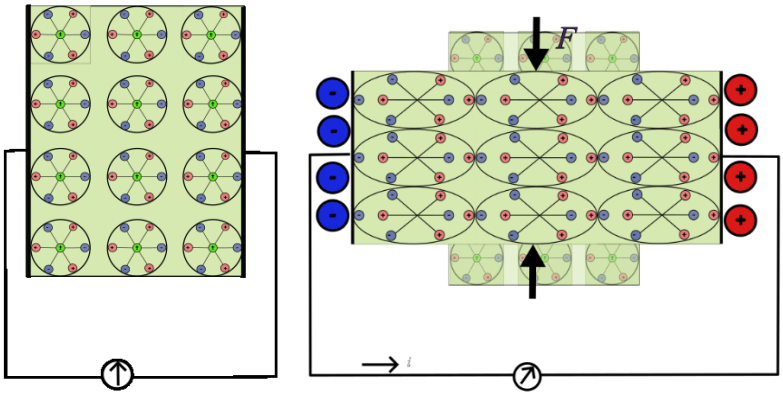

(a) (b)

Fig. 1- 5 (a) the absence of electric current through the short circuit around the piezoelectric material when it is not under a mechanical stress, (b) the presence of the electric current duo the mechanical force on the piezoelectric material.

Equation (1-2) that was introduced for the piezoelectric materials can be written in its tensor form as:

$$\begin{bmatrix} D_1 \\ D_2 \\ D_3 \end{bmatrix} = \begin{bmatrix} \varepsilon_{11} & \varepsilon_{12} & \varepsilon_{13} \\ \varepsilon_{21} & \varepsilon_{22} & \varepsilon_{23} \\ \varepsilon_{31} & \varepsilon_{32} & \varepsilon_{33} \end{bmatrix} \begin{bmatrix} E_1 \\ E_2 \\ E_3 \end{bmatrix} + \begin{bmatrix} d_{11} & d_{12} & d_{13} & d_{14} & d_{15} & d_{16} \\ d_{21} & d_{22} & d_{23} & d_{24} & d_{25} & d_{26} \\ d_{31} & d_{32} & d_{33} & d_{34} & d_{35} & d_{36} \end{bmatrix} \begin{bmatrix} T_1 \\ T_2 \\ T_3 \\ T_4 \\ T_5 \\ T_6 \end{bmatrix} \quad (1\text{-}5)$$

where the Voigt notation introduced earlier has been used. The symmetry of the piezoelectric materials is reflected in the symmetry of its piezoelectric tensor so that many of these tensor components are zero. Considering structural symmetry, and Voigt notation, the equation can be simplified as below for piezoelectric materials having symmetry groups 4 mm and 6 mm:

$$\begin{bmatrix} D_1 \\ D_2 \\ D_3 \end{bmatrix} = \begin{bmatrix} 0 & 0 & 0 & 0 & d_{15} & 0 \\ 0 & 0 & 0 & d_{24} & 0 & 0 \\ d_{31} & d_{32} & d_{33} & 0 & 0 & 0 \end{bmatrix} \begin{bmatrix} T_1 \\ T_2 \\ T_3 \\ T_4 \\ T_5 \\ T_6 \end{bmatrix} + \begin{bmatrix} \varepsilon_{11} & 0 & 0 \\ 0 & \varepsilon_{22} & 0 \\ 0 & 0 & \varepsilon_{33} \end{bmatrix} \begin{bmatrix} E_1 \\ E_2 \\ E_3 \end{bmatrix} \quad (1\text{-}6)$$

1-3 Advanced processes for water treatment

Advanced oxidation processes - or more accurately reduction-oxidation or redox processes - at play in water treatment are related to the presence of hydroxyl radicals •OH playing the main role as the reactive oxidative species in the catalytic reactions. Hydroxyl radicals are formed when one of the electrons of the negatively charged hydroxyl anion (OH^-), has been removed. Their electric charge is thus neutral, but they then have an unpaired electron spin. Due to its electronic structure with unpaired electron carrying an unpaired spin driving the hydroxyl radical toward immediate capturing (or sharing) the 'missing' electron from another molecule, the hydroxyl radical is very susceptible to oxidative processes, namely those involving the capturing or sharing of an electron from another molecule. One of the most important features of hydroxyl radicals is their oxidative potential (E^0) which is among the highest (just after fluorine), which makes it a powerful oxidative agent in redox reactions. Advanced catalytic oxidation is a powerful tool in the range of innovative methods presently investigated and developed for wastewater remediation, as well as to be used for other challenges related to various pollution problems hard to tackle. These active free radicals have the ability to oxidize organic pollutants into CO_2, H_2O, or certain inorganic ions, while also preventing the production of by-products that could slow down the complete degradation of the targeted pollutants [39]. In contrast to some traditional advanced oxidation processes using oxygen peroxide (H_2O_2), and ozone (O_3), which are expensive methods with the requirement of complex equipment to produce H_2O_2 and O_3, and also generally bear the possibility of the formation of toxic secondary products, the methods based on the hydroxyl groups are more environmentally friendly as well as cost effective. In the following, some examples of these methods involving hydroxyl radicals and advanced oxidation processes in their catalytic reactions are discussed.

1-3-1 Photocatalysis

Photocatalysis and photolysis in general are known since the decade of 1960 [40]. Since then, the photocatalytic reaction has been extensively studied, and it can be said that the fundamental science involved is well established now. Photocatalysis is a process in which the electrons and holes of an organic substance are excited by sunlight irradiation, and then participate in the catalytic chemical reactions to decompose that organic substance, e.g. organic dyes, which are typical pollutants usually present in wastewater. If the photon energies of the light are greater or equal to the bandgap of the semiconductor, the valence band electrons are photo-excited and promoted to the conduction band in a few femtoseconds leaving a hole in the valence band of that semiconductor. If these excited free electrons reach the surface of the semiconductor, they will have a chance to participate in the surface catalytic reactions that lead to the degradation of pollutants such as organic dyes into CO_2 and other inorganic compounds. This can occur by the activation of dissolved O_2 and H_2O_2, releasing active radicals, in particular hydroxyl radicals [41]. This process can take place in ambient conditions in various media, liquid or gas, such as in water or even in dry air. In aqueous solutions, the presence of •OH, and h^+ can effectively oxidize organic dyes such as aromatic and aliphatic compounds dissolved in liquid with a high reaction rate of up to 10^9 Ms^{-1} [42]. The mechanism of the photocatalysis that yields the active species on the catalyst surface is schematically shown in Fig. 1- 6. The only requirement for the photocatalytic reactions - besides the ultra-bandgap energy - is the presence of oxygen. Photocatalysis is cheap and accessible to many parts of the world and represents therefore a growing market that has been estimated in 2021 to $2 billion. However, Photocatalysis is a process still suffering from low catalytic reaction rates for the degradation of pollutants such as organic dyes.

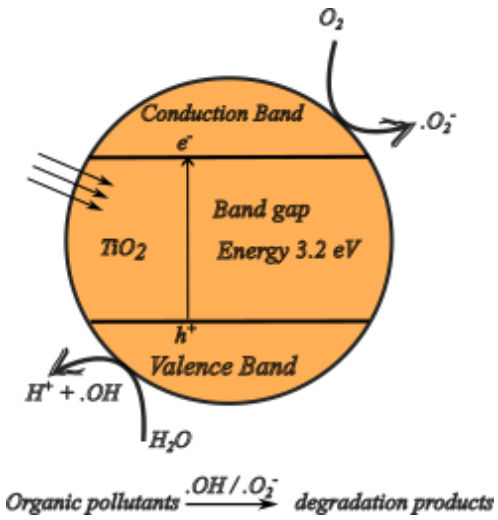

Fig. 1- 6 Schematic of the proposed photocatalysis mechanism for TiO_2 nanoparticles

The reaction rate in photocatalysis is strongly dependent on the *e-h* pairs charge separation of and of their lifetime. Many methods have been proposed to enhance photocatalytic activities, such as band gap tuning, using composite semiconductors, nanostructured morphology engineering, and introducing defects to the lattices. One of these methods recently proposed is to use piezoelectric catalysts and promote and enhance the charge separation using the internal field generated by piezoelectric effect, which is called piezo-photocatalysis. The piezoelectric potential, which is coming from the internal polarization of the piezoelectric materials induced by an external mechanical stress, can drive free electrons to the surface of the semiconductor, where they can participate in the chemical reactions. Accordingly, the free electrons in the conduction band are driven to the positively charged surface, and the hole to the negatively charged one. This process is able to increase the reaction rate of the dye degradation by factors ranging between one to two orders of magnitude, depending on the structure and morphology of the piezocatalysts used.

1-3-2 Sonocatalysis

Ultrasonic waves have been experimentally observed to enhance catalytic reactions when applied for the degradation of the organic dyes soluble in water. This has been mostly explained by the phenomenon of cavitation produced by ultrasounds in liquids: Ultrasonic waves produced and propagating through the liquid (typical situation in an ultrasonic baths) is leading to the production and growth of the macro and micron-size bubbles in liquids, whose subsequent

implosion can release locally a vast amount of energy [43]. The transient conditions specifically the local hot temperature of up to 5000 K as well as the local pressures up to of 1800 atm inside the cavitation bubbles cause locally confined extraordinary micro-environments inside the liquid [44]. The extraordinary conditions in these micro-environments enable the dissociation of water molecules to produce hydroxyl radicals (•OH), which in turn can act as oxidant agents in catalytic reactions according to the following reaction [45]:

$$H_2O \xrightarrow{)))} OH^{\cdot} + H^{\cdot} \qquad (1\text{-}7)$$

Alongside the production of the hydroxyl groups, the harsh local conditions on the surface of the semiconductor particles in the liquid, in particular the extreme local temperatures cause the electrons in the valence band to jump to the conduction band. These electrons may later take part to the catalytic reaction involving the radicals generated inside the liquid (often water) and help decomposing the pollutant (e.g. organic dyes). This latter effect of the semiconductor nanoparticles improves the increases the number of active sites around the radicals. However, the removal of organic pollutants by the ultrasonic process under sonocatalysis requires long times and a vast amount of energy to completely remove the dissolved organic dyes in water. Some of the non-piezoelectric candidates that have been considered as catalyst for wastewater treatment include carbon bases nanostructures like graphene, CNT, C60, C_3N_4 [46, 47], or metal oxide candidates such as Fe_3O_4, TiO_2, CeO_2, V_2O_5, and Al_2O_3 [48, 49].

1-3-3 Piezocatalysis

By developing piezo-photocatalysis as a new way to enhance the catalysis reaction kinetics, it has been observed that piezoelectric materials are also able to play the main role in catalytic reactions, acting themselves as catalysts, so that they don't necessarily need sunlight to show catalytic activities. Owing to their non-centrosymmetric structures, mechanical stress exerted onto piezoelectric materials leads to a change in their intrinsic electrical polarization and the apparition of bound charges at the surface accompanied by a piezoelectric potential across the material along the direction of its polarization. Fig. 1- 7 shows a schematic of a $BaTiO_3$ nanowire that is submitted to an external force, such as mechanical pressures. Duo to this mechanical force (in the schematic figure bending the wire; the actual mechanical forces may generate more complex deformations, including shear deformations), a piezoelectrically induced polarization and the resulting surface e bound charges appear around the piezoelectric wire. In the presence of

organic dyes soluble in water, the bound charges promote the production of hydroxyl radicals (•OH) and oxygen anions radicals (O_2^-) that are essential in the decomposition of the organic dyes. Since the charge exchanges between the surface and the surrounding medium strongly depends on the electrochemical potential difference between the surface and surrounding medium, the mechanical strain-induced piezopotential therefore significantly affects the material's electrochemical activity [50]. Most of the piezoelectric titanates including $BaTiO_3$, $BiTiO_3$, $SrTiO_3$ and other piezoelectric materials such as ZnO, and PZT have shown piezocatalysis activity. Among these materials, $BaTiO_3$ has shown a stable and reproducible catalytic activity, promising for future catalysis applications.

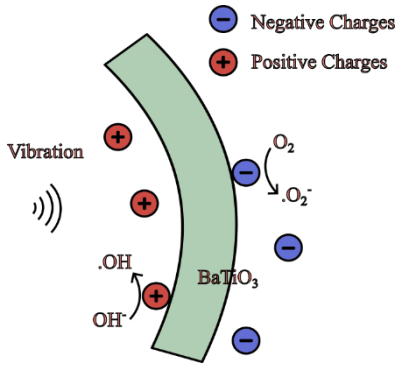

Fig. 1- 7 Schematic view of the at play in piezocatalysis using piezoelectric $BaTiO_3$ nanowires as catalysts

1-3-4 Tribocatalysis

The friction between two solids may also cause an exchange of their electrons. Owing to their electron affinity, some particles may take or donate the electrons from or to other particles that they enter in contact with, generating surface charges. This effect, dubbed tribocatalysis, has been shown to be able to provide surface electrons suitable for taking part in catalytic activities. Catalytic reactions promoted by the triboelectric effect have been reported for different semiconductor nanoparticles such as TiO_2 [51], $BaTiO_3$ [52] and CdS [53] nanostructures.

1-4 Applications

The scarcity and gradual deterioration of water resources have given the wastewater treatment plants (WWTP) a fundamental role and a great importance among the number of activities undertaken in the field of water protection. Generally, WWTP uses different steps to purify water, the first step of wastewater treatment being its collection. Three different processes physical, chemical, and biological treatments then apply to the wastewater. During the primary

stage, the solid particles floating inside water are removed from the wastewater. This stage uses screens, sands, and grit chamber to remove the solid particles of different sizes. In the secondary treatment step, the wastewater is submitted to biological processes to dissolve organic cells, bacteria, and microbes present in the wastewater. The last step and most critical stage of wastewater treatments is called the tertiary treatment during which the toxic chemical elements and organic contaminants and/or specific pollutants are removed from the wastewater. This latter step is also the most expensive part of the wastewater treatment process. One of the different Physio-chemical Treatment (PCT) methods reported in recent years is using activated carbon to remove organic compounds from the wastewater. Owing to the advances and developments of nanotechnology, various novel approaches have recently been suggested and developed. For instance, different catalytic methods have been proposed to decompose the organic dyes soluble in water. such as photocatalysis [54], electrocatalysis [55], and Fenton reactions [56]. Recently Piezocatalysis, has also been investigated and suggested as a promising way to decompose the organic dyes and medical compounds such as antibiotics.

Beside the wastewater treatment applications, side reactions in a piezocatalytic cell may also be applied in other applications. It is for instance well stablished that hydrogen can be produced by using these types of piezocatalytic reactions [57]. Due to the high demand of hydrogen as a source of energy, this method can be considered as a novel approach to consider in the hydrogen production sector. Moreover, such these reactions have been noticed in the medical sector. Recently, Shi *et al* showed that tetragonal $BaTiO_3$ nanoparticles activated by ultrasonic irradiation can help eradicating cancer tumors via piezocatalytic reactive oxygen species generation [58]. Anecdotically, it has also been suggested that similar piezocatalytic processes would be useful for some specific nondestructive tooth whitening [59].

1-5 Description and objectives of the project

The details of the piezocatalysis mechanisms of have been explained by two different models. The first model, based on the energy band theory and borrowed from our understanding of the widely accepted photocatalytic mechanisms, postulates that the piezopotential, namely the stress-induced electric potential generated across the piezoelectric material, plays a significant role to enhance the transport of the free electrons in the conduction band to the surface of the catalyst material. In this theoretical model, the piezopotential serves as the handle to adjust the band

structure, in particular the energy level of the band edges at the opposite surfaces of the piezoelectric material, in order to control the flow of internal charge carriers to the surface of the piezocatalyst, these charges promoting the production of free radicals and - in turn - initiating the catalytic chemical reactions in the nearby solution. In the second model, the piezocatalysis reactions are explained by the presence of screening charges at the surface of the piezoelectric material and is indeed called the 'screening charge effect' model. In this model, the free electrons inside the piezoelectric material and their energy do not play a critical role and the surface potential is just a consequence of the built-in polarization. The latter are compensated outside the surface of the piezoelectric material by free screening charges from the nearby (liquid) medium forming an electrical (Helmholtz) double layer. Rather than the free electrons originating from the piezoelectric material playing the most important role, in this model the surface-adsorbed screening charges are indeed the main actors and participate in the generation of free radicals, which in turn are promoting the catalytic chemical reactions.

To find the best model to explain the contribution of the piezoelectric effect in the catalytic activities of piezoelectric materials, one should design an ideal piezocatalytic experiment in which the number of the free electrons in the conduction band of the piezoelectric material - usually nanoparticles - would approach zero. Hence, piezocatalytic experiments, including sonication, are performed in dark to prohibit electron-hole excitations. This procedure, however, does not prevent all possible electron-hole excitations, since electrons in the conduction band can also be generated directly by the ultrasonic waves excitation. In particular, the electron-hole pairs can still be excited by the local heating of the system induced by the ultrasonic waves through the sonocatalysis process, in addition to that of piezocatalysis. In general, the complexity of the phenomena at play for the 'in-liquid' ultrasound experiments does not allow to prevent all electron-hole excitations, and therefore to directly measure experimentally the effects of the sole piezocatalysis. In this thesis we aim to investigate and evaluate the real contribution of the piezoelectric effect and be able to discriminate the latter from the other possible effects such as sonocatalysis or tribocatalysis that may occur simultaneously in the same experiment. Barium titanate is a well-studied piezoelectric material which has a temperature dependent structural phase and known piezoelectric properties. It has also been used in catalytic experiments and has been reported to exhibit piezocatalytic properties. $BaTiO_3$ nanoparticles were therefore chosen as a 'case study' for our experiments, aiming at investigating the role of the piezoelectric effect.

The main objective of this project is to determine the contribution of the piezoelectric properties in the catalytic degradation process of the dye methyl orange in solution, which is being subjected to ultrasonic vibrations by means of an ultrasonic bath. Ultrasonic bath is the most used source of mechanical vibrations at ultrasonic frequencies in the reported piezocatalysis experiments and will be the source of ultrasounds used in this study. Different characterization techniques have been used that will be explained in detail. We will also discuss which model best describes and explain the mechanism of the degradation of the methyl orange organic dye during this process.

1-5-1 Contribution of $BaTiO_3$ piezoelectric effect to its catalytic activities

The main goal of this thesis is to find out quantitatively or at least semi-quantitatively the contribution of the piezoelectric effect to the overall catalytic activities of piezoelectric materials. Nanoparticles of $BaTiO_3$, perhaps the most widely studied piezoelectric material, were chosen as piezocatalyst material in this project. In order to discriminate between the pure piezoelectric effect and the other effects that may exist in the different experiments, such as sonolysis, triboelectric effects and even photo-excitations, we used a model in which the catalytic activity of *piezoelectric* $BaTiO_3$ (BTO) were compared to the well-known catalytic activity of the *non-piezoelectric* material TiO_2. Barium titanate crystals do possess two different surface terminations, namely (i) Ba-O, and (ii) Ti-O surface termination, as it is schematically shown in Fig. 1- 8. Since Ba-O external surface is highly susceptible to chemical reaction with CO_2, they are likely to rapidly turn into $BaCO_3$, with no effective active sites on this surface. Alternately, the Ti-O terminated surfaces of BTO are very similar to the surfaces of TiO_2 and are anticipated to have comparably active and lead to a catalytic activity of $BaTiO_3$ – more specifically of its Ti-O terminated surfaces - possibly quite similar to that of TiO_2. ***Then according to this model, it is assumed that the non-piezocatalytic activities of the $BaTiO_3$ (sono, tribo or any other reactions except piezocatalytic effects) can be somewhat scaled to to the TiO_2 catalytic response***. It is acknowledged here that TiO_2 and BTO are neither structurally nor electronically exactly the same but it is assumed they are sufficiently similar so that TiO_2 can serve as a model of a *hypothetical non-piezoelectric $BaTiO_3$*, which can be used for comparison and evaluation of our experimental results.

To assess the contribution of the piezoelectric effect in the catalytic activity of $BaTiO_3$ in the degradation of methyl orange, we studied two main critical parameters, namely temperature and nanoparticles size.

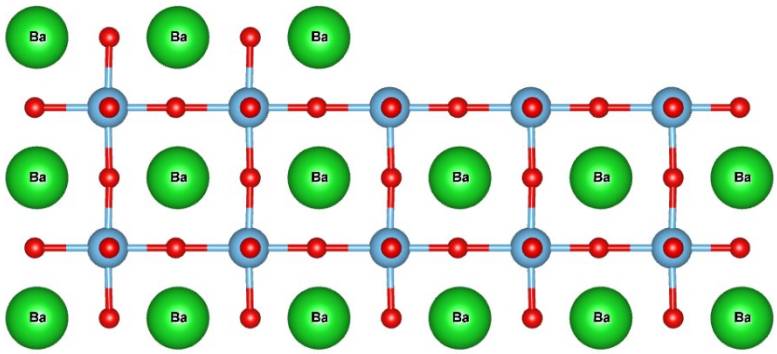

Fig. 1- 8 Illustration of the two possible surface terminations in a $BaTiO_3$ crystal. In order to simplify our illustration the oxygen atoms (ogygen octahedra around each Ti atom) have been removed.

1-5-2 Temperature effect

The piezoelectric properties of $BaTiO_3$ are strongly dependent on the temperature. $BaTiO_3$ exhibits a tetragonal structure at room temperature, and its bulk transition from a tetragonal ferroelectric to a cubic paraelectric phase, occurs at the transition temperature (T_C) of approximately 130 ºC. However, the tetragonality of $BaTiO_3$, defined as *c/a*, is also dependent on temperature, so that by increasing the temperature, ratio of the lattice parameters c and a, which is representative of the elongation of the structure in the *z* direction, decreases when the temperature increases from room temperature to $T_{C,}$ where it becomes unity for the cubic structure In addition, the ferroelectric phase transition temperature T_C of $BaTiO_3$ nanoparticles has also been shown to be dependent on the size of the nanoparticles. We will show how temperature and size effects can help us to refine our model to evaluate the contribution of the piezoelectric properties of $BaTiO_3$ to the overall catalytic activity for both piezocatalysis and photocatalysis experiments.

1-6 Thesis outlines

The dissertation of the thesis consists of 5 chapters which are structured as follows:

The 1st chapter discusses the basic concepts used in the thesis. It presents the motivation of the research and outlines the importance of the subject in the context of the limited clean and drinkable water resources. It first presents the fundamentals of polar materials including piezoelectrics, pyroelectrics, and ferroelectrics. Then the advanced oxidation processes are

presented with some examples which include photocatalysis, piezocatalysis, and sonocatalysis. Finally, the main ideas and the objectives of the project are introduced in detail.

The 2nd chapter gives a review on the piezocatalysis mechanism based on the two physical models based on the 'energy band theory' and 'screening charge effect', followed by a description of the different methods used and reported in the literature as being 'piezocatalysis experiments. Next, more details about piezocatalyst materials will be given, and finally, the methodology and techniques used in this study are presented.

The 3rd chapter first presents the principles of the methods used to synthesize the nanoparticles of piezoelectric and catalytic materials, namely the microwave-assisted hydrothermal synthesis method. The second part of the chapter discusses all the characterization techniques used in this study are presented, namely X-ray diffraction technique, Transmission electron microscopy (TEM), Raman spectroscopy, Liquid chromatography-mass spectroscopy (LC-MS), UV-Vis-NIR absorption spectroscopy, as well as the piezocatalysis setups used to carry out this research.

The 4th chapter of the thesis discusses in detail the main results obtained in this research. It includes the synthesis and characterization of $BaTiO_3$ nanoparticles using microwave assisted hydrothermal method, that was done as the first step of this project. Next, the measured piezocatalytic activities of $BaTiO_3$ and TiO_2 nanoparticles for the degradation of methyl orange, the dye chosen as model pollutant in this study, are compared together. The results presented in this section permit to evaluate the contribution of the piezoelectric properties to the overall catalytic process. Finally, the temperature effect, and size effect are be discussed as important parameters affecting the piezocatalysis process.

The 5th chapter gives a summary of the whole project as well as its conclusions. This chapter also gives some perspectives and suggests some recommendations which may form the basis for further studies.

Chapter 2

Piezocatalysis - State of the Art

2-1 Introduction

During the last decade, it has been proposed to generate a piezoelectrically-induced electrical potential at the surface of piezoelectric material via an applied mechanical stress in order to promote redox reactions [36]. In particular, researches have been conducted in order to take advantage of these piezopotential-promoted redox reactions degrading various organic pollutants as a new way of treating wastewater, which was dubbed piezocatalysis. Regardless of its applications, piezocatalysis has two different aspects that should be carefully considered: (i) the generation and existence of the piezoelectric potential (or piezopotential), and (ii) understanding how this piezopotential promotes and rives the catalysis processes. One of the main challenges regarding the piezopotential is to estimate its value in relation with the mechanical energy reaching the surface of the piezoelectric catalysts, and to establish whether it is suitable to the promotes the redox reaction, i.e. whether it is sufficient to reach the redox potential of the chemical reaction degrading a specific organic pollutant. Another important challenge about the

chemistry of the catalytic reactions is to establish - for a given value of the piezopotential - what are the active radicals produced and whether they are suitable to drive the redox reactions that yield the decomposition of the organic pollutant under consideration. Moreover, if these processes proceed in an environmentally friendly manner should also be established. Until now, piezocatalysis experiments, in which the mechanical energy is converted into an electric potential have been restricted to some specific experimental setups and piezoelectric materials. In this chapter we review the existing literature and discuss the achievements of piezocatalysis to review the answers that were proposed so far given to these questions.

2-2 Piezocatalysis models

One of the most important questions in piezocatalysis is to understand in detail how the piezopotential does govern the catalytic reactions in a typical piezocatalysis system. The catalytic processes induced by the piezopotential is generally explained on the base of two different models: the ‘Energy band theory’ model, and the 'Screening charge effects’ model. The latter model emphasizes the piezopotential as the results of surface bound charges originating from the internal polarization in the piezoelectric material requiring surface adsorbed screening charges to compensate for them. In this model it is shown that the piezopotential can easily exceed the Gibbs free energy required for specific chemical reactions to proceed [60]. The second model is based on the energy band theory and is inspired from the physical models proposed to explain the photocatalytic effects. Briefly, it states that the specific chemical reactions are mainly determined by the energy band edge levels. In this model, the piezoelectric potential serves as the “handle” to initiate the reactions, to adjust the band structure, and to control the internal charge carrier flow to the catalyst surface. One main difference between these two models is that the source of the free electrical charges in the ‘band energy theory’ model is originating inside the piezoelectric material i.e they are the electrons in the conduction band, and the holes in the valence band of the structure, whereas in the ‘screening charge effect’ model, the charges participating in the redox reactions are surface adsorbed screening charges originating in the medium outside the piezoelectric material. In the following, these two models are described and explained in detail.

2-2-1 'Screening charge effect' model

In the 'screening charge effect' model the piezopotential and above all its associated surface adsorbed screening charge play dominant roles in the catalytic activity of the piezoelectric material. In this model, it should be demonstrated that the magnitude of the piezopotential level at the catalyst surface is aligned with the required redox reaction potential, so that it is consistent with the well-known process of electrocatalysis, which is able to determine which conditions are required for the desired chemical reactions to proceed in order to decompose a specific organic dye. In his model, the relation between the polarization-induced piezopotential and the surface screening condition is well described and established. Therefore, understanding the screening effect of the piezopotential is of primary importance.

In order to understand this model, we first briefly introduce conventional electrocatalysis, a well-established technique developed earlier [61]. The applied electrical potential provided by an external power supply adjust the electronic levels of the electrodes so that the electrons could flow (from the electrode toward the medium or form the medium towards the electrode) and take part in the catalytic chemical reaction. The application of an electrochemical potential may result in one of the two following processes: (1) lowering electronic energy levels of unoccupied states within the electrode to a value smaller than that of the highest occupied molecular orbital (HOMO) of the material in solution; or (2) raising occupied states within the electrode above the lowest unoccupied molecular orbital (LUMO) of the material in solution. Under the first condition, electrons will leave the HOMOs in solution and transfer to the unoccupied states within the electrode oxidizing the solution. Under the second condition, electrons will leave the occupied states in the electrode and transfer to the LUMOs in solution reducing the solution. When the electrode is a non-metallic solid, the $e\varphi_{HOMO}$, $e\varphi_{LUMO}$ energy levels of the solution extend to the material's valence ($e\varphi_{VB}$), and conduction band ($e\varphi_{CB}$) edges, respectively. In the case of piezocatalysis, the potential produced by the external power source is replaced by the piezoelectric potential produced by the piezoelectric polarization (P_{PZ}), itself resulting from the mechanical stress applied to the piezoelectric material. An ideal perfectly insulating piezoelectric material can be considered as the simplest example to analyze. For such a material, a mechanical deformation creates a perfuse electric field ideally constant across the material, hence a built-in potential varying linearly across the material. This piezoelectric potential changes the energy levels of the valence band (VB) and the conduction band (CB) across the piezoelectric material,

and in particular at its surfaces, having a dramatic effect on the materials interaction with its environment (Fig. 2- 1). In the absence of piezopotential, the production of $\bullet O_2^-$ and •OH radicals over piezoelectric catalysts such as tetragonal $BaTiO_3$ is not thermodynamically favorable, because of the mismatch between the valence and conduction band levels of $BaTiO_3$ and the required redox potentials for the oxidation of water and the reduction of oxygen. However, a significant piezopotential of 0.45 V within tetragonal $BaTiO_3$ can tilt the band sufficiently to enable the alignment of valence and conduction bands to the redox potential levels as shown in (Fig. 2- 1 (a)). In this model, it is assumed that strain does not change the magnitude of the band gap. If the $e\varphi_{VB}$ approaches $e\varphi_{LUMO}$, it becomes energetically favorable for electrons to leave the VB and enter the LUMO (center panel of Fig. 2- 1 (a)). If the $e\varphi_{CB}$ approaches $e\varphi_{HOMO,}$ it becomes energetically favorable for electrons to leave the HOMO and enter the CB (third panel of Fig. 2- 1 (a)). To simplify this explanation, one can put an imaginary metal electrode with their continuous density of states up to their Fermi energies between the piezoelectric and the solution. In this scenario, the piezopotential acts as a bias, lifting and lowering the metal's Fermi level $e\varphi_M$ (Fig. 2- 1 (b)).

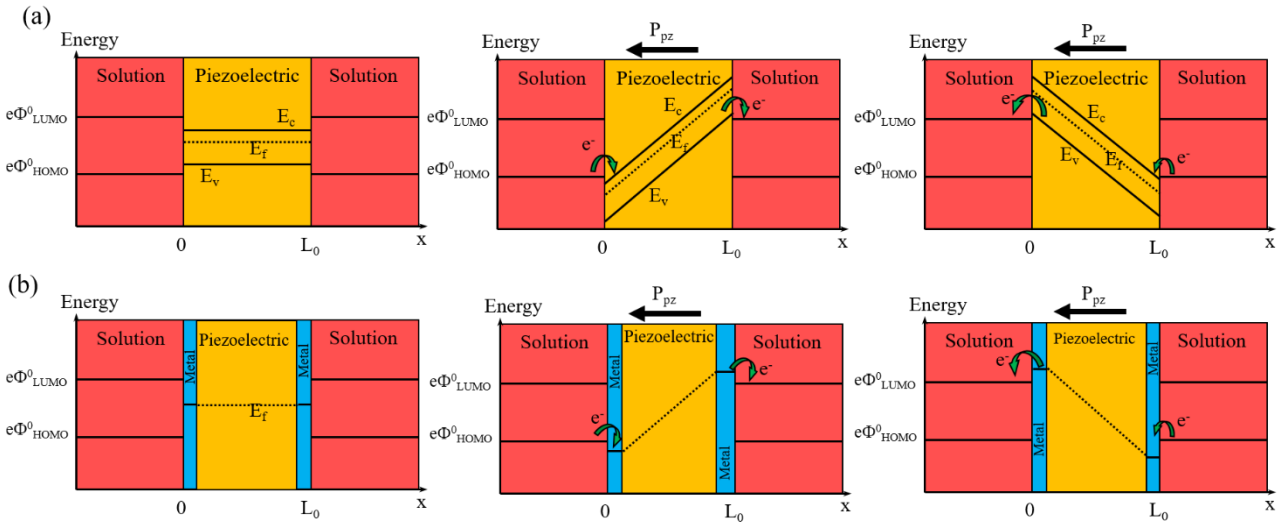

Fig. 2- 1 (a) In the case of a bare piezoelectric, conduction and valence bands act as the reservoirs for electrons donated or accepted from molecules in solution. The piezoelectric polarization (P_{PZ}) applies a variable bias across the material, raising and lowering the valence band and conduction band energies. (b) Adding metal electrodes to the piezoelectric material provides electron reservoirs at a suitable Fermi energy, the piezoelectric potential being the source of bias.

After reviewing the existence of the surface screening charges, let's discuss the surface current density of these charges. In the case of piezocatalysis, the applied stress is the source of the bias via the induced polarization produced by the piezoelectric effect and the built up of a potential across the material. Piezoelectric materials are capable of achieving very high potentials (up to even a few hundred volts) when subjected to a moderate to high strain [62]. We know from electrochemistry that most of the chemical species undergo reduction or oxidation reactions when the potential of the electrodes reaches around 3 V vs. standard hydrogen electrode. In order to quantify the amount of these oxidation and reduction reactions, it is necessary to quantify the interaction between charge exchange at the piezoelectric/electrolyte interface and the effect of the piezopotential on the charge exchange. One main characteristic of the piezocatalytic systems is the piezopotential drop that takes place during charge transfer to (or from) its surface. In this way the system acts as a capacitor, and the piezopotential drop rate is dependent upon both the piezoelectric material's properties and the nature of the solution in which it is immersed. In a simple assumption, if the concentration of the reactive species in solution is low, and the liquid is just pure water for the hydrogen reduction reaction, and the power available for driving electron-transfer reactions is sufficiently high, the rate of the electrochemical reactions at the electrode is dominated by the diffusion rate of the redox specie to the electrode (surface of the piezoelectric material). If we neglect migration and convective phenomena, the flux of species *i* is dependent upon diffusion alone. In the diffusion-limited regime, the maximum rate of transferring electrons from the piezoelectric material should be equal to the rate of reactant diffusing to the piezoelectric. The current density *j* is then given by:

$$J_i(x) = -n_i F D_i \frac{\partial C_i(x)}{\partial x} \qquad (2\text{-}1)$$

Where n_i is the number of electrons per reaction event with species *i*, D_i is the diffusion coefficient of species *i* in the liquid (water in our example), $\partial C_i(x)/\partial x$ is the concentration gradient at distance *x*, and *F* is the Faraday constant [63]. By applying boundary conditions to equation (2-1), considering the capacitive nature of the piezoelectric voltage drop, an expression of the piezopotential V_p as a function of time can be written as follow:

$$\frac{\partial V_p}{\partial t} = -\frac{w_x F \sum_i n_i D_i^{\frac{1}{2}} c_i f_i}{t^{\frac{1}{2}} \varepsilon_0 \varepsilon_{r,x} \pi^{\frac{1}{2}}} \qquad (2\text{-}2)$$

In which w_x is the piezoelectric width in the x direction, f_i is a kinetic parameter that takes a value between 0 and 1 representing the reactivity of electrode with the species i, t is the time, c_i the bulk concentration, and $\varepsilon_{r,x}$ is the in the relative dielectric permittivity in the x direction [50]. If the number of reactants and electrolyte concentrations are low and the positive electrode potential is high ($e\varphi_{LUMo} > 2eV$ vs SHE), a kinetic parameter (f_i) less than 1 causes a semi-diffusion controlled regime to form where charges reactant species (e.g. protons and metal ions) capacitively couple to the electrode's surface, effectively reducing the surface potential before they are electrochemically reduced or oxidized. Under the application of a large positive electrode potential, a dilute liquid system capacitance can be approximated by a Helmholtz model. The variation of the voltage vs. time by both electrons transfer reactions, and capacitive effect can be determined by integrating from the equation (2-2):

$$V_P = -\frac{2Ft^{1/2}}{\varepsilon_0 \varepsilon_{r,x} \pi^{1/2}} \left[w_x \sum_{i=1}^{i=l} n_i D_i^{1/2} c_i f_i + w_H \sum_{i=1}^{i=l} z_i n_i D_i^{1/2} c_i (1 - f_i) \right] \qquad (2\text{-}3)$$

Where z_i is the charge sign (1 for cation, and -1 for the anion) of species i, w_H is the thickness of the Helmholtz layer, w_x is the width of the piezoelectric material, and l is the number of different species in solution. The positive potential of the electrode causes the contribution of the positive charges in solution to result in a positive capacitive current that lowers the piezopotential. The first term in equation (2-3), describes the change in the piezopotential by proceeding the redox reactions, and the second term describes the potential change duo to the capacitive coupling of not yet reacted species at the piezoelectric material's surface. Equation (2-3) determines how the potential on the piezoelectric's wall should drop from the time (t=0) of initial mechanical deformation, when the piezopotential can be a value of tens or hundreds of volts, to a time (t=t_p) when the potential has been reduced to a reasonable value about the SHE (for example more than 2 V vs SHE). Between time t = zero to t_p, there is sufficient electric potential to reduce or oxidize the species within solution in an effective and nonselective manner. At $t > t_p$, the piezoelectric potential is less than the energy difference between $e\varphi_{HOMO}$ and $e\varphi_{LUMo}$ values of ions in solution resulting in a more selective reduction and oxidation process.

2-2-1-1 Charge surface screening mechanism

Theoretically, the dynamic adsorption and desorption behaviors of the screening charges can be well controlled with the modulation of the polarization of the piezoelectric effect. According to this fact, a general working mechanism of the screening charge effect has been proposed [59] based on the $BaTiO_3$. The $BaTiO_3$ is electrically neutral due to the fact that the external screening charges adsorbed to its opposite surface compensate for the bound charges. When it is submitted to stress, e.g. pressure ultrasonic waves, the balance of this charges is destroyed, because the polarization inside $BaTiO_3$ decreases leading to the release of the extra screening charges from the surface. These free charges with sufficient energies facilitate the redox reactions producing different free radicals such as $^{\bullet}OH$ and $^{\bullet}O_2^-$. This process continues until a new balance is reached, and once the applied stress is relieved, the initial built-in polarization is restored resulting in the presence of more polarization bound charges at the surface. Consequently, more screening charges from the electrolyte will be adsorbed on the surface again, temporarily leaving behind charges of opposite polarity in the electrolyte that can then also participate in redox reactions[64]. Briefly, redox reactions can be promoted over the surface of piezoelectric materials via cycles of polarization-induced accumulation and release of surface screening charges.

2-2-1-2 Experimental results favoring the 'Screening charge effect' model of piezocatalysis

The surface electrical properties of materials are affected by the polarization in piezoelectric and ferroelectric materials. Using Kelvin probe microscopy, the local surface electrical states have been detected and mapped by Kalinin *et al* [65]. They have provided fundamental insights about screening phenomenon at the surface of polar surfaces, taking the important and prototypical ferroelectric material $BaTiO_3$ as an example, as shown in Fig. 2- 2. At 25 °C, corrugated surface topography was observed, and the surface potential map shows a uniform potential distribution within single domains at 25 °C, with a potential difference of 150 mV between the adjacent domains of the opposite polarity. These results are indicatives of the polarization of $BaTiO_3$ at room temperature. By increasing the temperature up to 130 °C which is the most recently and most accurately measured value of the Curie temperature of $BaTiO_3$, the surface electrical charge map undergoes important changes: With a different and much more uniform surface topography (Fig. 2- 2 (c)), the mapping of the surface potential in the paraelectric phase is nevertheless very

similar to that of the ferroelectric surface right when images just 1 minute after the temperature exceed the phase transition of $BaTiO_3$. Although the change of polarization is almost instantaneous and so is the change of the polarization -induced bound charge density, the images of the potential at and above T_c change very slowly, demonstrating that it takes longer times to subsequently release the adsorbed surface screening charges until equilibrium is eventually reached again. When this material is cooled from just below the Curie point to lower temperatures, the same behavior can be seen. Such difference between bound charges and screening charges dynamics is schematically illustrated in Fig. 2- 3. It has to be noted that the exact same phenomenon of adsorbed surface screening charges and to compensate for polarization-induced bound charges and their different dynamics occurs not only for ferroelectric materials but for all polar materials, namely also for pyroelectric and piezoelectric materials.

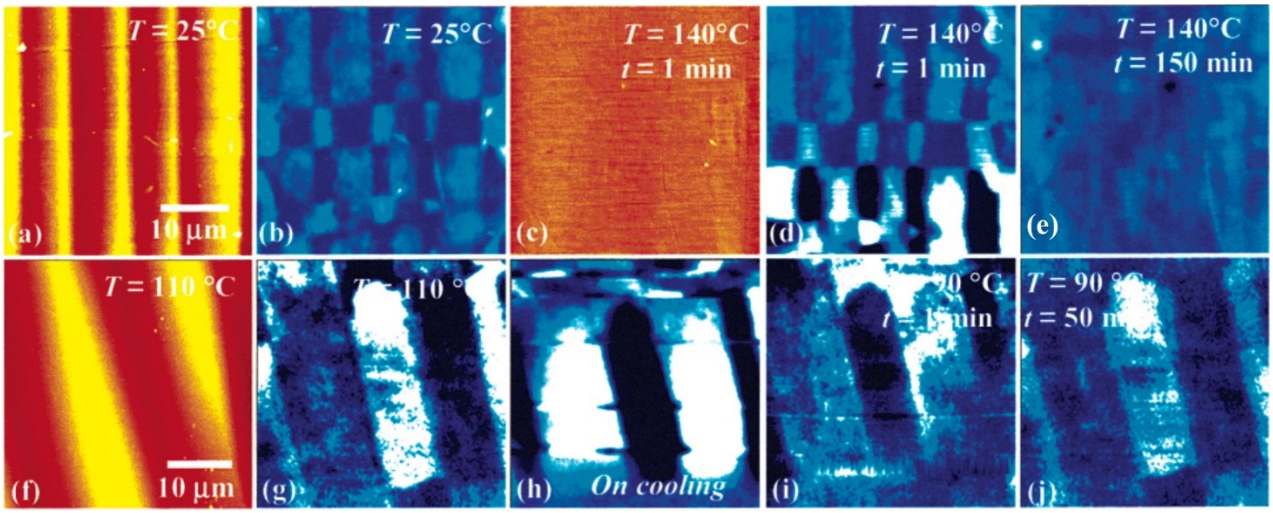

Fig. 2- 2 Surface topography (red) and potential distribution (blue) at the $BaTiO_3$(100) surface (a, b) at 25 °C, before the ferroelectric phase transition, (c, d) at 140°C 1 min after transition, and (e) after 2.5 h at 140 °C. The color scales are (b) 0.1 V, (d) 0.5 V, and (e) 0.1 V. (f) Surface topography and (g) surface potential of the ferroelectric domain structure on the $BaTiO_3$(100) surface at T = 110 °C. Surface potential (h) during cooling from 110 to 90 °C, (i) at 90 °C, and (j) after 50 min. at 90 °C [65].

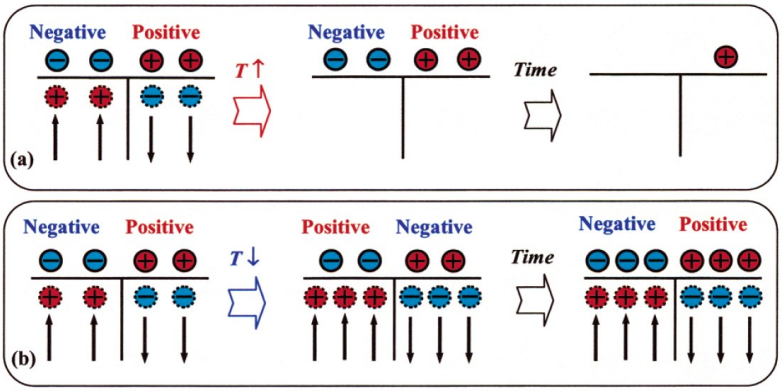

Fig. 2- 3 Charge dynamics on the ferroelectric surface on (a) heating and (b) cooling, illustrating the interplay between fast polarization bound charge (dotted lines) and slow screening charge (solid lines) dynamics as described in the text [65].

2-2-2 'Energy band theory' model

In this model, the photocatalysis process is explained based on the energy band theory and the band structure of the semiconductor material considered. The electrons from the valence band (VB) are excited by the high energy sunlight photons and jump to the conduction band so that a hole (positive charge) is left in the valence band [66]. These photo-induced charge carriers diffuse to the opposite photocatalyst surfaces and then participate in the chemical reactions that proceed on the surface of the photocatalyst material. Despite of the wide band gap of these oxide semiconductors preventing them from harnessing a large part of the visible light, many of these materials possess the capability to generate $\bullet O_2^-$ and $\bullet OH$, the crucial free radicals required to catalyze the redox reactions degrading organic dyes. For example, tetragonal $BaTiO_3$, and anatase TiO_2 with a band gap of around 3.2 eV, can produce photo-excited electrons and holes that facilitate these redox reactions, ultimately leading to the formation of $^{\bullet}O_2^-$ and $^{\bullet}OH$. Many researches have shown that the existence of a piezoelectric potential across the semiconductor does help their transport to the surfaces and consequently help these chemical reactions to process more effectively [67, 68]. This process, which is called piezo-photocatalysis, has been well explained based on the energy band theory. In this theory, the electronic states and the band configuration of the piezocatalyst, in particular the band tilting induced by the piezopotential, are the key factors to govern the catalytic activities. A strong catalytic activity has been reported even without photoexcitation, with the only excitation energy delivered to the catalyst being

ultrasonic mechanical vibrations, the catalytic process being then purely piezocatalysis. Indeed, an extraordinary organic degradation of the organic dye Rhodamine-B by piezo-photocatalysis has been reported using n-type MoS_2 platelets-like structures (dubbed nanoflowers by the authors) [69]. This strong catalytic effect was explained by the high electron concentration (4.04×10^{15} cm^{-3}) and electron mobility (2.9 $cm^2V^{-1}s^{-1}$) in the MoS_2 nanoflowers. In this model, the electrons and holes are excited by the energy of the photons, and the additional induced piezopotential drives the charge carriers toward the surface of the piezoelectric materials where they then take part in the redox reactions. It is believed that a significant source of charge carriers in piezocatalysis is the presence of the defects within the structure of the piezoelectric catalyst. Typically, the anion defects such as oxygen, selenium, and sulfur vacancies in the transition metal oxide and dichalcogenides can generate free electrons that can move easily to the surface driven by the piezopotential [70]. Many studies on piezocatalysis in the recent years have been dedicated to defect engineering of the piezoelectric nanostructures, which has led to a substantial enhancement in the piezocatalytic activities [71]. However, most of this research do not discuss the relative importance of the free charge concentrations and the piezoelectric effect in the analysis of the reported piezocatalytic process.

In a typical piezocatalytic process which is specifically runs in dark without the possibility of photo-excitations, the source of the charge carrier is indeed still subject of debate [72]. Due to the complexity of the piezocatalysis systems reported, which usually include the use of ultrasonic baths, it is likely that some charge carriers are excited directly due to other processes taking place simultaneously, such as sonolysis (sonocatalysis), or even triboelectric effects. For instance, In sonolysis, there is a possibility of the charge carrier excitations due to the local high pressure, high temperature, and even light production, well documented in the process called sonoluminescence [73]. The collapse of the ultrasonic-induced cavitation bubbles may also generate locally a very high pressure of up to around 10^8 Pa at the interface of the bubbles and water, where the catalysts may be located. Such a s pressure has been shown to induce a piezoelectric potential of as big as about 0.45 V around the $BaTiO_3$ particles. This high pressure has been reported to have enough energy for direct electron excitations [13, 74, 75]. Other reports come up with alternative models to explain the charge carrier excitations, such as vibration-induced thermal excitations. The ultrasonic collapse of the cavitation bubbles could lead locally hot spot (up to 5000 ^oC) near the surface of the piezocatalyst, which would also

release enough energy to promote electrons from the valence band to the conduction band [76]. Experimentally, Edward Flint et al showed that the transient temperature of the cavitation bubbles was able to weld together metallic particles dispersed in an ultrasonic bath, suggesting that the temperature generated by the cavitation bubbles at the time of their collapse exceeds a few thousands Kelvin [44].

2-2-2-1 Experimental results favoring the 'Band energy theory' model of piezocatalysis

Some critical questions remain about the capability and selectivity of piezocatalysis in different chemical reactions, that are difficult to explain by the screening charge model and would favor understanding piezocatalysis using the 'Band energy theory' model. For example, in the generation of H_2 by reduction reaction processes, the production of different ROS, e.g. of H_2O_2, can be selectively achieved with different piezocatalysis setups with the possibility of collecting H_2 gas [59, 72, 77, 78]. In order to investigate the intrinsic factors, some theoretical simulations and experiments to test the piezoelectric and piezocatalytic activities of $BaTiO_3$ with different particle sizes and morphologies have been reported [77]. Using piezoresponse force microscopy (PFM) from the a surface of the superfine $BaTiO_3$ nanocubes with sizes of 10 nm, a strikingly superior longitudinal piezoelectric coefficient of 0.45 nm V^{-1} was obtained, while for the bigger sizes nanocubes (200 nm), and nanowires, the relative results were measured to be 0.06 and 0.09 nm V^{-1}, respectively (Fig. 2- 4 (a)). As a consequence of their piezoelectric coefficients, the peaks surface piezopotential values calculated from the finite element modeling were obtained to be 2.6, 0.5, and 1.2 V for 10 nm, 200 nm and nanowires, respectively. From these three sizes and shapes, only the 10 nm $BaTiO_3$ cubic samples exceeds the required redox reaction potential (1.23 V), and as shown in Fig. 2- 4 (d), it also shows the best piezocatalytic activities among those three nanostructured samples. It means that the induced piezopotential should reach the Gibbs free energy threshold of the water splitting to be able to promote the redox reactions yielding H_2 or any kind of organic decomposition. These results show that the engineering of the structure and morphology to optimize the surface mobile charges is of high importance in piezocatalysis.

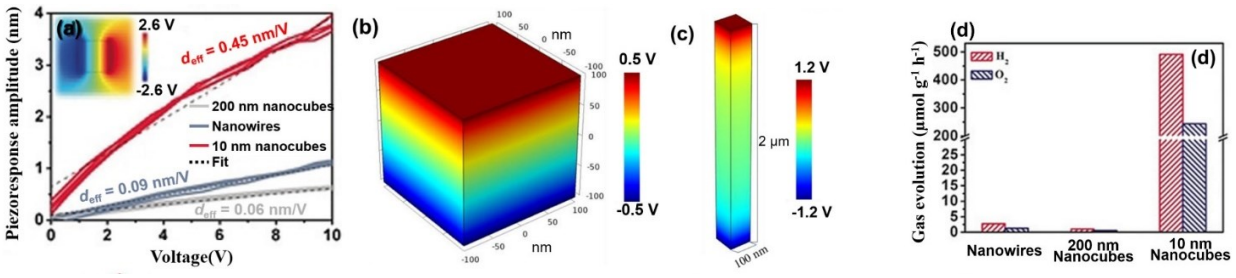

Fig. 2- 4 (a) Comparative quantitative piezo-response amplitude measurements versus bias for 10 nm $BaTiO_3$ nanocubes, 200 nm $BaTiO_3$ nanocubes and $BaTiO_3$ nanowires. The inset shows the distribution of electric potential in 10 nm $BaTiO_3$ nanocubes by COMSOL simulation. The distribution of piezopotential in b) 200 nm $BaTiO_3$ nanoparticles and c) nanowires. d) The rate of H_2 and O_2 production by piezocatalytic water splitting [77].

In another model developed by Amaechi *et al* [79], a model based on of $BaTiO_3$ nanorods was used to make an estimation of the piezopotential. This model basically neglects the water conductivity and shock waves originating from the bubbles. With this simplification the pressure of the acoustic wave in the linear regime can be written as below:

$$p = \sqrt{P/_A}\,\rho c \qquad (2\text{-}4)$$

where P/A, ρ and c are the power density, fluid density, and the speed of sound, respectively. Assuming the maximum power density for the steady situation (and still neglecting the bubbles shockwaves) which is $p_a = p_0 = 1$ bar, the power density P/A yields 0.68 W/cm^2. Since the frequencies of the ultrasonic waves typically range between 20 kHz-1 MHz, and the speed of sound is 1480 m/s , this yields a wavelength of the acoustic waves between 1.5-74 mm. It is noted here that the absorption of the ultrasonic waves with higher frequencies is larger as the absorption loss increases with the square of the frequency [80]. Assuming the existence of a pressure gradient in the liquid that is related to the acoustic pressure by the following formula:

$$\frac{\partial p}{\partial z} = 2\pi f p_0 / c \qquad (2\text{-}5)$$

The induced piezopotential obtain from the hydrostatic pressure, pressure gradient for both uniaxial and shear forces have been calculated and is shown in Fig. 2- 5. The results of this calculations reveal that the maximal induced piezopotential for a typical frequency of 100 kHz is just 0.8 mV, which is about one order of magnitude lower than that of the typical potential needed for redox reaction. However, the piezopotential effect is probably under-estimated in this

model, since it does not consider the cavitation bubble collapse effects, which could possibly be quite significant.

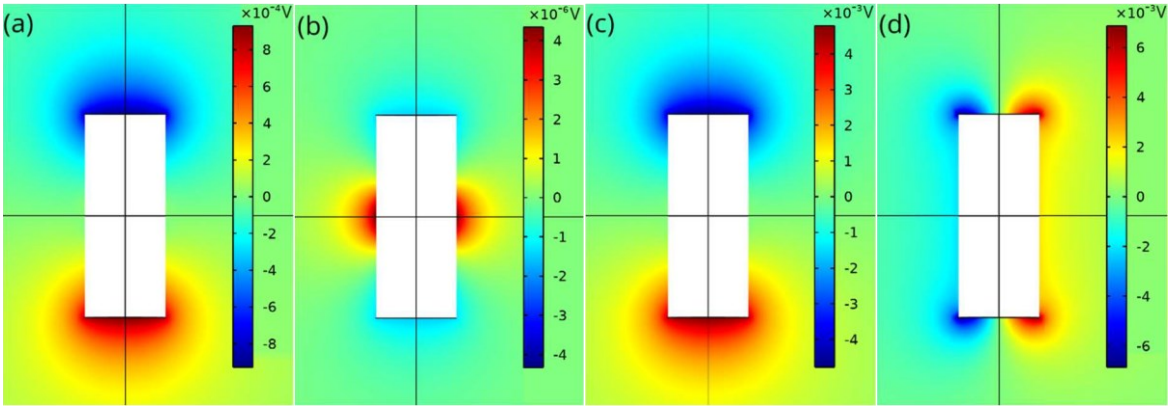

Fig. 2- 5 Simulation of piezopotential around the $BaTiO_3$ nanorods dispersed in water under (a) hydrostatic pressure p_0, (b) the pressure gradient of $\frac{\partial p}{\partial z} = 2\pi f p_0/c$, (c) with the uniaxial pressure p_0, (d) at the shear force p_0 [79].

2-3 Piezocatalytic reactions

One type of pollutant often used in studies about wastewater treatment is organic dyes. This is because they are quite widely used in the textile industry and therefore are actually found in wastewater and also because they are conveniently, by their very nature as dyes, visible to the naked eye and their colour (or the intensity or vibrance of their colour) is also noticeably changing as they degrade and their concentration in water changes. The most common approach to investigate the kinetic of degradation of organic dyes pollutants is to measure the optical absorbance of the contaminated water during the catalytic process. In this regard, typical dyes such as Rhodamin B, Methyl orange, and methylene blue are most convenient owing the simplicity of their degradation investigations even with the naked eyes (These organic compounds have specific absorption peaks in the range of the visible light). Two types of organic dyes exist based on their electron affinity: anionic and cationic dyes. A standard catalyst should literally be able to degrade both types of organic pollutants. Fig. 2- 6 shows the absorbance spectra of the water contaminated with different organic dyes at different moments in time during their piezodegradation. These results that were obtained usinge Sm-doped (1–

x)Pb($Mg_{1/3}Nb_{2/3}$)O_3-x$PbTiO_3$ piezoelectric nanoparticles as catalyst of the degradation reactions and shows their suitability for different types of anionic and cationic dyes [81].

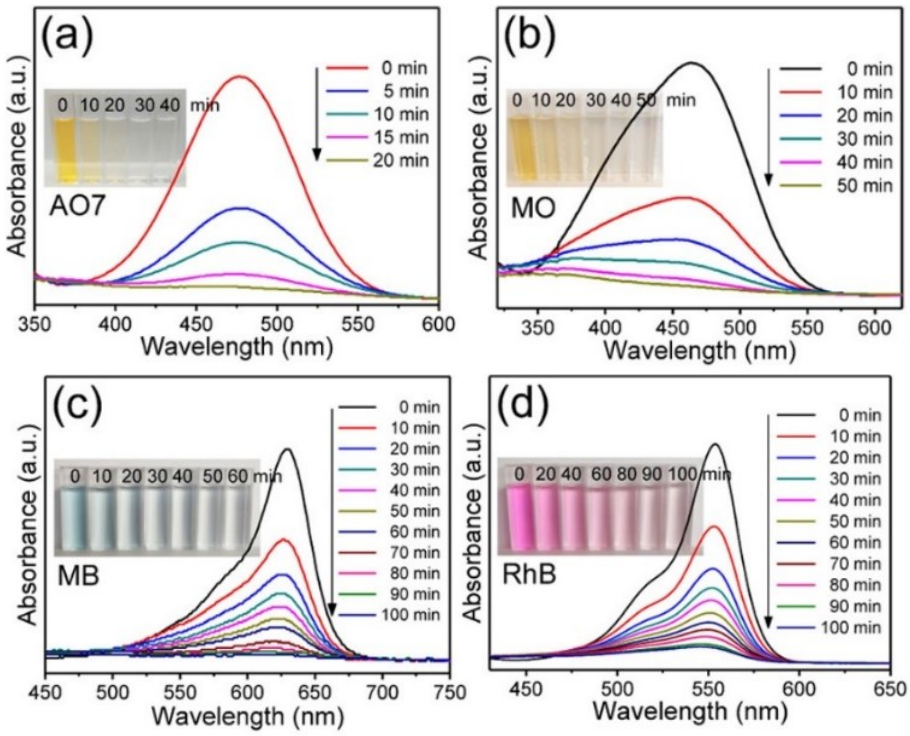

Fig. 2- 6 Absorption spectra from contaminated water containing (a) acid orange 7 (AO7), (b) methyl orange (MO), (c) methylene blue (MB), and (d) rhodamine B (RhB) at different sonication times using Sm-PMN-0.30PT catalyst nanoparticles; the insets display the corresponding photographs of dye solutions [81].

Similar optical absorption techniques and organic dyes are used for performing standard degradation measurements in photocatalysis *[82]*. It has also been shown that ultrsonication using piezoelectric nanocatalists can be applied in a hybrid process in which it synergistically enhances the degradation rate of the organic pollutants, a process then called pizo-photocatlysis *[83-85]*. According to the band energy model which is used to explainboth piezo and photodegradation processes, the electron-holes excitations by the sunlight radiation can better reach the surface of the catalysts when a piezopotential is induced simultaneously to the piezocatalyst particles. Piezopotential genration is reported to enhance the photocatalytic degradation rate between one to two orders of magnitude according to the recently published literature. Fig. 2- 7 (a) shows a typical photocatalysis kinetic measurements of the degradation using ZnO nanoparticles as catalyst agents *[86]*. The intensity of the absorption peaks of the methylene blue, which are located at 615 and 662 nm, decreases with the time of solar

irradiation. However, Fig. 2- 7 (b) shows that when ultrasonic waves are added to this setup, it clearly enhances the degradation process so that after 20 min. the intensities of this peaks almost completely vanished confirming the degradation of methylene blue as also shown on the corresponding photographs.

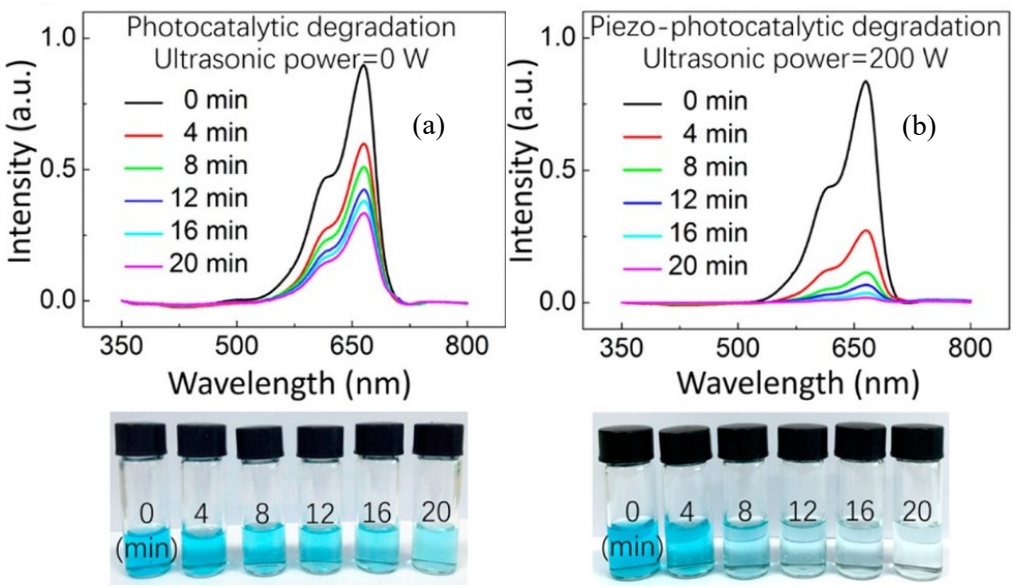

Fig. 2- 7 Piezo-photocatalytic activities of CuS/ZnO nanowires grown on stainless steel mesh for the deradation of methylene blue under different experimental conditions: (a)absorption spectra of methylene blue under photodegradation only, without ultrasonication. The inset shows images of the corresponding liquids at different times. (b) The absorption spectra of methylene blue under photodegradation with the added ultrasonication. The inset also shows images of the corresponding liquids at different times [86].

One of the main issues about the piezocatalysis activities in an aqueous medium is to establish the chemical reactions and the reactions pathways that yield the removal of the organic pollutant. Reviewing the literature reveals that the chemical reactions in water beside the piezoelectric materials are quite complex, so that there is no unique answer to that, as different pathways depending on the experimental setup have been suggested. One of the main questions here is to determine the active free radicals directly produced during the generation of the piezopotential across the piezocatlyst particles present in the aqueous solution. The importance to establish the details of these reactions is making sure that the degradation of the organic dyes does not yield another toxic compound that would be dangerous for the environment. The main reactive oxygen species (ROS) in such these experiments would be O_2^- (superoxide), •OH (Hydroxyl radical), or even $^1O_2$ (singlet oxygen). Depending on the experimental setup, piezocatalysis material, and on

the organic dyes, the following reactions have been suggested and are likely in the vicinity of the piezocatalysts [87, 88]:

$$Piezo \xrightarrow{ultrasound} Piezo + e^- + h^+ \quad (2\text{-}6)$$

$$O_2 + e^- \rightarrow O_2^{\cdot -} \quad (2\text{-}7)$$

$$H_2O + h^+ \rightarrow H^+ + HO^{\cdot} \quad (2\text{-}8)$$

$$H_2O + e^- \rightarrow OH^- + H^{\cdot} \quad (2\text{-}9)$$

$$O_2^{\cdot -} + HO^{\cdot} \rightarrow OH^- + {}^1O_2 \quad (2\text{-}10)$$

$$O_2^{\cdot -} + h^+ \rightarrow {}^1O_2 \quad (2\text{-}11)$$

$$2O_2^{\cdot -} + 2H^+ \rightarrow H_2O_2 + {}^1O_2 \quad (2\text{-}12)$$

$$H_2O_2 + HO^{\cdot} \rightarrow HOO^{\cdot} + H_2O \quad (2\text{-}13)$$

$$HOO^{\cdot} \rightarrow O_2^{\cdot -} + H^+ \quad (2\text{-}14)$$

The primary products of the chemical reactions pathways can be determined by scavenging experiments, while the intermediate reactions that yields the discosiation of the organic dyes may be characterized using liquid chromatography−mass spectrometry (LC-MS). One typical pathway of the organic degradation suggested for the degradation of methyl orange using $BaTiO_3$ piezocatalyst nanoparticles is shown in Fig. 2- 8 [18].

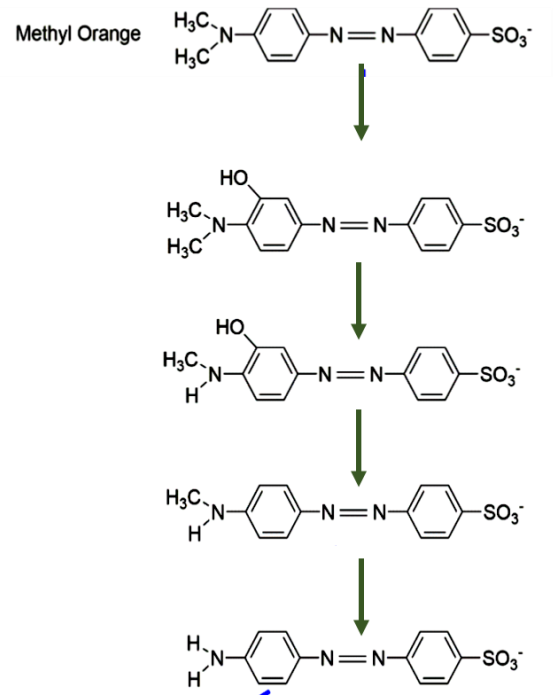

Fig. 2- 8 a typical pathway suggested for the degradation of methyl orange using $BaTiO_3$ nanocatalysts [18].

2-4 Piezocatalysis candidates

As was mentioned in the first chapter, the main characteristic of piezoelectricity is to have non-centrosymmetric structure. Among the piezoelectric materials, only a small number of them have demonstrated strong and consistent piezocatalytic activity. Many efforts have been made on engineering the morphology and the structure of the piezoelectric material in order to enhance their piezocatalysis performance. With the general formula ABX_3, many of these piezoelectric candidates with perovskite structure have shown good and reliable piezocatalysis performance. These materials consist of arrays of face-sharing metal (B)-halogen (X) octahedra separated by organic molecule cations A. The main feature of these organic perovskites is that their molecular cations at A sites can rotate and doing so magnifies the polarization of these types of structures beyond values of polarization that has been obtained with traditional perovskites. Recently, a giant piezoelectric coefficient has been observed in organolead halide materials with perovskite crystal structure[89]. The crystalline structure of $CH_3NH_3PbI_3$ (MAPbI) has demonstrated a high efficiency in the production of hydrogen through a piezocatalysis process [57]. Both the elements in the A and B sites in the perovskite crystal may influence the polarization of the whole

structure, but the polarization of ABX_3 can be particularly well manipulated with the composition, structure and orientation of the molecular cations, and [90].

Many of the inorganic perovskite oxide piezoelectric materials with the general formula ABO_3 are the candidates that have been extensively investigated for piezocatalysis applications. Among the perovskite oxides, $BaTiO_3$ is recognized as a prototypical perovskite structure, and due to the fact that it both have excellent dielectric and piezoelectric properties and that it is a lead-free piezoelectric material, it is the piezoelectric material of choice that has been suggested and studied in most the piezocatalysis investigations. Barium titanate has been of practical interest for more than 70 years due to its numerous useful properties (high dielectric permittivity, piezoelectricity, ferroelectricity), resulting from its spontaneous electric polarization properties at room temperature. One of the main features of $BaTiO_3$ is that due to its lead-free nature, it is an environmentally friendly candidate that has gotten special attention among other perovskite candidates. At room temperature, its piezoelectric constants d_{15}, d_{33}, and d_{13} have been measured to be 392 pm/N, 85.6 pm/N, and -34.5 pm/N, respectively [91]. The tetragonal phase of $BaTiO_3$, which is the non-centrosymmetric phase, is ferroelectric (hence piezoelectric) and possesses a spontaneous polarization that is stabilized up to the temperature of around 130 ^oC (Fig. 2- 9). At this temperature it undergoes a phase transition from tetragonal to cubic that causes the disappearance of its spontaneous polarization at higher temperatures. The elongation of the $BaTiO_3$ crystal in one direction is representative of its tetragonality and is a function of temperature. It decreases when the temperature increase from the room temperature up to its phase transition temperature, called Curie temperature T_C [92]. The $BaTiO_3$ phase transition in polycrystalline ceramics has also been reported to be dependent on the size of the grains and ferroelectric domains, so that by decreasing the size of $BaTiO_3$ particles down to a few nanometers, the tetragonal-to-cubic phase transition temperature (the Curie temperature T_C) can be decreased down to around 70^oC [8]. Since the size of the ferroelectric domains depends on the particles sizes too, when decreasing the sizes of the $BaTiO_3$ nanoparticles their dielectric permittivity and piezoelectric coefficients decrease as well [5]. It is also noteworthy to mention that another phase transition from tetragonal to rhombohedral symmetry exist at lower temperatures, around 10^oC.

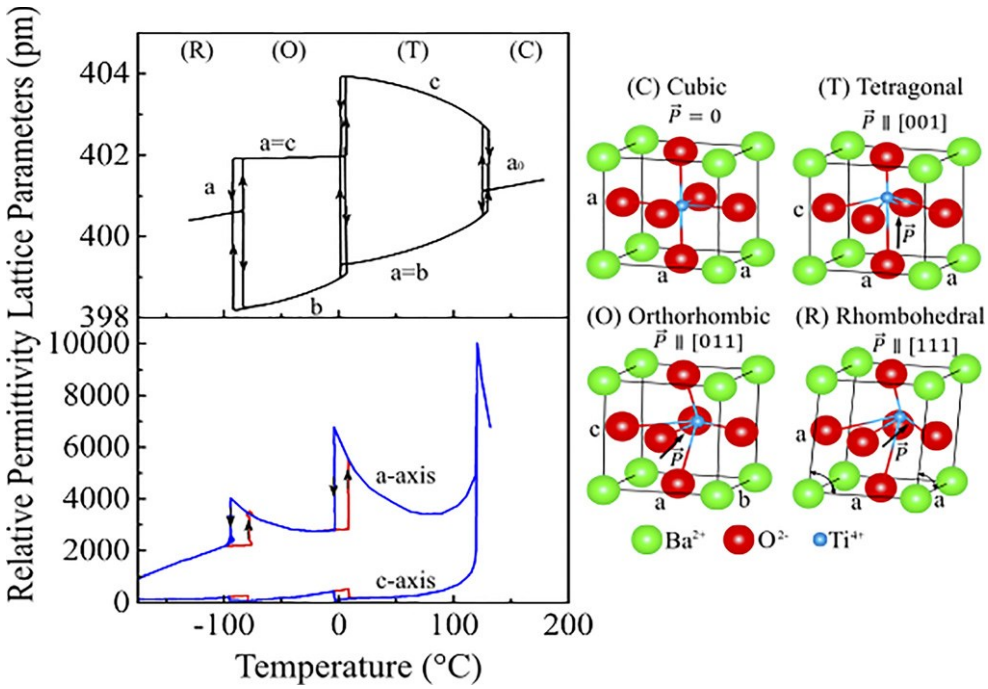

Fig. 2- 9 Changes in primitive-cell lattice parameters and anomalies in relative permittivity ($\varepsilon_r = \varepsilon'/\varepsilon_0$) during the sequence of phase transitions in $BaTiO_3$ [92].

Some other perovskite oxide candidates such as $SrTiO_3$ [35], and $KNbO_3$ [93] have also been suggested for potential application as piezocatalyst materials. Also, piezoelectric materials that do not have a perovskite structure have been studied and a promising piezoelectric candidate for piezocatalysis applications is ZnO, having a hexagonal wurtzite crystal structure. Owing to its different crystal structures (wurzite, zinc blende and rock salt) and morphologies, ZnO is a great candidate for trying to obtain high surface to volume via crystal engineering, in order to enhance its catalytic reaction performance. Like $BaTiO_3$, it is also a low cost and environmentally friendly piezoelectric candidate.

2-5 Generation of mechanical stress and related strain in the piezoelectric catalyst particles

In order to generate bound charges on the surface of the piezoelectric catalysts and a piezoelectric potential across the particulates, the piezoelectric catalyst particulates need to be submitted to a mechanical stress. The energy conversion from mechanical energy to electric is expressed by the piezoelectric coefficients, which in turn have a determining impact on the

efficiency of the piezocatalysis processes. Different mechanisms can be used to generate this mechanical stress and related strain onto the piezoelectric particulate catalysts, some of which will be discussed in more detail in the following.

2-5-1 Ultrasonic Vibrations and Cavitation

The main technique t used to induce a piezoelectric effect in the particulate catalyst is the use of ultrasonic vibrations or ultrasound waves in a frequency range of 37 to 45 KHz commonly used for ultrasonic cleaning (i.e. much lower than for ultrasonic imaging usually done with frequencies of 2 -18 MHz). The ultrasound are generated in a liquid bath and are energetic enough to produce cavitation bubbles, whose collapse generates large pressures(estimated to be up to 10^8 Pa) on the piezoelectric particulates dispersed in the liquid bath[13]. Therefore, surface bound charges and a piezoelectric potential are generated periodically across the piezocatalyst particles in suspension. Obviously, increasing ultrasonic power enhances catalytic efficiency. Frequency and amplitude of the ultrasounds, as well as the resonance frequency of the particulate catalysts are also important factors in this process. For nanosheets, the resonance frequency (f^r), which depends on length (L), width (W), density(D) and bending stiffness (ρ) can be calculated via the following equation:

$$f^r = \frac{\pi}{2}\left[\frac{1}{L^2} + \frac{1}{W^2}\right]\sqrt{\frac{D}{\rho}} \qquad (2\text{-}15)$$

The resonance frequency f^r for nanosheets of $BiFeO_3$ has been estimated to be about 46.5 kHz and the hydrogen production rate of $BiFeO_3$ at this ultrasonic frequency was shown to exceed that at any other frequency [94]. The total pressure generated inside the liquid by the ultrasonic vibrations waves in the linear regime can be written as:

$$\mathrm{p}(t) = p_0 + p_a sin(2\pi f t) \qquad (2\text{-}16)$$

In which p_0 and p_a are the static and driving pressures, respectively, and f is the frequency of the ultrasonic waves. The above formulation is only valid for the small ultrasonic driving pressures ($p_a \leq p_0$), where the mechanical response from the fluid is linear on the applied mechanical pressure from the ultrasound. When larger pressures are produced from the ultrasound waves (this can be obtained with higher powers of the ultrasonic waves generator), the dynamic

pressure may lead to the production of acoustic cavitation in which the dissolved gas nuclei grow in the liquid into microbubbles and subsequently collapse in a very short time. This adiabatic-like collapse generates local shockwaves, and temperature spikes up to thousands of kelvins within 100 picoseconds [44] that causes electron-hole excitations in semiconductors, and possibly direct redox reactions in water. This cavitation phenomenon can therefore promote chemical reactions and the degradation of the organic pollutants through a process called sonocatalysis [46, 95]. The local pressure of the water around the cavitation bubbles when they collapse and generate shockwaves has been estimated to be around 40-60 kbar [96]. The variations of pressure directly generated by the ultrasonic waves can also induce polarization in the piezoelectric catalyst particles dispersed in liquid via the piezoelectric effect.

2-5-2 Vortex-induced shearing force

Since there are few ultrasonic resources available in nature, which limits the applications of ultrasonication to promote reaction by piezocatalysis, it is meaningful to develop piezocatalytic processes using low-frequency vibrations instead of ultrasounds. One example for this case would be the mechanical energy from vortex in fluids [97]. A vortex is a whirling mass of water/fluid/air that therefore has some mechanical rotational kinetic energy associated with it. Some of this energy could therefore be transferred to the piezoelectric particles present in the fluid via interactions with their surface, in particular their surface irregularities. According to the Newton's viscosity law we have:

$$\tau = \mu \frac{\partial u}{\partial \gamma} \qquad (2\text{-}17)$$

Where μ is the viscosity coefficient of the liquid, and $(\partial u/\partial \gamma)$ is the derivative of the liquid velocity u. The shear force (τ) is equivalent to the applied stress (η) along the y-direction. Vortex-induced vibration gives low frequency shocks to the attached systems (contaminated liquid etc); thus, only highly sensitive piezoatalytic materials possessing hierarchical structures can give rise to optimum catalytic efficiency. According to this equation, one can determine the relation between the flow rate $(\partial u/\partial \gamma)$ and the induced piezopotential. It has been shown that the degradation rate of the Rhodamine B (RhB) over spherical lead zirconate titanate (PZT) has been improved by increasing the stirring speed [98]. The reactive oxygen species (ROS) monitored in

these experiments have shown a clear relationship with the shear forces [99]. It has been shown that the efficiency for transferring the fluid mechanical energy to the piezoelectric materials can be significantly enhanced when the surface of the latter is corrugated with hierarchical structures. The hybrid system of ZnO nanorods over Ni foam has shown an excellent piezoelectric response to the mechanical energy generated using vortices rather than that of the ZnO/ITO or ZnO/glass systems [100].

2-5-3 Physical bending

With certain frequency and amplitudes, it has been shown that physical bending of piezoelectrics may also be applicable for the design of piezocatalysis experiments. For instance a cantilever of ferroelectric $Pb(Mg_{1/3}Nb_{2/3})O_3$-$PbTiO_3$ has been used to generate a piezoelectric potential for the evolution of H_2 [101]. Putting the cantilever in a circuit, 10 V peak voltage was detected on the electrode under mechanical oscillations. The induced piezopotential using this method was used as a source of a periodic bias voltage in electrochemical catalysis reactions. The output voltage verified that the piezopotential was thermodynamically capable of driving H^+ reduction reactions. The frequency and amplitude of the oscillations of the cantilever were critical parameters controlling the H_2 evolution rate. Also, the dependency of the H_2 generated per oscillation was calculated as a non-linear function of the piezoelectric potential. The electrochemistry's Bulter–Volmer equation relates well the current density with the piezopotential generated during the oscillation [101], which proves the similarity of the mechanism of the H_2 generated with to the electrocatalysis process. Since both ultrasonic cavitation and vortex-induced shearing forces need liquid media, physical bending of a cantilever may have promising applications for utilization of piezocatalysis in air or other dry media.

Chapter 3 Materials and Methods

3-1 Introduction

The experimental setups used for this research are introduced and fully detailed in this chapter, along with the materials, techniques of the synthesis and characterizations employed.

3-2 Materials

The Commercial materials, utilized in this research are all detailed in the table below:

Table 3- 1 Chemical materials used in this research (NPs = nanoparticles)

Material	**Provider**	**Purity**	**Product No.**
$BaTiO_3$ NPs- 50 nm	Sigma Aldrich	99.9%	745952
$BaTiO_3$ NPs- 100 nm	Sigma Aldrich	>99%	467634

$BaTiO_3$ Particles- 2 µm	Sigma Aldrich	99.5%	338842
Ammonium hydroxide solution	Sigma Aldrich	>99.99 %	338818
Barium hydroxide octahydrate	Sigma Aldrich	>98%	B2507
TiO_2 NPs-100 nm	Sigma Aldrich	99.9%	637262
Methyl orange	Sigma Aldrich	85%	114510
Rhodamine B	Sigma Aldrich	>95%	R6626
Tert-Butanol	Sigma Aldrich	>99.5%	471712
p-Benzoquinone	Sigma Aldrich	>98%	B10358
ethylenediaminetetraacetic acid	Sigma Aldrich	>98%	03620
Hydrogen peroxide	Sigma Aldrich		216763
Manganese acetate tetrahydrate	Sigma Aldrich	99%	221007

3-3 Microwave-assisted Hydrothermal synthesis

The microwave-assisted hydrothermal synthesis method has been widely used for synthesis of nanostructures. The synthesis process in this method is undoubtedly one of the fastest methods among different chemical and physical synthesis processes. Compared to the conventional hydrothermal method with a processing time of around 10 hours, the processing time in the microwave assisted hydrothermal method does not usually exceed more than 10 minutes [102]. The microwave-assisted hydrothermal method accelerates the crystallization of the products and is energetically more efficient than the conventional hydrothermal method [103]. This method is also considered cost-effective. Although the liquid temperature and pressure in the autoclave are not directly controlled during the synthesis process, the microwaves' power can indirectly provide a good estimation of these two parameters. Unlike the solid-state reactions that need very high temperature (including processing or post-processing temperatures), the hydrothermal synthesis is usually performed at temperatures ranging between 100°C and 200 °C. The

microwave-assisted hydrothermal utilizes the in-situ microwave energy to produce autogenic pressure assisted by the rapid heating of the content in an enclosed system. Microwaves are non-ionizing electromagnetic radiation with frequency roughly between 1 GHz and 1000 GHz (sometimes also described as a range from 0.3 GHz to 300 GHz). The microwave frequency used for our synthesis was2.45 GHz (the regulated licensed frequency for microwave ovens corresponding to the wavelength of 12.24 cm) with a penetration depth of several cm depending on their moisture (~1 cm for material with high moisture to 10 cm for dry materials). The mechanism is basically due to the interaction of the dielectric materials (either liquid or solid) with the microwave radiation. The higher the microwave frequencies, the smaller the penetration depth for the microwaves, which are mostly absorbed to the surface of the dielectric materials, while materials are transparent to and the lower frequencies. The cationic and anionic precursors precipitate the oxide perovskite materials in the micro and nano-sized forms during a single step at the temperatures higher than 100 ^{o}C and the pressure of more than 0.1 MPa [104]. The time of the phase selectivity significantly decreases duo to the fact that the rate of the nucleation enhances by using this method [105]. A schematic picture of a standard microwave oven, similar to the one used in our syntheses is shown in Fig. 3-1. It has to be emphasized that the hermetically closed vessel containing the liquid with the chemical precursors of the synthesis reactions should be made of a dielectric material allowing the penetration of the electromagnetic waves so they can reach to the reactive materials.

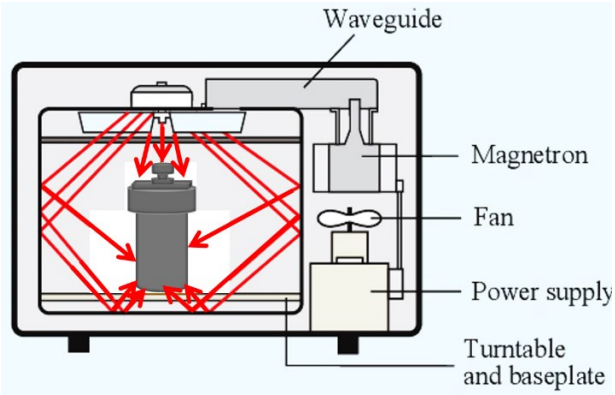

Fig. 3-1 the schematic illustration of a microwave and a standard autoclave to synthesis nanoparticles,

3-4 $BaTiO_3$ Synthesis procedure

The general recipe for synthesis of $BaTiO_3$ nanoparticles using microwave assisted-hydrothermal method is according to the following procedures: The volume fill factor, power level, and microwave radiation exposure duration are parameters depending on the internal pressure and temperature of the geometry of the microwave hydrothermal reactor vessel. As a result, for the 232 mL Teflon vessel used for the $BaTiO_3$ particles synthesis, the mixture's volume fill factor was set at 0.52. As chemical precursor and source for titanium, 50 mmol of titanium butoxide was added to 5 mL of ethanol while being continuously magnetically stirred. In the case of impurity-doped $BaTiO_3$, the molarity of the dopant was adjusted with the molarity of titanium (for example Mo 5% doped in $BaTiO_3$ means that the ration of the Mo molarity was 5% of that of Ti), and both titanium butoxide and the impurity were added to the emulsion at the same time. In the case of controlling the size of the BaTiO3 nanoparticles, PEG (polyethylene glycol) has been used. In this process, $BaTiO_3$ precursors are mixed with PEG in a suitable solvent, and the mixture is then subjected to microwave irradiation under hydrothermal conditions. The PEG molecules attach to the surface of the growing $BaTiO_3$ nanoparticles, and this prevents further growth by making a barrier for the growth. The size of the particles can be controlled by adjusting the molecular weight and concentration of PEG. A higher concentration of PEG results in smaller particle size because more PEG molecules are available to bind to the surface of the growing nanoparticles. Additionally, the molecular weight of PEG can also affect the particle size. Higher molecular weight PEG can result in larger particles due to the increased steric hindrance. Therefore, by adjusting the concentration and molecular weight of PEG, it is possible to control the size of $BaTiO_3$ nanoparticles synthesized by microwave-assisted hydrothermal method [8].

After 10 minutes, the chemical precursor and barium source, namely 75 mmol of $Ba(OH)_2.8H_2O$ was diluted in 5 mL of hot distilled water (>90 °C), and added to the mixture together with 2 mL of H_2O_2 acting as a hydrogen scavenger. Prior to being transferred to a 23 mL Teflon container, the solution was stirred for an additional 10 minutes to ensure homogeneity. The Teflon container was sealed in a Parr Instrument microwave acid digestion PTFE vessel, and microwave-heated for 4 minutes at 360 W in an Inverter Microwave Oven (2.45 GHz). The vessel was then let to cool down to room temperature, and the final product was then rinsed in hot distilled water

before letting it dry for 15 hours in an oven set at 80 °C. To disperse the particles that have agglomerated during the drying process, all samples were ground for 15 minutes.

3-5 Characterization techniques

3-5-1 X-ray diffractometry

X-ray diffractometry provides useful information regarding structural crystallography and also the grain sizes of the nanostructured materials. The incident X-ray photons interact with the crystal lattice when a monochromatic X-ray beam is shined on it and scattered in different directions. However, the scattered light only produces constructive interference at specific angles (theta), dependent on some lattice characteristics (namely, the interplanar distances) and the wavelength of the x-ray radiation [106]. This is schematically shown in Fig. 3-2 (a) and is described by the Bragg's law. Bragg's law defines the scattering angles according to the d, distances between a series of parallel crystallographic planes and λ, the X-ray wavelength:

$$n\lambda = 2d\sin\theta \qquad (3\text{-}1)$$

θ is the angle of the diffraction, and *n* is an integer number characterizing the order of the diffraction. In this project, XRD measurements were performed using the D8 Bruker advanced diffractometer with a Cu X-ray tube operating at 40 kV and 25 mA, using the CuKα line (λ = 1.5406 Å) at the ambient condition. The configuration of this XRD system including incident X-ray beam, detector, and sample holder is shown in Fig. 3-2(b).

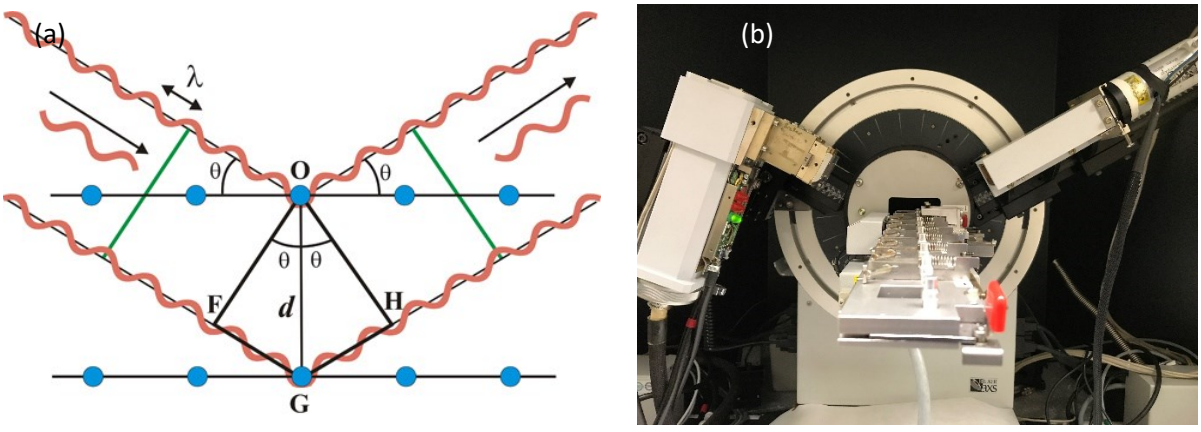

Fig. 3-2 (a) Schematic diagram of the constructive interference of the X-ray scattered waves. (b) The configuration of the XRD Bruker system.

3-5-2 Raman Spectroscopy

Based on the Raman effect, Raman spectroscopy is a non-destructive optical spectroscopic technique. In Raman spectroscopy, inelastic scattering occurs: a specific amount of vibrational energy, corresponding to a specific local mode of vibrations (of angular frequency (ω_{vib}) of the material under investigation is either acquired from (Stokes Raman scattering) or lost to (Anti-Stokes Raman scattering) the energy of the incoming photon ($\hbar\omega_0$). In the first case, the material goes from its fundamental energy state to a virtual state at a much higher energy (corresponding to the energy of fundamental state plus the energy of the incident photon) and falls back to the a vibrational excited state, emitting a photon of lower energy (lower frequency $\omega_R = \omega_0 - \omega_{vib}$, hence longer wavelength) than the incident photon, and in the second case, some vibrational state already excited is promoted by the incident photon to a virtual state at an energy corresponding to its initial energy plus the energy of the incident photon before falling back to the fundamental energy level (hence in a lower energy state as the initial state) emitting a photon of higher energy (higher frequency $\varpi_R = \omega_0 + \omega_{vib}$, hence shorter wavelength) than the incident photon. It must be noted, though, that the vast majority of the incident photons excite fundamental states to virtual states and fall back directly to the fundamental state, emitting photon at the exact same frequency at that of the incident photon (elastic scattering = Rayleigh scattering). Raman scattering is therefore occurring only with a few percent of the incident photons (~1 photon out of 1000), and consequently, the Rayleigh is much more intense that the Stokes line, itself more intense than the Anti-Stokes lines (since the latter had to start form an already less populated excited state). The challenge is to detect the Stokes and Anti-Stokes Raman lines only, and not the more intense – but relatively close in energy – Rayleigh line. Raman spectra are actually plots versus wavenumbers (in units of cm^{-1}) of the Raman shift, i.e. the frequency difference between the Stokes (or Anti-Stokes) line and the frequency of the Rayleigh line. Since the vibrational spectra of a substance is material-specific and unique, Raman spectroscopy is therefore used for material analysis, both quantitatively and qualitatively [107]. In the quantitative analysis, the scattered light's intensity is measured in order to determine the analyte concentration in the sample, while in the qualitative analysis, the material is identified using the frequency of the scattered light and the resulting spectrum [108, 109]. Let's first look at the main components of this analytical tool before addressing the science underlying the Raman effect. As shown in Fig. 3-3, the main elements of a typical Raman setup include a highly monochromatic

excitation source, a sample irradiation and collection system, a spectrometer, and a detector typically charge-coupled device (CCD). To provide enough intensity of the scattered light after the interaction (which has a rather low intensity compared to the intensity of the Rayleigh line, as explained above), lasers are technically used as an illumination source. This is due to the fact that the lasers are the source of high intensity monochromatic light. After the laser light has excited the material illuminated, the radiation that has been emitted from the area that has been illuminated is collected and, using a lens, is sent to the spectrophotometer (usually placed perpendicularly to the incident laser beam, in order to avoid detecting the incident and transmitted light beam and to collect only the scattered light). A notch (band-stop) filter is employed to remove the dominating Rayleigh light before reaching the detecting spectrophotometer while leaving the frequency of the Raman scattered light (Stokes or Anti-Stokes) unattenuated. The intensity of the Raman scattered light (Stokes) varies as the inverse of the fourth power of its wavelength [110]:

$$I_S \propto I_0(\omega_0 - \omega_R)^4[\left(\frac{\partial\alpha}{\partial k}\right)_{k=0}]^2 \Rightarrow I_S \propto \lambda^{-4} \qquad (3\text{-}2)$$

The Raman-scattered light is then directed onto a detector, typically a CCD detector using a grating to spatially spread and separate the various wavelengths of the scattered light [107, 111, 112]. The converted optical-to-charge signals provided by the CCD detector can be integrated over a chosen time interval before being transferred to a readout device. In this investigation, a Horiba iHR320 imaging spectrometer with a thermoelectrically cooled Horiba Scientific Synapse Back-Illuminated Deep Depletion CCD detector was used for all Raman experiments. A 473 nm solid state blue Cobolt 04-01 laser (linearly polarized, TEM00) serves as the excitation source.

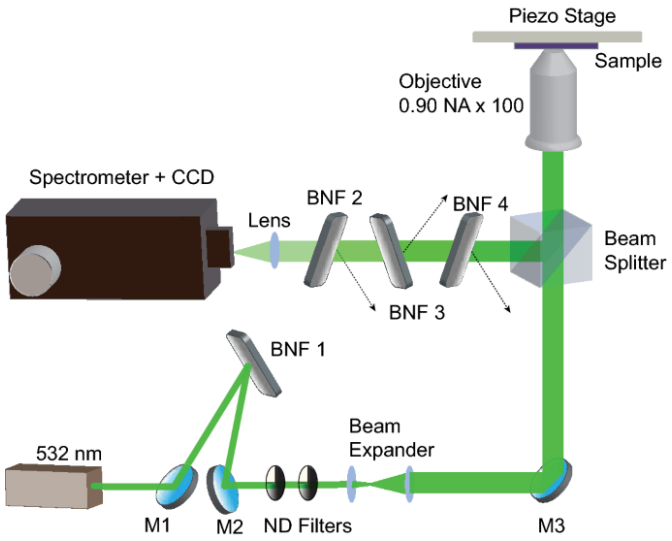

Fig. 3-3 Schematic of a typical system indicating the major components of the Raman spectroscopy setup used.

When a material is irradiated with light that has significant energy, the atoms typically get polarised by the electric field of the electromagnetic radiation, inducing an electric dipole in the molecules. This induced electric dipole moment, also known as induced polarisation, is proportional to the electric field amplitude: $P = \alpha E$, where α is the polarizability of the material, which changes and follows the atoms vibration frequency. If k is the wave vector of the atom vibration in the lattice, $k = k_0 cos(\omega_{vib} t)$, then the polarizability can be expressed by the Taylor series expansion:

$$\alpha(\mathrm{k}) = \alpha_0 + \sum \left(\frac{\partial \alpha}{\partial k}\right)_{k=0} k \; + \frac{1}{2} \sum \left(\frac{\partial^2 \alpha}{\partial k^2}\right)_{k=0} k^2 + \ldots \qquad (3\text{-}3)$$

Then the electric polarization can be written as follow:

$$P = \left[\alpha_0 + \sum \left(\frac{\partial \alpha}{\partial k}\right)_{k=0} k \; + \frac{1}{2} \sum \left(\frac{\partial^2 \alpha}{\partial k^2}\right)_{k=0} k^2 + \ldots . \right] \times E_0 cos(\omega_0 t) \qquad (3\text{-}4)$$

considering the fact that they are anharmonic, the third and the other higher terms of this function are negligible compared to the 2 first terms. Using the trigonometric equality: 2 cos(α) cos(β) = cos(α +β) + cos(α -β), (3-4) can be simplified to the following form:

$$\begin{aligned} P = [\alpha_0 E_0 \cos(\omega_0 t) + \frac{1}{2} \sum \left(\frac{\partial \alpha}{\partial k}\right)_{k=0} k_0 E_0 \cos(\omega_0 t - \omega_{vib} t) \\ + \frac{1}{2} \sum \left(\frac{\partial \alpha}{\partial k}\right)_{k=0} k_0 E_0 cos(\omega_0 t + \omega_{vib} t)] \end{aligned} \qquad (3\text{-}5)$$

Rayleigh, Stokes, and Anti-Stokes scattering are represented by the first, second, and third terms in equation (3-5), respectively. ω_{vib}stands for the scattered phonon frequency. In Fig. 3-4, the Raman processes schematically showing the energy of the inelastically scattered photon smaller (Stokes) and larger (Anti-Stokes) than the excitation photon are detailed.

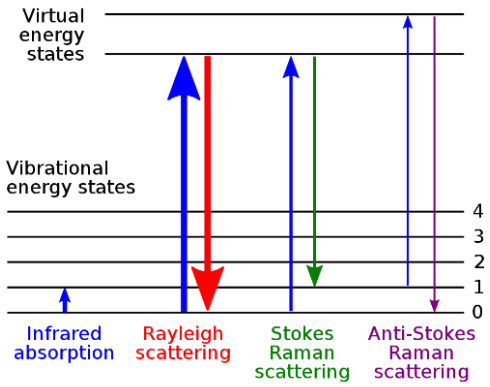

Fig. 3-4 Energy-level diagram showing the photon energies and the states involved in Raman spectroscopy.

When the lattice vibration modes are optical phonons, the inelastic scattering processes are called Raman scattering and the technique Raman spectroscopy. When the lattice vibration modes are acoustic phonons, the inelastic scattering processes are called Brillouin scattering and the corresponding technique Brillouin spectroscopy. Brillouin and Raman scattering have different selection rules predicting the presence or absence of scattering depending on the energy states occupation numbers and crystal symmetry.

Acoustic phonons- This type of phonon modes carry the small amount of energy of $\frac{k_B T}{n(\omega)}$ which goes to zero when $k \to 0$. In this situation, the next neighbour atoms' vibrations are in-phase (Fig. 3-5 (a)). If the atomic displacement is in the direction of or perpendicular to its propagation direction (represented by the wave vector k), the vibration mode is called longitudinal acoustic (LA) or transverse acoustic (TA).

Optical phonons – with the out of phase vibration of the next neighbour atoms, this phonon modes carry a substantial energy which does not goes to zero when $k \to 0$ (Fig. 3-5 (b)). The atomic displacement can be longitudinal or transverse and if it is in the direction or perpendicular to the propagation direction k, the modes are denoted longitudinal optic (LO) or transverse optic (TO), respectively.

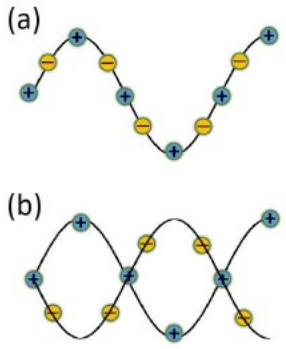

Fig. 3-5 Distinction between (a) acoustic, and (b) optical phonon modes.

3-5-3 Transmission electron microscopy (TEM)

An intense electron beam is used in TEM, which is a combination of imaging and electron diffraction techniques, to offer details on the probe material's structure (TEM images), symmetry and various scale periodicity (selected area electron diffraction), also giving information about dislocations, grain boundaries, etc. Contrary to an optical microscope, which has a fixed wavelength in the $\lambda_{visible}$ = 400 – 800 nm range, an electron beam energy (hence wavelength) can be modified by changing the accelerating voltage. Moreover, its wavelength $\lambda_{electron}$ ~ 0.004 nm for V_a = 100 kV—is far less than the average separation between two atomic planes. This short wavelength's makes it possible to examine a material's structural characteristics at the atomic level with excellent spatial resolution. The components of a conventional TEM are the electron gun (a heated cathode that generates energetic electron streams), the beam conditioning or illuminating system (a series of electromagnetic lenses), and the imaging system (another series of electromagnetic lenses) (see Fig. 3-6). A series of lenses placed in the illumination system compartment direct the thermoionically emitted electrons. The thermoionic electron current emitted from the hot cathode toward the sample to be investigated is related to its temperature by the Richardson law [113]. The portion of the beam is transmitted and is focused on the objective lens depending on the thickness and electron transparency of the material. Finally, the scattered beam is deflected by the electromagnetic field to produce a 2-D image that may be focused on the screen. All the electrons beam, and the sample are located in a very high vacuum. TEM''s ability to also produce an electron diffraction pattern, also known as selected area electron diffraction (SAED) which links the structure periodic characteristics of the image to the

irradiated specified area is one of its benefits. In this work, TEM was utilized to examine the particle sizes and shapes of the powdered materials bright-field images were taken with a JEOL transmission microscope Model JEM-2100F operating at 200 kV.

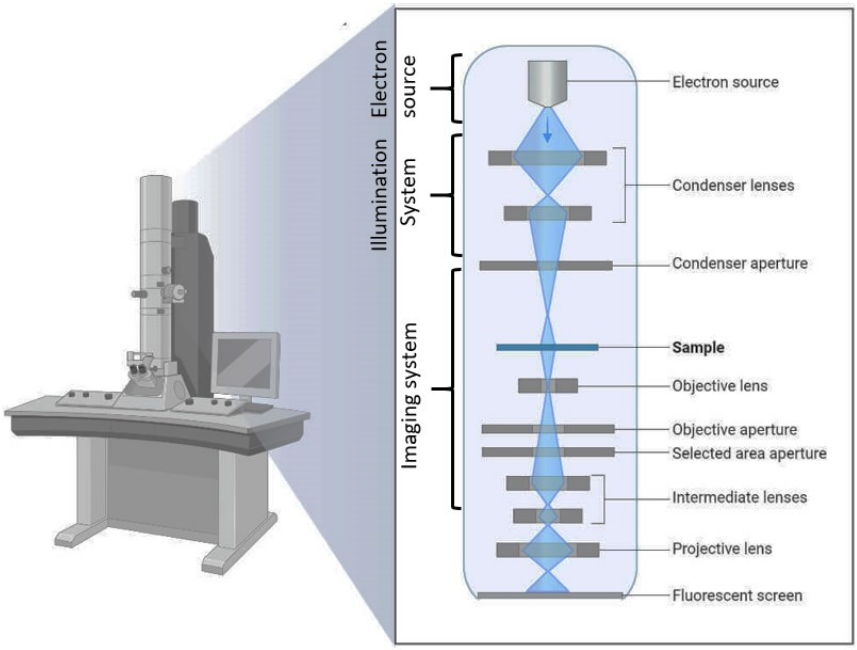

Fig. 3-6 the main components of a TEM system

3-6 Methyl orange catalytic degradation reaction measurements

3-6-1 Piezo-sonocatalysis setup

An ultrasound wave has an ultrasonic frequency higher than 20 KHz. It travels far in water, has a great penetrating power, and has good directionality. It can be used to measure speed, distance, and for other purposes including sterilization and disinfection. There are numerous uses in the fields of agriculture, industry, and medical applications (the best-known being ultrasound imaging). Ultrasound gets its name because its lower frequency limit is roughly comparable to the top limit of human hearing. In this work, the ultrasonic bath model Branson CPHX 1800 has been used for the piezo-sonocatalysis experiments. The frequency and the power of this system were set to 40 kHz and 80 W, respectively. The sound wave pressure produced by ultrasonic vibration in a liquid has a typical power density of around 0.35 W/cm^2 at the atmospheric pressure. The pressure in the liquid on the path of the ultrasound wave oscillates between its

maximum and minimum peak values. The maximum pressure could be locally quite high and the lower pressure might be lower than the evaporation pressure of the liquid at the liquid temperature, in which case the phase transition from liquid to gaseous occurs and a gas bubble forms inside the liquid, a phenomenon called cavitation. When the local ultrasonic pressure reverses and reaches its maximum, the gaseous bubble brutally collapses. The term "cavitation" refers to the shock waves and very energetic liquid microjets produced when numerous microscopic cavitation bubbles implode. These bubble implosions-generated shock waves and energetic liquid microjets impact any surface in the vicinity and , for instance, forces the dirt off the surface.

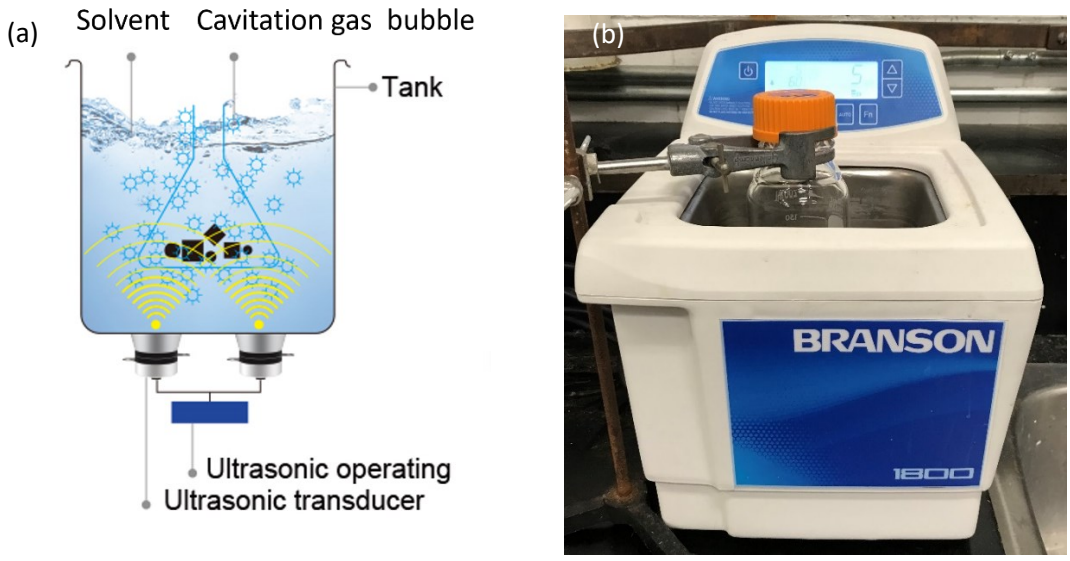

Fig. 3-7 (a) the schematic of the typical ultrasonic systems, (b) photograph of the ultrasonic bath utilized for the catalysis application in this project.

Two different contaminants were used during this project: methyl orange (MO) and Rhodamine B (RhB). During the measurements, we used fixed values of the contaminants' concentration dissolved in water. Catalytic activity measurements were carried out by evaluating the discoloration rate of methyl orange or Rhodamine B solutions via optical absorption measurements. $BaTiO_3$ (piezoelectric) and TiO_2 (non-piezoelectric) nanoparticles 100 nm in size were used as catalyst agents. The MO (or RhB) was dissolved in DI water with a concentration of 4 mg/L and, in the study, these dyes were used as the water pollutant to be degraded. The $BaTiO_3$ and the TiO_2 powders were added separately to the water 'contaminated' with varied dye concentrations from 0 to 1 g/L in order to mimic water contamination by organic pollutants. If

not otherwise stated, the concentration of the catalyst is assumed to be 1 g/L. Due to the specific design of the ultrasonic bath shown in Fig. 3-7(a), the intensity of the ultrasonic waves as well as the number of cavitation bubble is located more in the center of the bath. Accordingly, all the vials containing the dye-contaminated water were always set in the center of the bath and fixed in the liquid without any contact with the bottom of the bath floor. It has also to be noted that all the ultrasonication experiments were done in the dark to avoid photocatalysis. The temperature of the ultrasonic bath was controlled precisely using a submersible heating element (George Ulanet 335-115 Heat-O-Matic Immersion Heater). For the room temperature measurements, the temperature of the liquid bath increased slightly by the time. In order to prevent a temperature variation in our measurements, the water of the ultrasonic bath a replaced continuously by the fresh and cold water. A small quantity of 4 mL of the suspension was taken from the main liquid batch every 30 minutes. This 4mL sample was then centrifuged at 6000 rpm for 10 min, to precipitate the catalyst particles and finally, optical absorption measurements were performed on the supernatant solution. The centrifugation method was selected by comparing the transmittance of water before and after the nanoparticle dispersion. Specifically, the time and frequency of the centrifugation were chosen to ensure that no particles were dispersed in the water after centrifugation. The selected parameters represent the minimum values necessary for effective particle precipitation.

The piezocatalytic degradation of dyes is often measured with dilute aqueous solutions in the presence of a sufficient amount of piezocatalytic materials to be able to degrade all the contaminants. Usually, the end products of such reactions are CO_2 and water. Such a chemical reaction can be classified as a first order or pseudo-first order, and the degradation rate is directly proportional to the initial concentration of the pollutant as follow:

$$rate = -\frac{d[C]}{dt} = k[C]^n \qquad (3\text{-}6)$$

In equation (3-6), k is the rate constant, $[C]$ is the reactant concentration, and n is the order of the reaction rate (i.e. $n = 1$ for first order reactions). Assuming a first order of the reaction, and integrating over time, we get:

$$ln[C] = -kt + ln[C_0] \qquad (3\text{-}7)$$

In which C_0, and C are the initial concentration, and the concentrations at time t. This equation can be rewritten as follow:

$$-ln\left(\frac{C}{C_0}\right) = kt \qquad (3\text{-}8)$$

This form of the expression often used to describe the kinetics of heterogeneous catalytic systems corresponds to the Langmuir-Hinshelwood mechanism under the assumption of a diluted dye and reaction-limited (and not an adsorption/desorption-limited) process. The Langmuir-Hinshelwood expression has been widely used to determine the degradation rate of various pollutants in piezo or photocatalytic reactions. The first order reaction equation (3-8) only applies, though, if the following assumptions are made: (1) The pollutant's initial (molar) concentration is sufficiently low, (2) The reaction's equilibrium point is unaffected by the (by)products, (3) The heterogeneous catalyst is present in considerable amounts, and (4) the number of active catalytic sites has not significantly decreased during the reaction [114]. For the majority of dyes diluted in aqueous solutions, equation (3-8) is valid and may be used to determine the degradation rate constants.

3-6-2 Photocatalysis setups

One of the earliest and most used methods for the degradation of aqueous dye solutions evaluating the effectiveness of catalysts is photocatalysis. In this work, several photocatalysts including $BaTiO_3$ and TiO_2 nanopowders were evaluated by degrading aqueous solutions of different colors. In particular,100 mg of $BaTiO_3$ particles of different sizes were dispersed in 100 mL of water that was previously contaminated with MO (4 mg/L). Adsorption–desorption equilibrium was reached by magnetic stirring of the solution for 30 min in the dark, before illuminating with a standard and calibrated solar simulator (150 W xenon lamp, Model – #SS50AAA, PET Photoemission Tech., Inc.). The temperature of the reactant was controlled precisely using a submersible heating element (George Ulanet 335-115 Heat-O-Matic Immersion Heater) in a water bath containing the reactant vessel. A photograph of the experimental setup is shown in Fig. 3-8. The reaction rate constant, k was evaluated from the slope of the plot of $\ln(C_0/C_t)$ as a function of t, the irradiation time using equation (3-8), and the degradation efficiency was determined by fitting the time-dependent absorption profile obtained from degradation of the dye solution with a two-phase exponential function.

Fig. 3-8 The image of the photocatalysis setup

3-6-3 UV-Vis spectrophotometry

Spectrophotometry is a technique for measuring the amount of light absorbed by a chemical substance based on the intensity of incoming light that has passed through a sample (see Fig. 3-9) Fig. 3-9 Schematic of a spectrophotometer.. It is an effective and popular quantitative analytic technique in a variety of scientific disciplines, including physics, chemistry, material sciences, and medicine. Based on the wavelength range, the spectrophotometry can be classified into UV-Vis (185 nm - 700 nm) and IR (700 nm -15000 nm) spectrophotometery. The different functional groups that are present in a molecule are often identified using IR spectroscopy, whereas UV-Vis spectroscopy is a far more quantitative method. In this study, the quantity of the organic pollutant dissolved in water were measured using a UV-Vis spectrophotometr (Lambda 750).

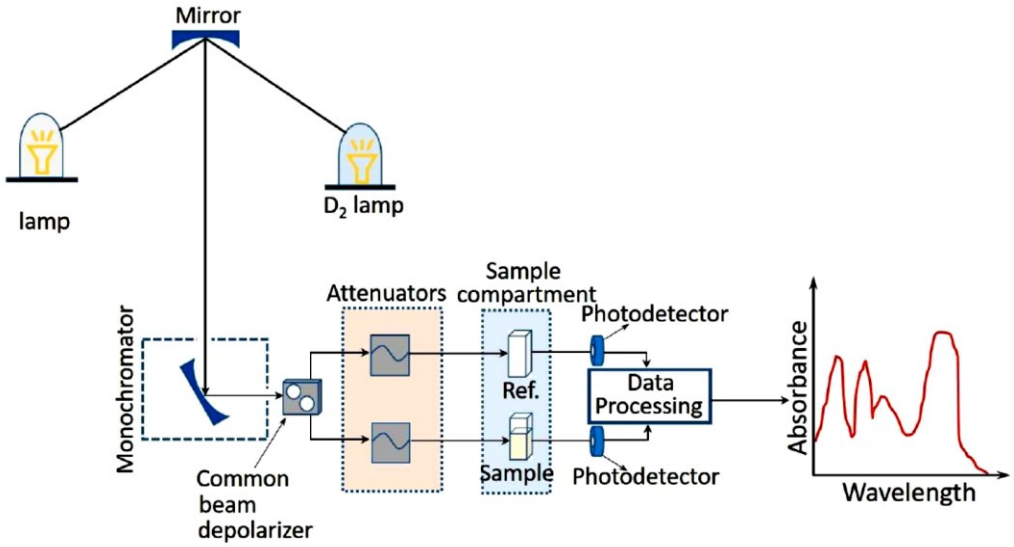

Fig. 3-9 Schematic of a spectrophotometer.

A UV-Vis spectrophotometer calculates the difference between the intensity of incoming light and the intensity of light passing through the suspension (contained in a cuvette). A light source, a empty vial and a vial containing the liquid sample to be measured (cuvette), a dispersive device to separate the various light wavelengths (such as a monochromator), and an appropriate detector are the essential parts of a UV-Vis spectrophotometer. The intensity of light that has passed through the sample solution is measured by the UV-Vis spectrometer's detector. The transmitted intensity, I, is the portion of light that the detector has detected. When light passes through a sample, its intensity is absorbed, and its value is lower than the light's initial intensity I_0 at the light source. Transmittance can be described by the follow equation:

$$T = \frac{I}{I_0} \tag{3-9}$$

The UV-Vis spectrophotometer measures the transmitted light intensity and calculates the transmittance values, but it may also calculate the absorbance values, which are defined as *unitless* values and are mathematically expressed as the negative of the logarithm of the transmittance.

$$A = -log\,(T) \tag{3-10}$$

The change in concentration of a substance may be quickly determined by determining the wavelength that corresponds to the highest absorption and calibrating it against a known solution. This method for quantitative determination is based on the Beer-Lambert law:

$$A = log\left(\frac{I}{I_0}\right) = a_{mol} \times L_{path} \times C \qquad (3\text{-}11)$$

Where the a_{mol}, L_{path}, and C represent the molar absorptivity (extinction coefficient), the length of the sample's path, and the compound's concentration, respectively. A UV-Vis spectrum is often shown as absorbance against wavelength, and the magnitude of the absorption peaks directly corresponds to the amounts of the component to be measured. A solution with a greater concentration will absorb more light, increasing the magnitude of the absorption peak. Additionally, the attenuation is related to the cuvette length, thus a longer cuvette (with its liquid sample) will absorb more light. The UV-Vis spectrum displays variably defined peaks for each pure or broken-down chemical substance. This spectrum allows us to calculate the sample's extinction coefficient, and the rate of the reaction.

In addition to the UV-Vis spectrometer, a simple home-made stage was designed to measure the absorbance of contaminated water in a significantly shorter time. To do this, monochromatic lasers with wavelengths near the absorption peak specific of the model contaminants used (blue laser with wavelength of 405 nm for Methyl Orange, and a green laser with wavelength of 532 nm for Rhodamine B) were chosen and passed through a cuvette containing the contaminated water. The transmitted light was collected by an optical detector (PDA100A 400-1100 nm) that was connected to the computer to record the results. The results obtained by this method were consistent with the results obtained from the standard UV-Vis spectrophotometer.

3-6-4 Liquid chromatography mass spectroscopy (LC-MS)

This technique is used to separate, identify, and quantify the different chemical components of a sample according to a mass spectrometry process involving differential migration of the different components is to be analyzed through a porous separation column, resulting from their differential adsorption on the material composing the column. The pressurized liquid, the sample mixture, and the super-hydrophobic column through which the liquid passes are three main components of an LC-MS system. The liquid passes through a solid absorbance column under pressure, and the chemicals are separated according to their interaction with the column. The

liquid (which is under pressure) typically contains solvents such as water, acetonitrile, or methanol and which are called the mobile phases. The composition of the solvent and its temperature plays an important role in the interactions of the liquid with the column, which are mostly types of physical contacts, such as the hydrophobic, dipole-dipole and ionic (the column is called the stationary phase). The velocity of each chemical component depends on its chemical nature, its interactions with the stationary phase and on the composition of the solvent used (mobile phase). The affinity (Van der Waals force, for example) between the components to be identified and quantified and the mobile phase in the column determines how quickly the component and mobile phase travel across the column. On the other hand, the affinity between the stationary phase and the mobile phase results in slowing down the motion of that component (dissolved in the solvent), leading the stationary column to separate the various chemical compounds (principle of chromatography). The retention time which is the time at which a specific analyte passes through the column permits to identify the a given analyte. Fig. 3-10 schematically shows different part of an LC-MS mass spectroscopy.

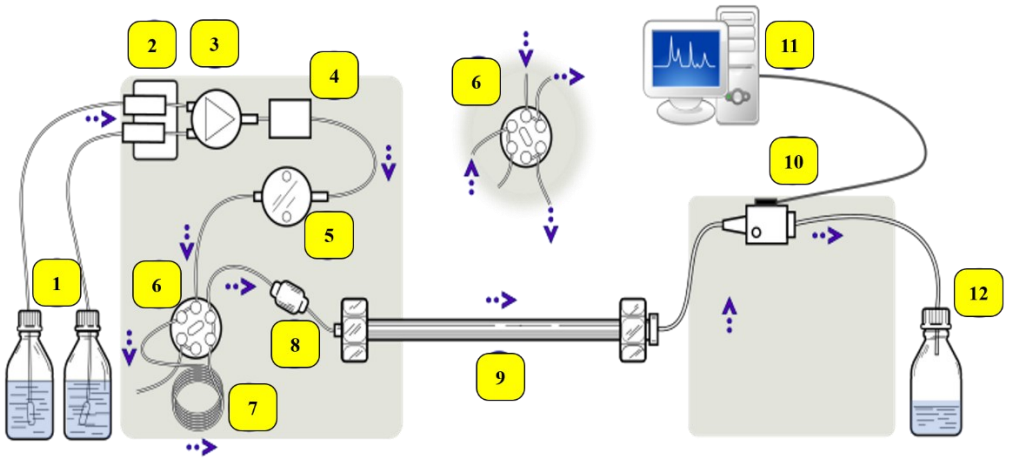

Fig. 3-10 A unit of LC-MS; schematic view; (1) Solvent reservoirs, (2) Solvent degasser, (3) Gradient valve, (4) Mixing vessel for delivery of the mobile phase, (5) High-pressure pump, (6) Switching valve in "inject position", (6') Switching valve in "load position", (7) Sample injection loop, (8) Pre-column (guard column), (9) Analytical column, (10) Detector (i.e., IR, UV), (11) Data acquisition, (12) Waste or fraction collector.

Chapter 4

Results and Discussion

4-1 Introduction

In this chapter, the experimental results obtained during this project are presented and discussed in detail. The main goal of this chapter is to present a discussion of the results of our research leading to achieving our objective, namely, to determine the contribution of the piezoelectric properties to the piezo-sonocatalysis process. In the first section, the sono-piezocatalytic activities of piezoelectric tetragonal $BaTiO_3$ and non-piezoelectric anatase TiO_2 powders are presented, discussed, and compared, the differences between these two materials with similar surfaces but one being piezoelectric and the other not, constitutes a first step toward our goal. As discussed in the second chapter, the size and temperature are the two important factors that control the $BaTiO_3$ structure and determines whether it is in its tetragonal piezoelectric phase or in its cubic paraelectric phase. In the last part of this chapter, the experimental results describing the effect of the temperature and the size effects of the $BaTiO_3$ nanoparticles on their

piezopotential, and thus on their piezocatalytic activity, are presented and discussed in detail. Finally, some conclusions are drawn concerning the relative contribution of sonocalaysis and piezocatylysis when piezoelectric $BaTiO_3$ nanoparticles are used as catalysts.

4-2 Catalytic Activities of $BaTiO_3$ and TiO_2

Recent piezocatalysis research efforts seem to have overlooked the omnipresent contributions of a sono- and tribocatalytic processes. When evaluating the catalytic activity of the piezoelectric nanoparticles employed as catalysts, piezocatalysis, sonocatalysis, and even tribocatalysis should occur concurrently. To distinguish between tribocatalysis, sonocatalysis, and piezocatalysis in the catalytic process of methyl orange (MO) degradation by ultrasonication in aqueous solution, and to quantify the real piezoelectric contribution to the catalytic activity of the $BaTiO_3$ nanoparticles, we investigate the specifics of the catalytic activities of TiO_2 (non-piezoelectric material) and $BaTiO_3$ (classic piezoelectric material) with the same particle sizes (100 nm) and the same tetragonal crystal structures (it should be noted here that the anatase phase of TiO_2 is a type of tetragonal structure).

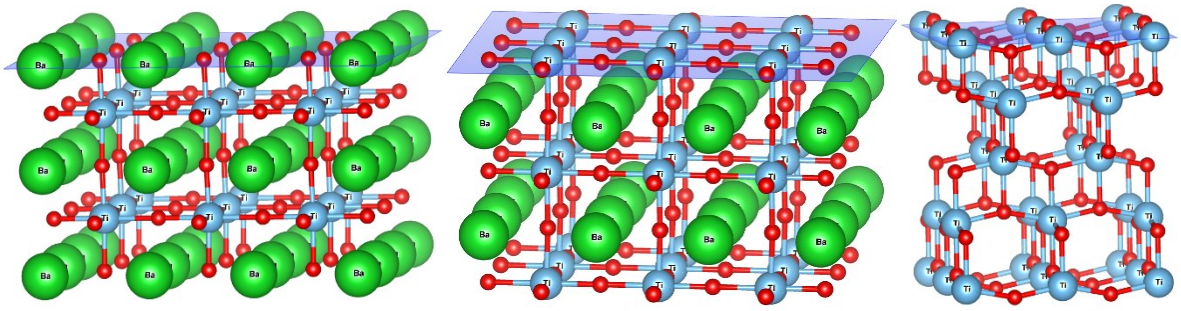

(a) (b) (c)

Fig. 4-1 Schematic of the tetragonal $BaTiO_3$ external surface when (a) Barium and oxygen, (b) Titanium and oxygen constitute the last atomic layer of the surface, and (c) the anatase TiO_2 crystal structure, which has the same termination surface a the $BaTiO_3$ when terminated by Ti and O, as shown in (b).

$BaTiO_3$ can structurally be seen as alternated BaO and TiO_2 sub-lattices, and that the surfaces of $BaTiO_3$ are either BaO- or TiO_2-terminated. Fig. 4-1 (a) and (b) shows the two possible externals surfaces of the $BaTiO_3$, in which the latter is comparable with the termination surface of the anatase TiO_2 structure shown in Fig. 4-1 (c). Since the BaO surfaces exhibits little or no catalytic

activity (it is catalytically inactive due to the fact that the surface of BaO easily react with the environmental contaminations such as CO_2 yielding $BaCO_3$, which is totally inactive for such catalytic reactions) [1], TiO_2 could therefore be considered the non-piezoelectric material with a catalytic activity the closest to piezoelectric $BaTiO_3$. Moreover, since both materials have a similar optical bandgap of around 3.2 eV [2], comparable optical properties are expected for these two materials. It is thus anticipated that they might have comparable photocatalytic and sonocatalytic activities, the only significant difference being that one is piezoelectric and the other not. We assume that half of the free surface of $BaTiO_3$ is terminated with barium and oxygen, while the rest of the surface is terminated with the titanium and oxygen. With these assumptions, the contribution of the piezoelectric properties of $BaTiO_3$ to the catalytic activities of $BaTiO_3$ is therefore determined by comparing the catalytic activity of piezoelectric $BaTiO_3$ nanoparticles as catalyst with that of non-piezoelectric TiO_2 nanoparticles as catalyst, both in aqueous solution and submitted to ultrasonic vibrations. It needs however to be point out that barium titanate vicinal surfaces with TiO_2 termination are neither structurally nor electronically absolutely identical to the surfaces of anatase or rutile TiO_2.

Methyl orange (MO), an organic dye, has been chosen as model pollutant in this study. It has been reported that $BaTiO_3$ nanoparticles are positively charged in near-neutral pH environment [3]. Thus, it is expected that anionic MO should be easily adsorbed by the $BaTiO_3$ nanoparticles. However, for completeness, the efficacy of the piezocatalysis of $BaTiO_3$ NPs was also examined with a cationic dye, namely Rhodamine B (RhB).

4-2-1 X-ray diffraction

Fig. 4-2 (a) shows the $BaTiO_3$ and TiO_2 nanoparticles' measured x-ray diffraction spectra at room temperature. The $BaTiO_3$ XRD pattern was indexed using the JCPDS card: 03-0725 to tetragonal $BaTiO_3$ with space group P4mm. In these nanoparticles, the unit cell's tetragonal distortion is remarkably small, yet can still be seen by the deconvolution of the diffraction peak at $2\Theta = 45^{o}$ into the two (200) and (002) peaks, as shown in Fig. 4-2 (b). It can be inferred from this pattern that [(c/a)-1= 0.008]. In other words, given that the tetragonal phase of $BaTiO_3$ is polar and exhibit a spontaneous polarization at room temperature, the splitting of the peak proves that its crystal structure is tetragonal and that this crystalline phase is ferroelectric and hence also piezoelectric. Since the tetragonality of $BaTiO_3$ (c/a) decreases [115, 116] as a function of

decreasing particle size, it is thus consistent and expected that the $BaTiO_3$ nanoparticles exhibit a small distortion of the unit cell. The measured diffraction pattern of the non-piezoelectric TiO_2 nanoparticles matches quite well the anatase phase of TiO_2 (JCPDS card: 21-1272), as shown in Fig. 4-2 (a).

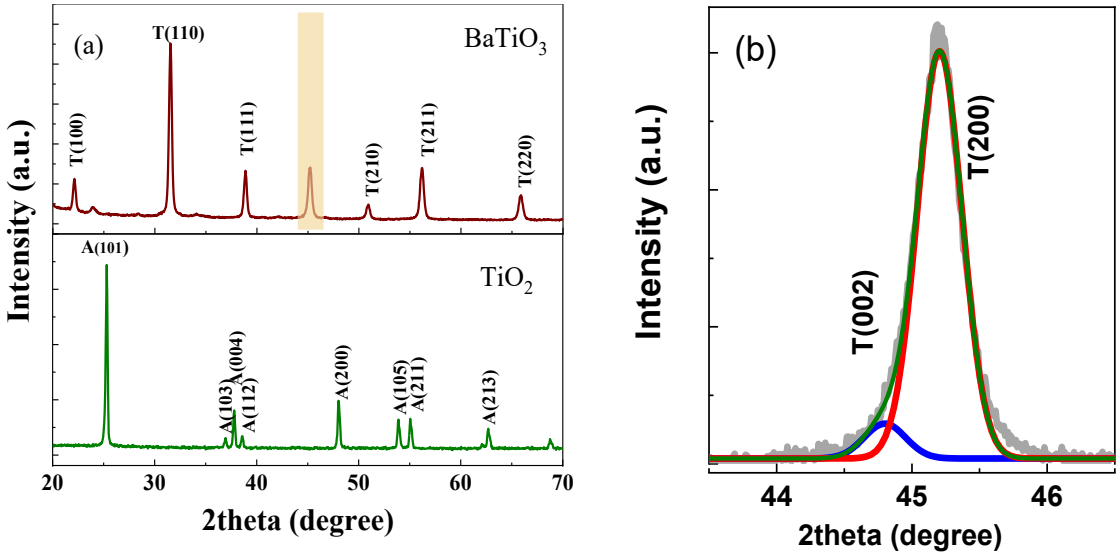

Fig. 4-2 Experimental X-ray diffraction patterns of (a) $BaTiO_3$ and TiO_2 nanopowders, both having tetragonal symmetry. (b) the high-resolution X-ray peak pattern of the $BaTiO_3$ peak located at $2\Theta = 45^o$.

4-2-2 Raman Spectroscopy

In addition, the samples were examined using Raman spectroscopy to determine their level of tetragonality and crystallinity. The Raman spectra of $BaTiO_3$ and TiO_2 nanoparticles, respectively, are shown in Fig. 4-3 (a) and (b). It is well-stablished that an ideal cubic phase of $BaTiO_3$ is Raman-inactive due to isotropic and hence centrosymmetric distribution of electrostatic forces in the unit cell [117]. In some cases, however, Raman activity of the cubic phase has been reported with the persistence of the Raman modes at 262 cm^{-1} and 520 cm^{-1}, generally attributed to disorder of the Ti^{4+} cation in the nominally cubic phase [118]. From the acquired Raman spectra of $BaTiO_3$, it can be seen that the observed phonon modes (i.e. 180 cm^{-1}, 262 cm^{-1}, 302 cm^{-1}, 520 cm^{-1}, and 715 cm^{-1}) are consistent with the Raman spectrum of the $BaTiO_3$ tetragonal phase [119]. The Raman mode at ~183 cm^{-1} is assigned to $A_1(TO)$ and confirms the nanosize of the $BaTiO_3$ powder. The bulk counterpart has been shown to exhibit a spectral dip around this wavenumber, in contrast to the sharp peak observed in the nanosized

particles, which indicates a coupling of A_1 transverse optic mode to E(TO), E(LO), and A_1(LO) [120, 121]. The two characteristic peaks at 302 cm^{-1} [B1, E(TO + LO)] and 706 cm^{-1} [A_1(LO), E(LO)] denote the Ti-O3 torsional and Ti-O stretching vibrations in the TiO_6 octahedra, respectively indicating the tetragonality or off-centering of the Ti^{4+} ion often estimated by 1- c/a. The two Raman modes are strongly affected by temperature and even smear out once the room-temperature tetragonal phase structurally transforms to the high-temperature cubic phase. The Raman mode at 509 cm^{-1} assigned to A_1(TO) indicates another transverse optic mode associated with Ti-O stretching vibration in the TiO_6 octahedra. The Raman spectrum of TiO_2 depicted in Fig. 4-3 (b) shows typical features of the anatase phase with the presence of five modes: 138, 192, 387, 504, 625 cm^{-1} which are assigned to E_g, E_g, B_{1g}, A_{1g}, and E_g vibration modes, respectively [122].

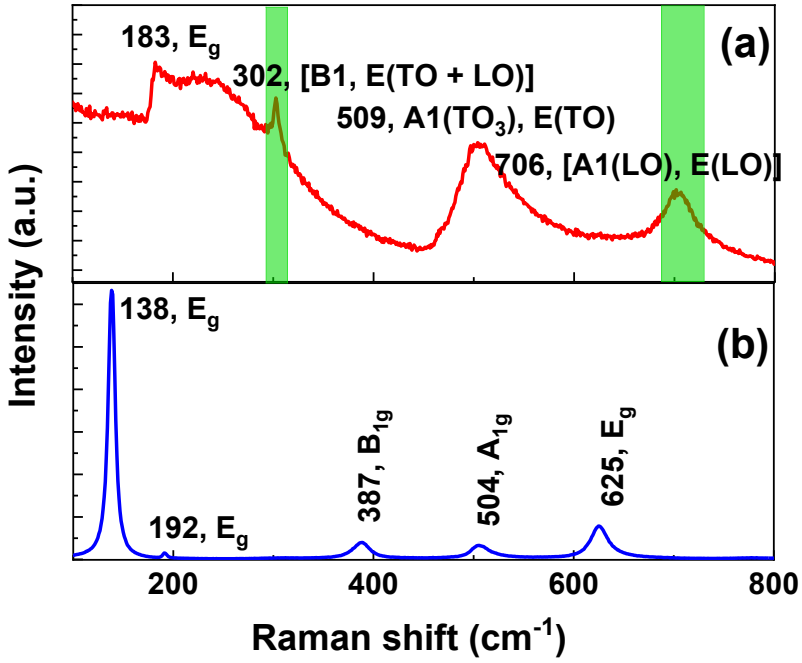

Fig. 4-3 Room temperature Raman spectra of (a) $BaTiO_3$, and (b) TiO_2 nanoparticles. The Raman modes of $BaTiO_3$ detected at 305 and 706 cm^{-1} are associated to the tetragonal phase.

4-2-3 Particles morphology investigated by TEM

The microstructure of the $BaTiO_3$ and TiO_2 nanopowders have been observed using TEM images, as shown in Fig. 4-4 (a) and (b). It is noticeable that both $BaTiO_3$ and TiO_2 nanoparticles have cubic shapes. The presence of parallel facets and cubic habits in both nanopowders suggests

their single-crystalline nature [123]. Also, the agglomeration of the $BaTiO_3$ nanoparticles is clearly seen to be less than that of TiO_2 nanopowder. The size distribution of the powders obtained form the analysis of the TEM micrographs is shown in Fig. 4-4 (c) and (d). The total surface of the catalyst powder in an specific weight of the catalyst powders can be determined by these results. Based on these findings, it can be calculated that the total catalytic surface area of $BaTiO_3$ is approximately 9% larger than that of TiO_2. This suggests that, in terms of surface area, the two catalysts are comparable. The sizes of the nanoparticles in both powders are quite uniform in the range 80-120 nm, so that it can be considered that both powders have also the comparable particle size range and morphologies.

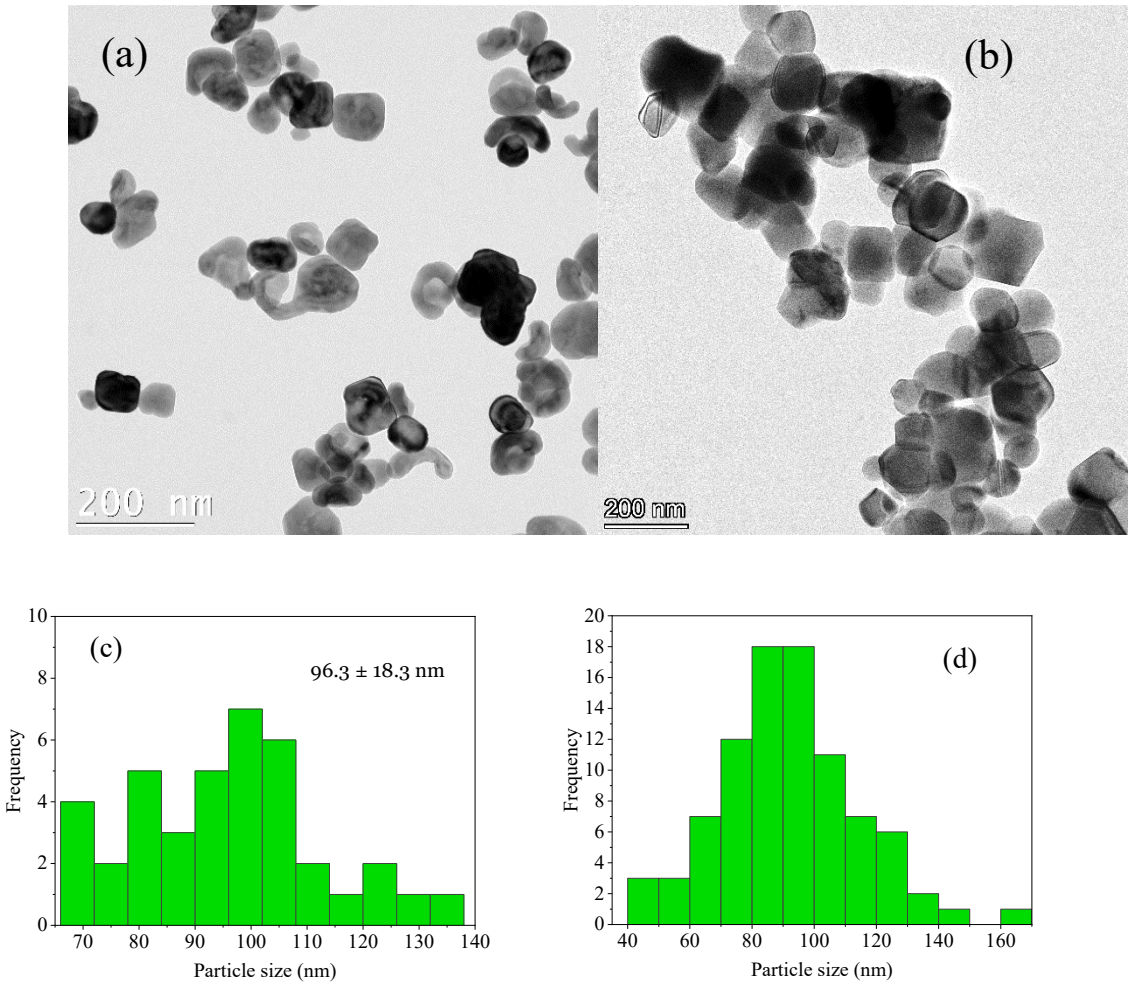

Fig. 4-4 Bright Field TEM image of (a) $BaTiO_3$ and (b) TiO_2 nanopowders, with the size distribution of the (c) $BaTiO_3$ and (c) TiO_2 nanopowders. The measured nanoparticles have a typical size of 80-120 nm.

4-2-4 Catalytic characterizations

The catalytic activities of $BaTiO_3$ and TiO_2 nanoparticles were investigated in suspension in water 'contaminated' with MO by submitting the aqueous solutions to continuous ultrasonic vibrations at a frequency of 40 kHz in an ultrasonic bath with a power of 80 W. Fig. 4-5 (a) displays the UV-vis spectrophotometric absorption measurements in the 300–620 nm wavelength range and for several ultrasonication times of the MO-contaminated water with $BaTiO_3$ nanocatalyst suspensions. There is a sharp absorption peak at 464 nm in the contaminated solution before ultrasonication, which is attributed to the MO for the curve. The intensity of this peak clearly decreases with time, so that after 3 hours, this peak has been significantly decreased. The fact that the colour of the contaminated water changed from light orange to transparent

suggests that $BaTiO_3$ nanoparticles are indeed acting as catalysts to breakdown the organic dye soluble in water. This figure also includes curves and images of the cells taken after larger ultrasonication times and show an almost complete disappearance of the peak and an almost transparent solution after 6 hours, which convincingly demonstrate the efficacy of $BaTiO_3$ to degrade MO under ultrasonication. For the MO-contaminated solution with TiO_2 nanocatalysts, the same results along with corresponding cell images of the polluted water taken after various time intervals are displayed in Fig. 4-5 (b). It is clearly seen that the baseline of the absorption curves increases with time. This can be an indication of some by-products formation using the TiO_2 nanoparticles catalysts. Comparing the results of $BaTiO_3$ and TiO_2 reveals that solutions containing $BaTiO_3$ catalysts degrade MO more rapidly and efficiently than those containing TiO_2. To provide a better discussion of the results on the degradation of MO using $BaTiO_3$ and TiO_2 catalyst nanomaterials, the contribution of the baseline has been subtracted. Fig. 4-5 (c) and (d) display the same data without their respective baselines. The corrected graphs reveal a significant finding: when TiO_2 was employed as the catalyst, a substantial amount of MO remained after 6 hours of ultrasonication, whereas almost all contaminants were degraded when $BaTiO_3$ was used as the catalyst. In terms of quantitative analysis, prior to implementing baseline corrections on TiO_2, the graph indicates that approximately 54% of the MO contaminations persist in the water. However, following the baseline corrections, it implies that only about 23% of the MO contaminants remain in the water. Similarly, for $BaTiO_3$, the measurements show a reduction from 11% to 3% after implementing the baseline corrections.

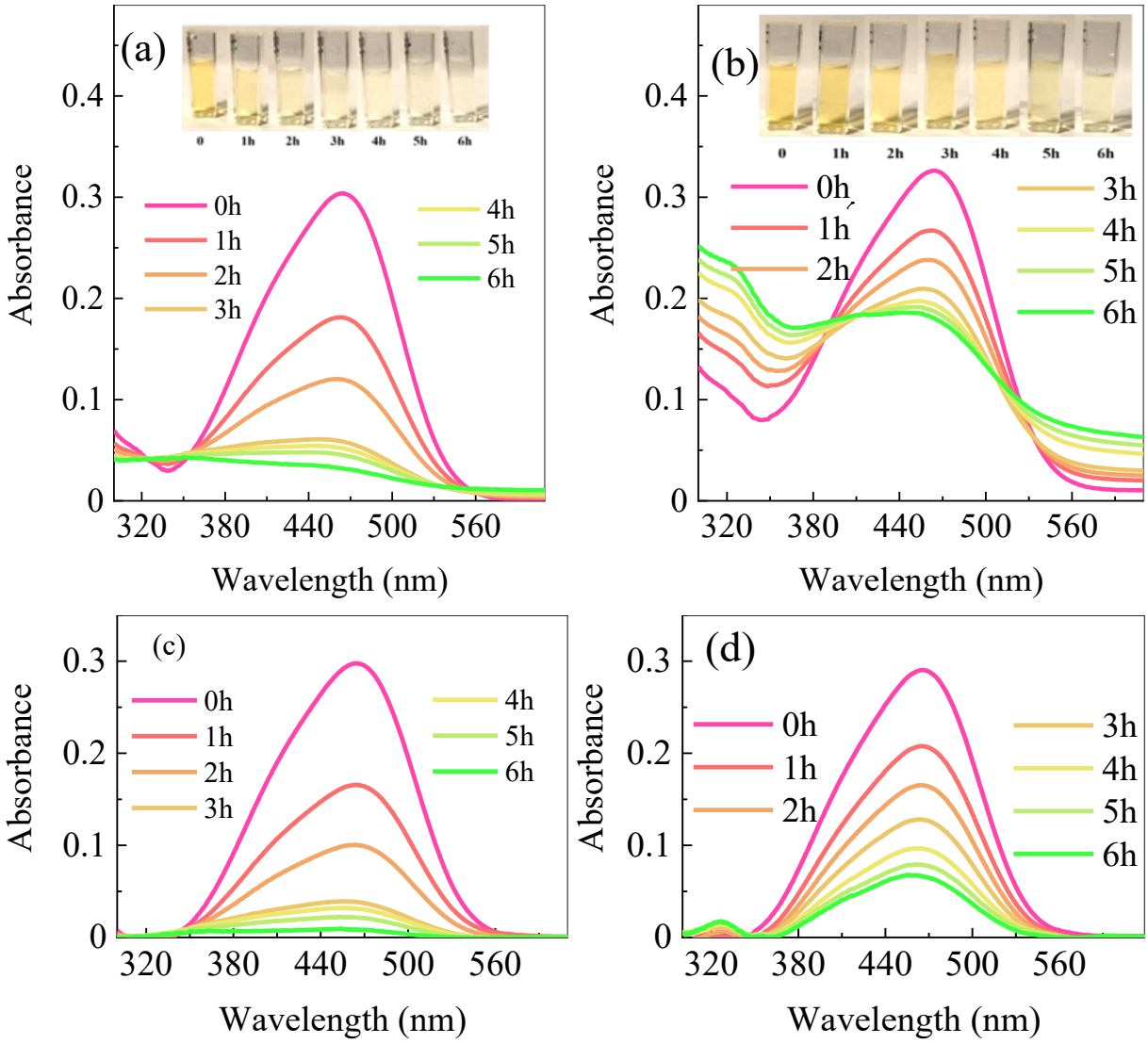

Fig. 4-5 UV–vis spectrophotometry of the contaminated water obtained with (a) $BaTiO_3$ and (b) TiO_2 catalysts at differen times of ultrasonic vibrations before removing the baseline, accompanied by the photographs showing the variation of the MO solutions colors after different times of ultrasonic vibrations. (c) and (d) shows the data corresponding to (a) and (b), respectively, after the baseline of the graphs have been removed.

In order to clarify the dye degradation processes using these two materials as catalysts, a series of additional studies have been carried out. As shown in Fig. 4-6 (a), using ultrasonic vibration without a catalyst in the solution does not result in any significant changes in the concentration of MO. The contaminants are also not appreciably reduced by the simple addition of TiO_2 or $BaTiO_3$ to MO-contaminated water and just mixing them with a magnetic stirrer without any ultrasonic vibration. However, it is seen that organic dyes like MO or RhB degrade and that their

concentration decreases as a function of time when TiO_2 or $BaTiO_3$ nanoparticles are used as catalytic agents under ultrasonic vibration, as shown in Fig. 4-6 (a). The fact that RhB is a cationic dye and MO is an anionic organic dye suggests that similar results are expected for a large range of organic contaminants of all types. By using the same concentrations of catalyst materials (0.5 g/L) for both TiO_2 and $BaTiO_3$ nanoparticles in an MO polluted water (4 mg/L), it has been clearly seen that after 8 hours, TiO_2 NPs degrade 50% of MO pollutant, while more than 80% of MO was degraded with $BaTiO_3$ NPs. These results show that with the same ambient condition, the catalytic efficiency of $BaTiO_3$ nanoparticles to decontaminate the water is clearly larger than that of TiO_2, which we attribute to the piezoelectric properties of $BaTiO_3$ and its piezocatalytic activity. The efficiency of the dye degradation should also depend on the concentration of the catalyst. The effect of the catalytic efficiency as a function of the catalyst concentration was measured as a function of time for different concentrations of $BaTiO_3$ nanopowders. The dye degradation increases significantly as the concentration of $BaTiO_3$ NPs increases from 0 to 0.5 g/L. To quantitatively discuss these changes further, we use the Langmuir-Hinshelwood model to define the reaction rate constant (K_{obs}) of the dye degradation according to the following equation:

$$K_{obs} \times t = -ln\left(\frac{C_t}{C_o}\right) \qquad (4\text{-}1)$$

where C_0 is the initial molar concentration of the dye solution and C_t is the molar concentration of the dye solution at time t. In Fig. 4-6 (b) and (c), the changes of $-ln(C_t/C_0)$ is shown for different concentrations of $BaTiO_3$ and TiO_2, respectively. The slope of the fitted plots gives the reaction rate constants for each concentration. Fig. 4-6 (d) displays the calculated reaction rates of each catalyst at different concentrations. Both results for $BaTiO_3$ and TiO_2 have been simply fitted with linear curves to obtain the dependency of the catalytic reaction rates on the concentration of the nanopowders dispersed in the liquid as catalyst agents. The obtained are 0.53 and 0.22 [L/g×h] for $BaTiO_3$ and TiO_2, respectively. Also, considering that catalytic scales with the concentration of particles, it should be stated that due to their different densities, there is a larger number of TiO_2 than $BaTiO_3$ particles in the solution for a given mass concentration and identical particle size. If corrected for density and expressed per particle or even better - since they have similar sizes - per unit of reacting surface, the curve related to TiO_2 in Fig. 4-6 (d) should be reduced by approximately 40%, which emphasize even more the difference of catalytic

activity between TiO_2 and $BaTiO_3$, hence the importance of the piezocatalytic contribution to the MO degradation.

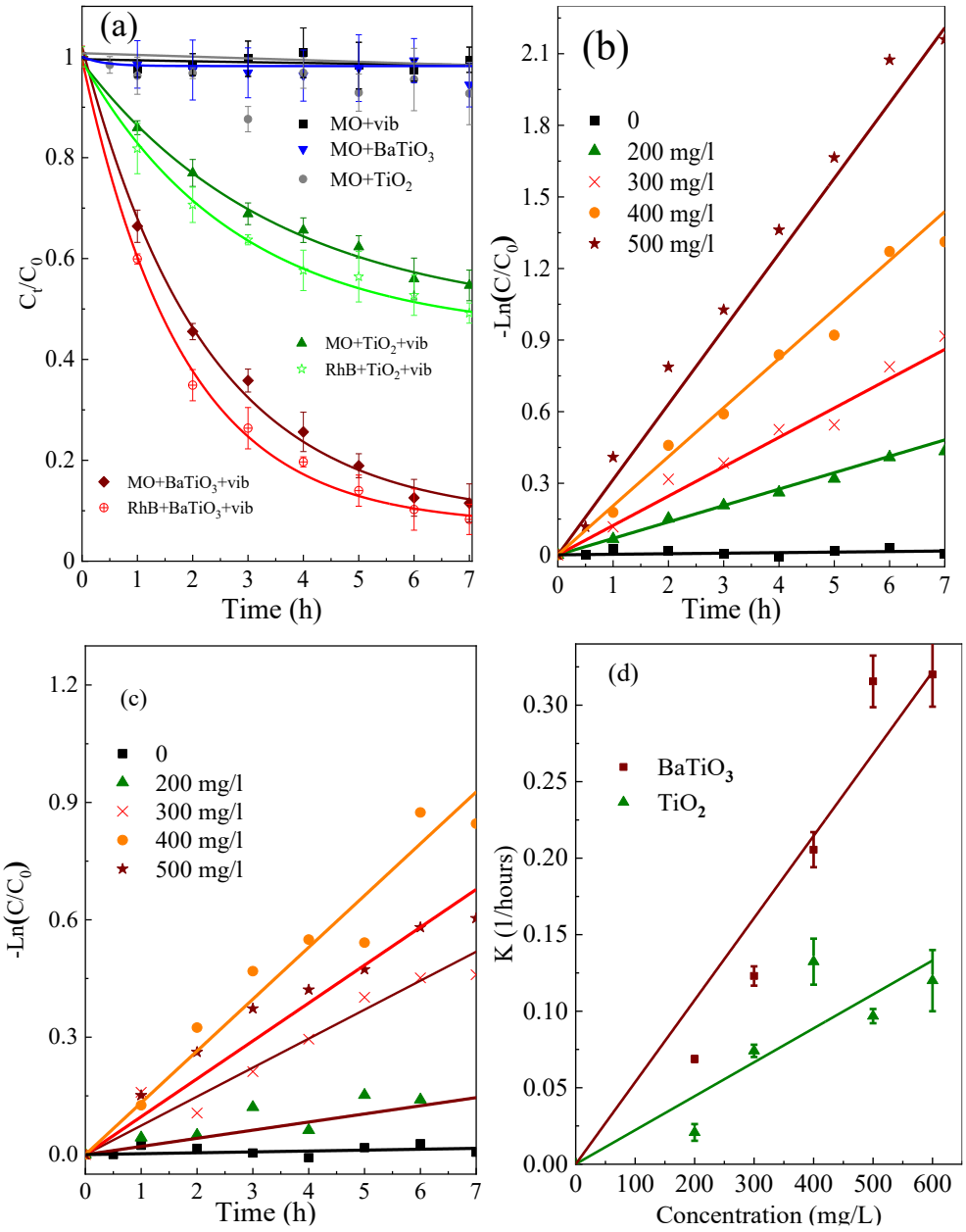

Fig. 4-6 (a) Time-dependent piezocatalytic activities of $BaTiO_3$ and TiO_2 catalyst nanoparticles for the degradation of MO and RhB in solution, and also when the catalysts were stirred with the contaminated water without the presence of ultrasonic wave. Time-dependent piezo-sonocatalytic activities of different concentrations of (b) $BaTiO_3$ and (c) TiO_2 nanopowder; plot of $-\ln(C_0/C_t)$ versus sonication time for different concentrations of catalyst nanopowder. (d) Piezo-sonodegradation kinetics of the methyl orange (MO) calculated by measuring the catalytic reaction rates at different concentrations of $BaTiO_3$ and TiO_2.

The ultrasound-assisted catalytic properties of $BaTiO_3$ and TiO_2 particles were also investigated at different temperatures. The experiments were done at six different temperatures from 25°C to 70°C, and the results are shown in Fig. 4-7 (a) and (b). It is observed that by increasing the temperature, the $BaTiO_3$ catalytic reaction rate decreases, while the temperature promotes the TiO_2 catalytic activities to decompose the inorganic dyes up to 60°C. Such an increase of the catalytic reaction rates of TiO_2 nanopowders with temperature has been previously reported [15]. The significant variation observed in the reaction rates based on temperature strongly suggests that the catalyst activities in $BaTiO_3$ and TiO_2 are governed by distinct physical mechanisms.

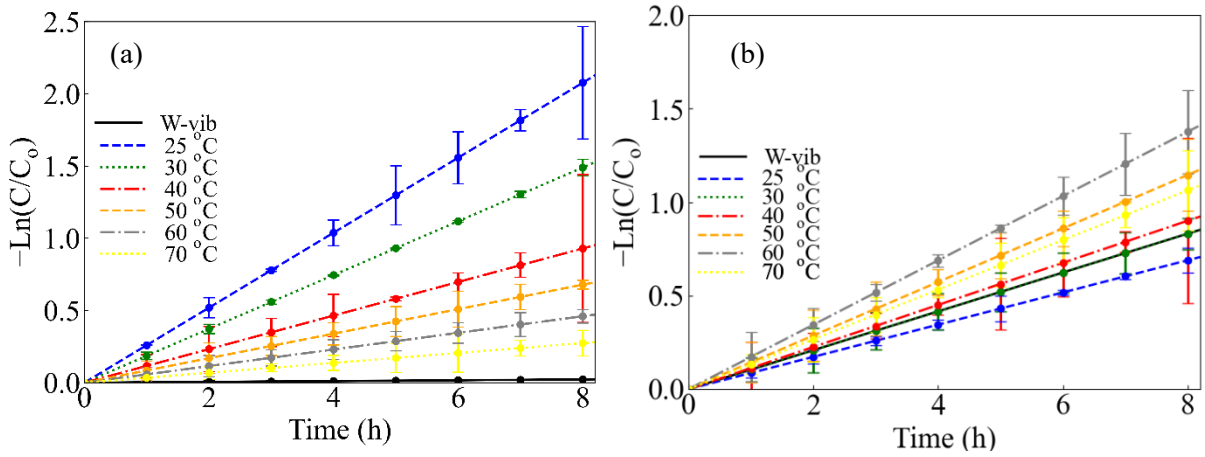

Fig. 4-7 MO dye degradation at different temperatures using (a) $BaTiO_3$, and (b) TiO_2 nanoparticle catalysts with 100 nm size.

In order to investigate the stability – or the possible degradation - of the piezocatalytic activity of $BaTiO_3$ nanoparticles, the same nanopowders (nominal concentration of 0.5 g/L of $BaTiO_3$) were used and re-used several times as catalysts for several catalytic cycles. For the first cycle, 1cc of water contaminated with MO (with a concentration of 0.4 g/L) was added to 99 cc of water containing the $BaTiO_3$ nanopowder catalyst, and then submitted to ultrasonic vibrations for several hours until the solution becomes clear i.e. until a nearly total catalytic degradation of the MO organic pollutant. For the following cycles, after switching off the ultrasonic vibrations and waiting that the $BaTiO_3$ nanoparticles settled at the bottom of the vial containing the solution, 1 cc of the clear solution is removed and replaced by 1 cc of fresh contaminated water, so the MO concentration in the solution is restored to the exact same level it had before the 1st cycle of catalytic degradation started. The restored solution is then submitted to ultrasonic vibration and the second cycle of catalytic reaction proceeds with the same $BaTiO_3$ nanopowder catalyst

(which stayed in the solution settled at the bottom of the vial as long as the ultrasonic bath was switched off) as during the first cycle. The same procedure is repeated for a third and fourth cycle of catalytic reactions. As shown in Fig. 4-8, the efficiency of MO degradation, i.e. the catalyst activity of the $BaTiO_3$ nanoparticles remains quite similar during and after the 4 catalytic cycles. This result is a good indication of the stability of the catalyst nanoparticles in the contaminated liquid. However, it is observed that the final concentration of the pollutant at the end of each 7-hour cycle slowly increases, so that in after the first cycle of catalytic reactions, just 10% of the contaminants is left while a bit more that 20 % of the contaminant is remaining at the end of the fourth cycle. This is an indication of the accumulation of contaminants from the previous cycle and not the performance of the $BaTiO_3$ catalytic activity.

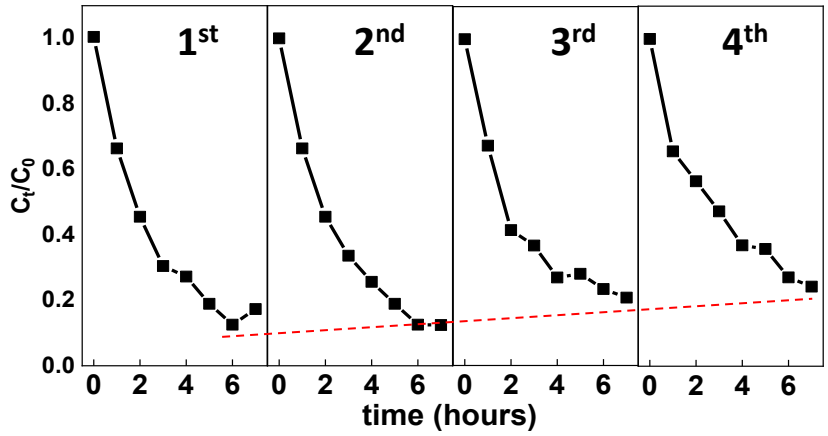

Fig. 4-8 The reproducibility and stability of the catalytic activities of $BaTiO_3$ nanoparticles after 4 cycles. The solid line is a guide to the eye.

4-2-5 Chemical reaction pathways

By conducting some controlled experiments in adding to the contaminated solution system scavenger additives such as tert-butyl alcohol (TBA), benzoquinone (BQ), and ethylenediaminetetraacetate dehydrate (EDTA-2Na) which react specifically with the free radicals $^{\bullet}OH$, $^{\bullet}O_2^-$, and holes, respectively, the details of the piezocatalytic process were investigated. The relative concentration ratio (C/C_0) of MO with 100 nm size $BaTiO_3$ nanopowder was determined in the presence of various scavengers, as shown in Fig. 4-9 (a). For TBA, EDTA, and BQ, the rates of the decrease were determined to be 48%, 94%, and 93%, respectively. These findings suggest that ultrasonication with $BaTiO_3$ catalyst nanoparticles

results in a substantial number of holes (and electrons that later yields the free radicals of $^{\bullet}O_2^-$). In any case, the abundance of holes and electrons yields the generation of $^{\bullet}OH$ and $^{\bullet}O_2^-$ radicals when they react with water molecules and with the oxygen dissolved in water [16]:

$$BaTiO_3 + \text{vibration} \rightarrow BaTiO_3 + (h^+ + e^-) \quad (4\text{-}2)$$

$$O_2 + e^- \rightarrow {}^{\bullet}O_2^- \quad (4\text{-}3)$$

$$H_2O + h^+ \rightarrow {}^{\bullet}OH + H^+ \quad (4\text{-}4)$$

As demonstrated in Fig. 4-9 (b), similar results were also obtained using TiO_2 nanoparticles as catalyst in the presence of these scavengers, demonstrating that both materials have comparable catalytic pathways. In Fig. 4-9 (c), the calculated reaction rates of MO degradation with $BaTiO_3$ and TiO_2 catalysts are compared in the presence of various scavengers

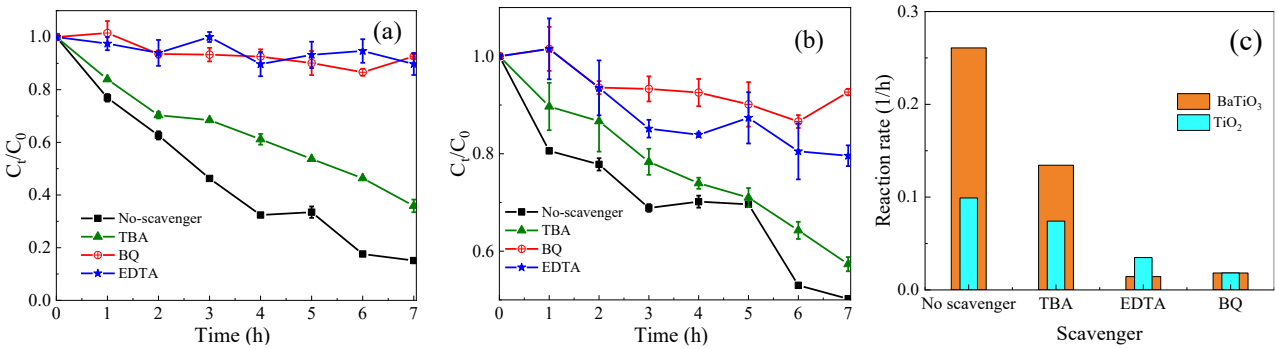

Fig. 4-9 Plots of C/C_0 vs. ultrasonic vibration time in the presence of free radical scavengers for the (a) $BaTiO_3$, and (b) TiO_2 nanocatalysts, and (c) the kinetic reaction rate constant for the degradation of MO obtained in the presence of different scavengers.

The results show that the abundancy of holes plays a critical role in the catalytic reactions. Hydrogen peroxide is known for its excess of protons that can help evolution of the chemical reactions in wastewater treatment process. In order to better understand the chemical reaction pathways when $BaTiO_3$ is used as catalyst, the piezo-sono catalytic reaction experiments were also conducted in the presence of different concentrations of hydrogen peroxides. This experiment can be thought as a kind of reverse of what has been done with the scavengers discussed in the previous section. In this experiment, different concentrations of H_2O_2 were added to the contaminated water, and the piezo-sonocatalysis experiments were done in the same way as before. The results of these experiments are shown in Fig. 4-10 (a). They demonstrate that the chemical reaction's rate with $BaTiO_3$ catalysts slightly increased when the concentration

of H_2O_2 was increased by 2.5%. however, for a further increase of hydrogen peroxide, the reaction rates decrease significantly, so that in the presence of 5 % of hydrogen peroxide the ultrasonic experiment hardly degrade the organic dyes with $BaTiO_3$ NPs catalysts. The reaction rates vs. H_2O_2 concentration are shown in Fig. 4-10 (b). These findings suggest that the degradation of dyes is assisted by the presence of small amounts of protons (H^+). If directly affected by the ultrasonic waves, it is likely that H_2O_2 molecules degrade to hydroxyl agents without the help of catalyst. In other case, with the help of free electrons in conduction bands the following reaction may occur according to the literature [124]:

$$H_2O_2 + e^- \rightarrow .OH + OH^- \qquad (4\text{- }5)$$

The presence of hydroxyls helps evolution of the dye degradation process. However, in the other hand, additional amount of hydroxyls lead to the consumption of superoxide that are critical agents in the completeness of the dyes degradation process. The superoxide may react with the hydrogen peroxide molecules according to the following process [125]:

$$H_2O_2 + O_2^- \rightarrow .OH + OH^- + O_2 \qquad (4\text{-}6)$$

These two reactions show that there is an optimum for the amount of hydrogen peroxide that can be helpful for the dye degradation process.

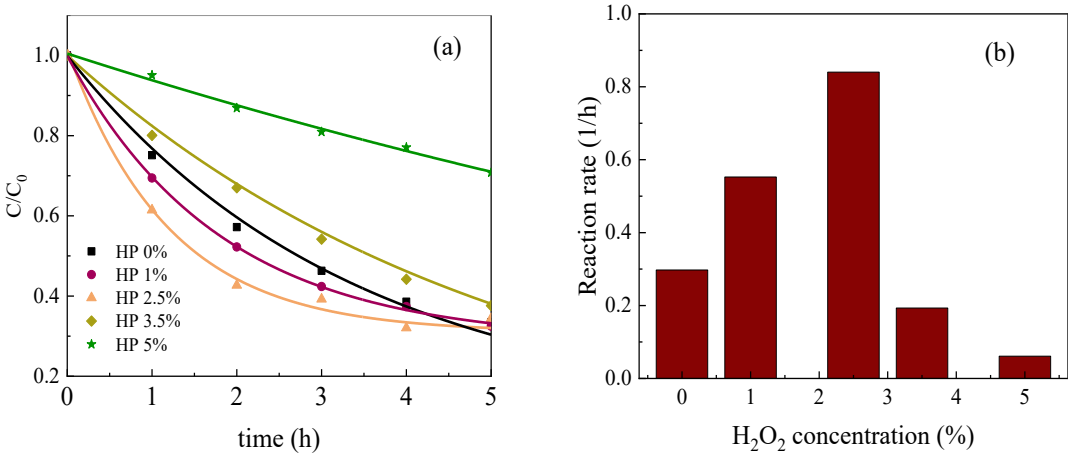

Fig. 4-10 (a) Plots of C/C_0 vs. ultrasonication time in the presence of different concentrations of hydrogen peroxide H_2O_2 when $BaTiO_3$ NPs were used as catalyst, and (b) their calculated reaction rates.

To investigate the possible presence of intermediate compounds, as well as determine the final products of the MO degradation reactions produced by piezo-sono catalysis as well as to establish the MO degradation pathway, liquid chromatography mass spectrometry (LC-MS) has

been used. This analysis was performed using sample of the contaminated water at various times after the catalyst nanoparticles were removed, and the results are presented in Fig. 4-11 (a) and (b) for $BaTiO_3$ and TiO_2 catalyst, respectively. For the solution containing $BaTiO_3$ NPs, a single, intense peak is shown at 3.0 min on the chromatogram, attesting to the existence of MO dissolved in water as shown by the corresponding MS spectrogram of Fig. 4-12 (a). This peak's intensity later drops, which indicates that the concentration of pristine MO decreases as it is degraded during the ultrasonic vibrations. Regarding TiO_2, the results indicate that only 5% of the MO remains after a duration of 6 hours. This finding demonstrates a significant disparity compared to the quantitative values obtained from the UV-Vis spectrophotometry results depicted in Fig. 4-5 (b) and (d). By $t = 2h$ and at subsequent times, a few additional peaks do reveal that several intermediate products have been created throughout the piezo-sonocatalysis process. It is important to note that when the ultrasonication duration in $BaTiO_3$ increases, the intensity of each of these peaks falls noticeably (a similar behaviour is also observed for the samples with TiO_2 catalysts). According to Fig. 4-12 (a), these peaks represent several organic byproducts that were identified by MS. Mass spectroscopy, for instance, reveals that the peak at 1.99 min is primarily indicative of a product with m/z = 248 (product D), or that the major peak at 1.87 min is indicative of a product with m/z = 290. (Product C). Using this information, a possible mechanism for MO's degradation is proposed, which is shown in Fig. 4-12 (b). These results indicate that piezo-sonocatalytically produced $^{\bullet}OH$ free radical attacks MO, resulting in an aromatic substitution of one of the benzene rings for a hydroxyl group and the creation of an intermediate product B (m/z = 320). The methyl group of this product is replaced by hydrogen atoms in the following step, resulting in a variety of products, such as product C (m/z = 290) [17, 18]. Under the attack of active species like $^{\bullet}OH$, the product C is further decomposed to product D. This process continues until all the large molecules are degraded, leaving behind the smaller molecules.

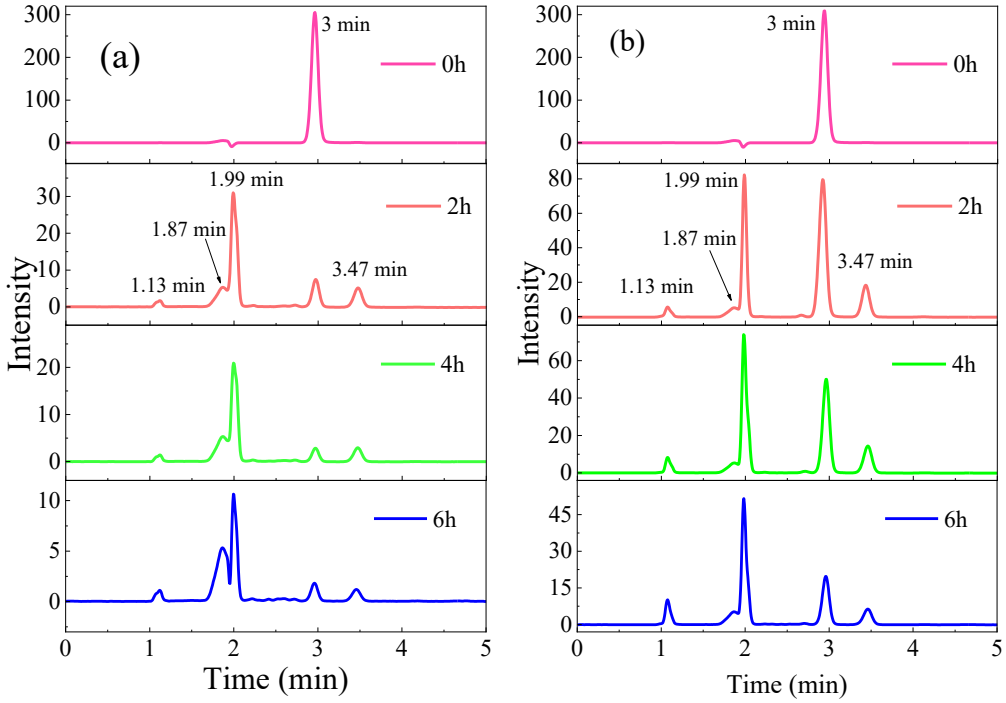

Fig. 4-11 Chromatogram obtained for different ultrasonication times from the MO- contaminated water in which (a) $BaTiO_3$ and (b) TiO_2 nanopowders were used as catalyst,

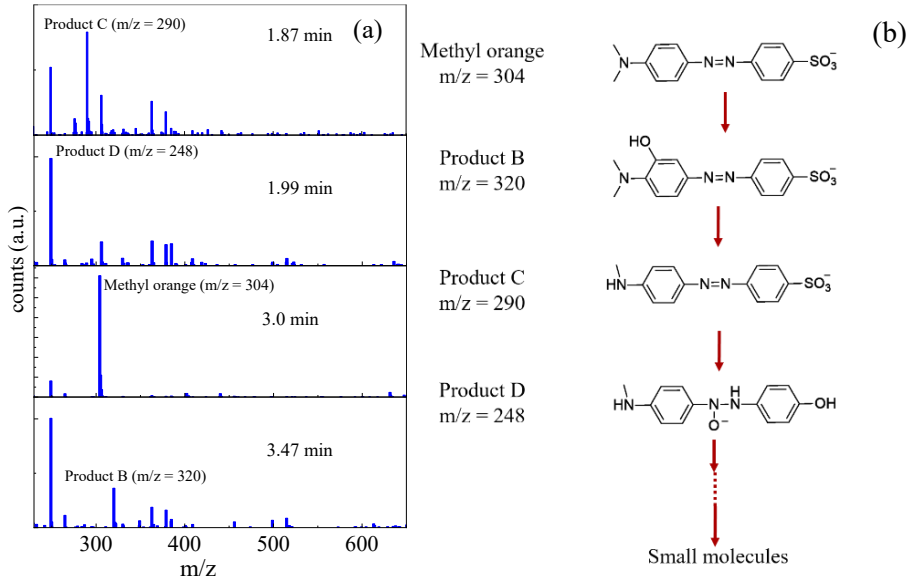

Fig. 4-12 (a) Mass spectrometry spectrogram corresponding to the degradation of MO after 2h of ultrasonication with $BaTiO_3$ NPs as catalyst and corresponding to the peaks shown on the second panel (2h) of Fig. 4-11(a), (b) Schematic illustration of the proposed pathway of MO when $BaTiO_3$ is used as catalyst of the degradation.

4-2-6 Discussions

The catalytic activities of $BaTiO_3$ and other piezoelectric materials has been explained by models generally based on the generation of a piezo-potential across the piezoelectric material [13, 67]. According to the literature, in these models, the piezo-potential is induced periodically on the surface of the nanoparticles by the high pressure resulting form the shock waves generated by the collapse of water cavitation bubbles or even by the regular hydrostatic pressure of the mechanical waves. While there are acoustic pressure waves in the solution already due to the ultrasonication itself, the additional shockwaves due to cavitation add to these effects, and moreover, the nanoparticles almost certainly act as nucleation sites for the bubble formation, hence for their collapse and cavitation. It is estimated that the local pressure on the surface of the nanoparticles generated by the implosion of the cavitation bubbles can reach up 10^8 Pa [44]. Although, due to the small size of the nanoparticles, only a fraction of approximately 10^4 Pa of this pressure difference can be felt by the ferroelectric $BaTiO_3$ nanoparticles (with regard to the ultrasound wavelength of ~1cm). This pressure, however, may be large enough to mechanically deform the crystal structure sufficiently to stimulate the appearance of piezoelectrically-generated charges, hence of a piezo-potential [126]. Indeed, the variation of the piezoelectric nonzero dipole in the crystal lattice causes the appearance of bound negative and positive charges on the opposite sides of the piezoelectric nanoparticles. It is important to note that – for insulating materials that do not have free charges available - the polarization bound charges on the surface of the piezoelectric nanoparticles cannot be transferred to the external medium, and they just generate an electric field around the particles. An electric double layer consisting of anions or cations will therefore be produced in the vicinity of the polarized surfaces of the nanoparticles that can then promote the generation of free radicals and the redox reactions required to degrade the pollutants.

The results of our experiments showed that both piezoelectric $BaTiO_3$ and non-piezoelectric TiO_2 are acting as a catalyst when submitted to ultrasonic vibrations, clearly demonstrating the existence of a non-piezoelectric contribution to the catalytic activity of TiO_2 (i.e. tribo- or sonocatalytic), and most probably to that of $BaTiO_3$ too. Using the same ultrasonic bath that was used for the $BaTiO_3$ catalyst NPs, we observed that the catalytic reaction rates obtained by TiO_2 catalysts, although smaller than those for $BaTiO_3$, were substantial. Like with $BaTiO_3$, we observed a meaningful change in the catalytic efficiencies by increasing the concentrations of the

TiO_2 nanoparticles. It follows from our experiments that the catalytic activity of non-piezoelectric TiO_2 cannot be explained by the same mechanism as for $BaTiO_3$ because, unlike $BaTiO_3$, none of the known crystalline phases of TiO_2 have ever been reported to show piezoelectric properties. It also can't be explained by the tribocatalytic effect, as the concentrations of the catalytic nanoparticles chosen in this study was minimal related to the research done by others [127, 128]. Indeed, there is less than one particle per volume of 5 μm^3 of liquid in our measurements, limiting the chance of particles collisions and reducing the possibility to triboelectrically generate surface charges on the nanoparticles surfaces. It should be noted, however, that the triboelectric effect has already been invoked in the literature to describe the interaction between the particles and the PDMS materials of the magnetic stirrer [129-131]. An additional argument disqualifying tribocatalytic activity as a possible explanation of our results is that a large increase in the amount of TiO_2 nanopowder, which should increase considerably the possibility of particles mutual contact and friction, did not increase the catalytic reaction rates significantly. Moreover, triboelectric charges are generally generated by the friction of different materials, which is not the case here. Instead, our results can be well explained by sonocatalytic models. The ultrasonic waves can lead to the production and growth of macro and micro-size bubbles in liquids, and their subsequent implosion can releases vast amount of localized energy [43]. The transient conditions generated by such cavitation, specifically the local hot temperature of up to 5000 K generated by the collapse of the cavitation bubbles, may locally release enough energy to cleave water molecules and produce hydroxyl radicals (.OH), which in turn can act as oxidant agent in the catalytic reactions [45]. Beside the production of the hydroxyl groups, the extreme local conditions on the surface of the semiconductor catalyst particles in the liquid could cause the electrons in the valence band to jump up to the conduction band. These electrons in an excited state, together with the free radicals inside the contaminated water, would all participate in the catalytic reaction to decompose the organic dyes.

In order to estimate the relative contributions of the sono- and piezo- electrical effects to the catalytic properties of $BaTiO_3$ nanoparticles, we compared its catalytic activity with that of TiO_2, often taken as a standard in catalysis, and also because of its similarity with the TiO_2-terminated surface of $BaTiO_3$ as already mentioned. Assuming that half of the surface of $BaTiO_3$ is TiO_2-terminated, and that its BaO-terminated surface is catalytically inactive, we assume that the

sonochemical contribution for the $BaTiO_3$ nanoparticles is very similar to that of the anatase TiO_2 nanoparticles and, therefore, we attribute it a value corresponding to half of that of the TiO_2 nanoparticles of the same size. According to our simple model, the pure piezoelectric catalytic reaction rate. i.e., the contribution of the piezoelectric properties of $BaTiO_3$ to its total catalytic activity, is the difference between the catalytic reaction rates experimentally obtained for $BaTiO_3$ NPs and half the catalytic reaction rates measured for TiO_2 NPs. Noting that the real number of particles is a function of their molar concentration, it can be said that 88% of the overall catalytic reaction of $BaTiO_3$ at room temperature is the contribution of the piezocatalysis, while about 12% of its catalytic activities is due to the sonocatalysis, the latter being present in both piezoelectric and non-piezoelectric catalysts nanoparticles. This is consistent with the temperature dependent measurements of $BaTiO_3$ catalytic activity (Fig. 4-7) by taking note that increasing the temperature reduced the piezocatalytic contribution and slightly increase its sonocatalytic activities. Comparing the reaction rates at room temperature with those at 70°C, and assuming that at 70°C the piezoelectric properties of nanoparticles of the size used in these experiment almost vanishes as the temperature approaches the tetragonal ferroelectric to cubic paraelectric phase transition temperature, a contribution of more than 80% to its catalytic activity can also be attributed to the piezoelectric properties of $BaTiO_3$, consistent with and conforming the results obtained from comparison of $BaTiO_3$ and TiO_2 nanoparticles.

4-3 Temperature dependencies of $BaTiO_3$ catalytic activities

The temperature and size of the $BaTiO_3$ piezoelectric nanoparticles are the two main parameters affecting their piezocatalytic activities since it has been clearly demonstrated that the piezoelectric properties of $BaTiO_3$ are strongly dependent on these two parameters [4, 5]. In this study, $BaTiO_3$ powders with three different grain sizes were investigated and their catalytic activities toward the degradation of MO, a well-known anionic dye, was characterized at different temperatures. The dependence of the catalytic activity on the particle size and temperature should help evaluate the contribution of the piezoelectric properties to the catalytic activity. The measurements of the $BaTiO_3$ powders piezocatalytic activity are conducted by measuring the organic dyes decomposition under ultrasonic vibrations below the boiling point of water, while the evolution of the local symmetry of these powders as a function of temperature

was investigated by temperature dependent Raman spectroscopy. Since the spontaneous polarization of $BaTiO_3$ has a strong dependence on temperature in the vicinity if the transition temperature, and assuming a weak temperature dependence of the other catalysis components in the temperature range investigated, the evolution of the overall catalytic activity with temperature can be used to separate the piezoelectric behavior from the other possible catalytic reactions such as sonocatalysis. It is shown that the piezocatalytic degradation of organic pollutant using $BaTiO_3$ powders under ultrasonication is size dependent and exhibit a sudden decrease at the site-dependent phase transition temperatures.

4-3-1 Particles morphology

Fig. 4-13 (a)–(c) show TEM images of the $BaTiO_3$ nanoparticles with their corresponding particle size distributions. For the 50 nm $BaTiO_3$ powder, the nanoparticles are monodispersed to some extent. However, there is a slight agglomeration resulting from short duration of ultrasonication of the dispersed powder. In the case of $BaTiO_3$ nanoparticles with sizes of 100 nm and less, TEM image shows irregular grain morphology with a combination of cubic and quasispherical shapes. From the histogram in the Fig. 4-13 (a) and (b), the average particle sizes of these two samples are estimated to be 53.8±11.3 nm and 96.3±18.3 nm, respectively. The bulk powder is made up of agglomerated particles, which were somewhat difficult to disperse homogeneously during ultrasonication. The dark contrast is due to size constraint arising from the fact that micron-sized particles are known to be less transparent to the electron beam. The average particle size estimated is 1.5±0.5 μm.

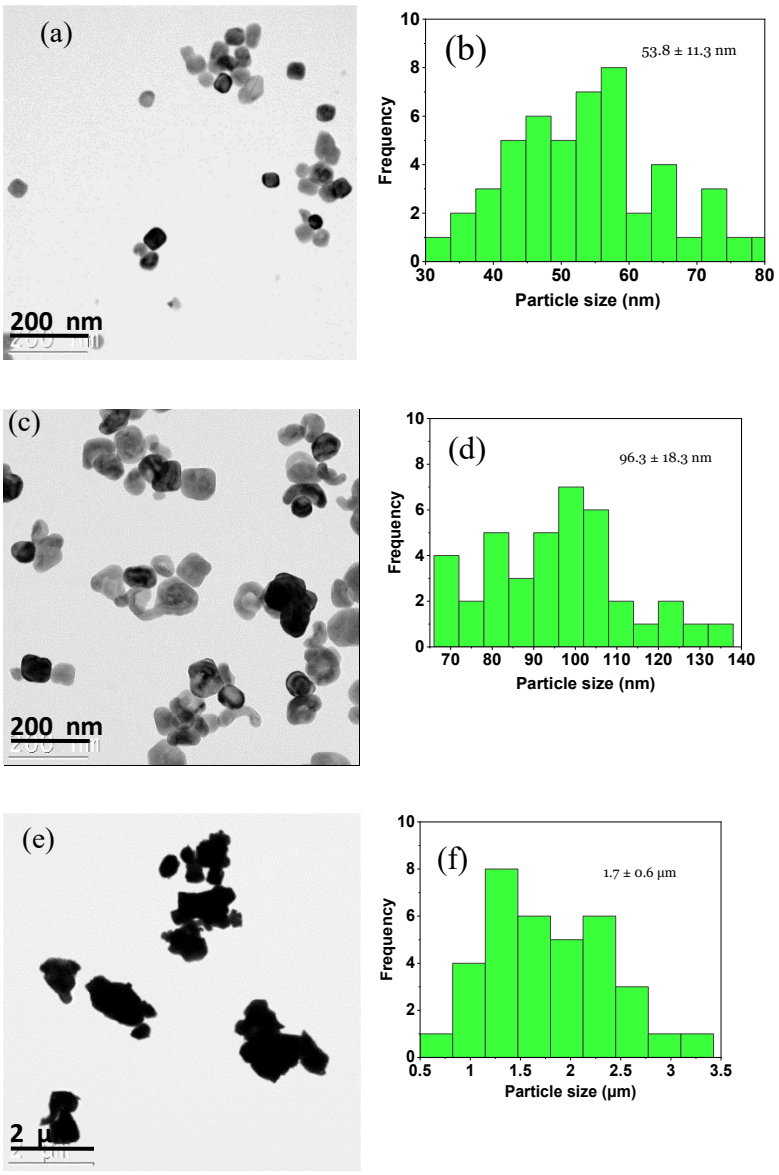

Fig. 4-13 TEM micrography and their relative size distribution of the particles with nominal sizes of (a), (b) 50 nm, (c), (d) 100 nm, and (e), (f) 2 µm.

4-3-2 Structural effects

X-ray diffraction is used to investigate the crystal structure of the powders. The results of the XRD are shown in Fig. 4-14 (a). With the main patterns of the tetragonal phase of $BaTiO_3$ according to the literature (JCPDS: 01- 089-1428), the diffractions of the three $BaTiO_3$ powders are similar. The only noticeable difference is in the two peaks located at $2\Theta = 45^{o}$ that are distinctly separated in the powder sample with the size of 2 µm, and are attributed to the (002) and (200) planes, respectively (Fig. 4-14 (b)-(d)). The high-resolution peak acquisition around

$2\Theta = 45^{o}$ in all these three samples shows an asymmetry due to the fact that it consists of 2 peaks and can be fitted with two Gaussian peaks as is shown in Fig. 4-14 (b)-(d). This splitting reveals a tetragonal distortion caused by an increase in the out-of-plane lattice parameter *c* in comparison to the in-plane lattice parameter *a*. Theoretical studies suggest that the tetragonal distortion decreases with the size of the particles [6]. Accordingly, the ratio *c* over *a* for each sample, which is the representative of the tetragonality, has been measured. The measured *c/a* decreases with the size of the particles from 1.0076 for the 2 μm powder to 1.0028 for the 50 nm particles. The following empirical functions has been proposed [7] to describe the tetragonal dependency to the size of the particles:

$$\frac{c}{a}(d) = \frac{c}{a}(\infty)\left[1 - \frac{A}{d-d_1}\right] \qquad (4\text{- }7)$$

In which $c/a(d)$ is the tetragonality of the crystal with a particle with size d, $c/a(\infty)$ is the tetragonality value of the bulk, and A, and d_1 are fitting parameters. The results of the *c/a* vs. the particles size are shown in Fig. 4-14 (b). By considering the fits, it can be considered that the tetragonality of the particles with the sizes of 2 μm is close to the bulk values reported in the literature [8]. The fitting parameter *A* in the formula (4-7) obtained is 0.19. It's important to note that the *c/a* decrease with the particle size is due to the decrease of the *c* lattice parameter, which is related to the decrease of the spontaneous polarization in the $BaTiO_3$ crystal structure with decreasing size. The d_1 parameter was measured to be 11.09 nm, and represents the critical size of the particles below which spontaneous polarization is not present anymore in the $BaTiO_3$ structure in agreement with previous reported studies [9].

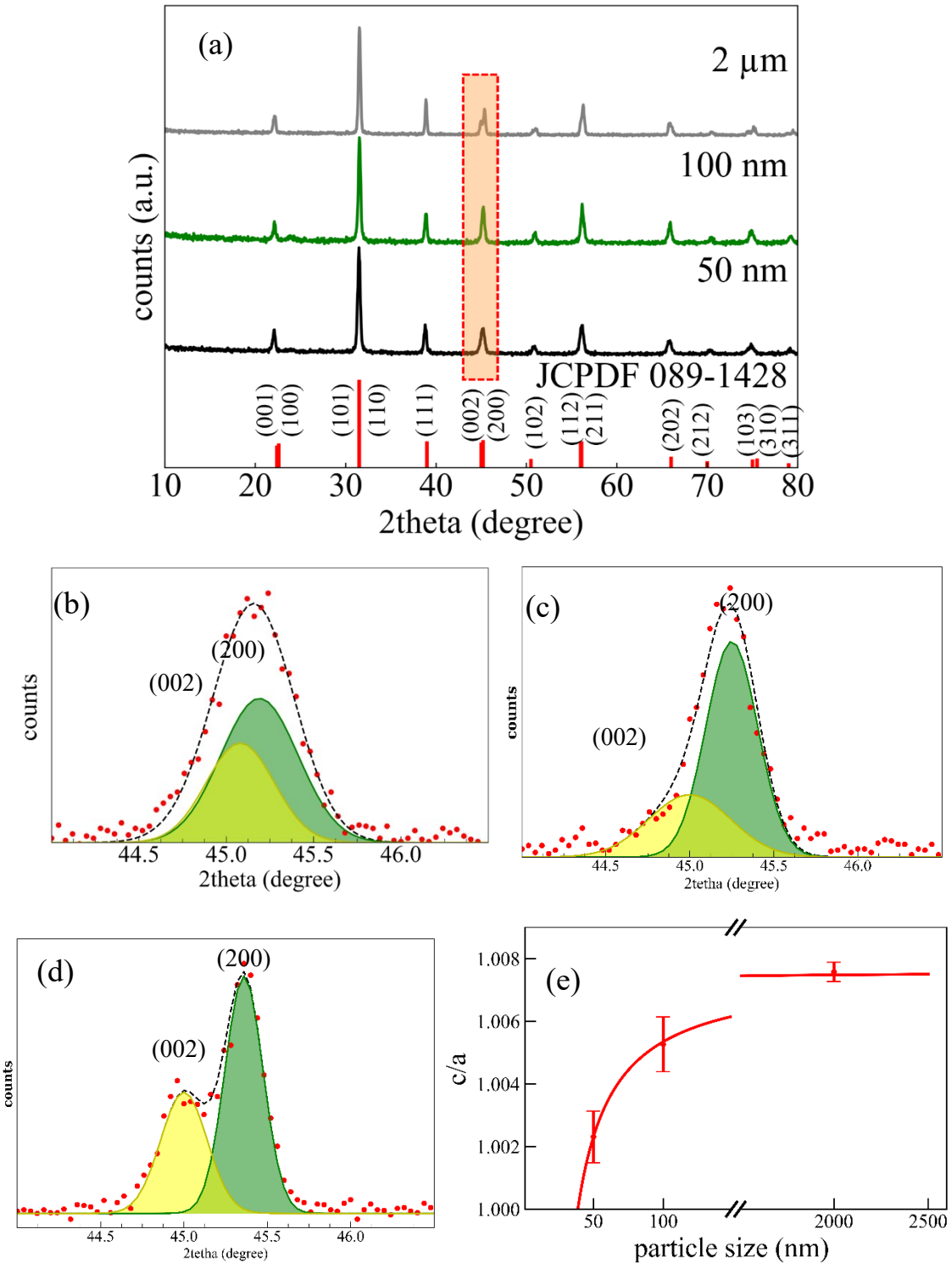

Fig. 4-14 (a) X-ray diffraction patterns of different $BaTiO_3$ powders, and the high resolution diffraction spectra around $2\Theta = 45^{\circ}$ to discriminate between (200) and (002) planes in $BaTiO_3$ powders with the size of (b) 50 nm, (c) 100 nm, (d) 2 µm , and (e) the results of the calculated c/a values as a function of the particles size calculated from (b), (c), and (d) .

4-3-3 Raman spectroscopy

Regardless of their size dependence, it is well known that the piezoelectric properties of $BaTiO_3$ strongly depend on temperature, especially in the vicinity of the tetragonal to cubic phase transition. The effect of temperature on the $BaTiO_3$ structural evolution has been examined using Raman spectroscopy. A literature review reveals that the first order Raman spectra of tetragonal $BaTiO_3$ includes 10 active phonon modes containing transverse and longitudinal optical modes, without considering the splitting of transverse and longitudinal optical modes, nor the splitting due to differing polarizability in each unit cell direction (when considered, there would be 18 distinct and independent Raman-active modes) [9]. The Raman spectra of the different sizes of $BaTiO_3$ powders were measured at different temperatures up to 140 ^oC, with the aim to estimate the Curie temperature of the different powders. As described in the previous section, smaller particles are closer to the transition into the cubic paraelectric phase, and are therefore expected to have a lower phase transition temperature. The Raman raw data were corrected using the Bose-Einstein thermal factor [10], thus allowing a direct comparison of the spectra obtained at different temperatures.

$$I_C(\omega) = I(\omega)[n(\omega) + 1] \qquad (4\text{-}8)$$

where $I_C(\omega)$ is the corrected intensity of the Raman spectra, $I(\omega)$ is the Raman intensity of the acquired spectra, and $n(\omega)$ is the Bose-Einstein occupation number (phonons are bosons). $n(\omega) + 1 = \left[1 - \exp\left(-\frac{\hbar\omega}{kT}\right)\right]^{-1}$ with ω the phonon frequency, T the temperature, $\hbar$ and k are the Planck and Boltzmann constants, respectively.

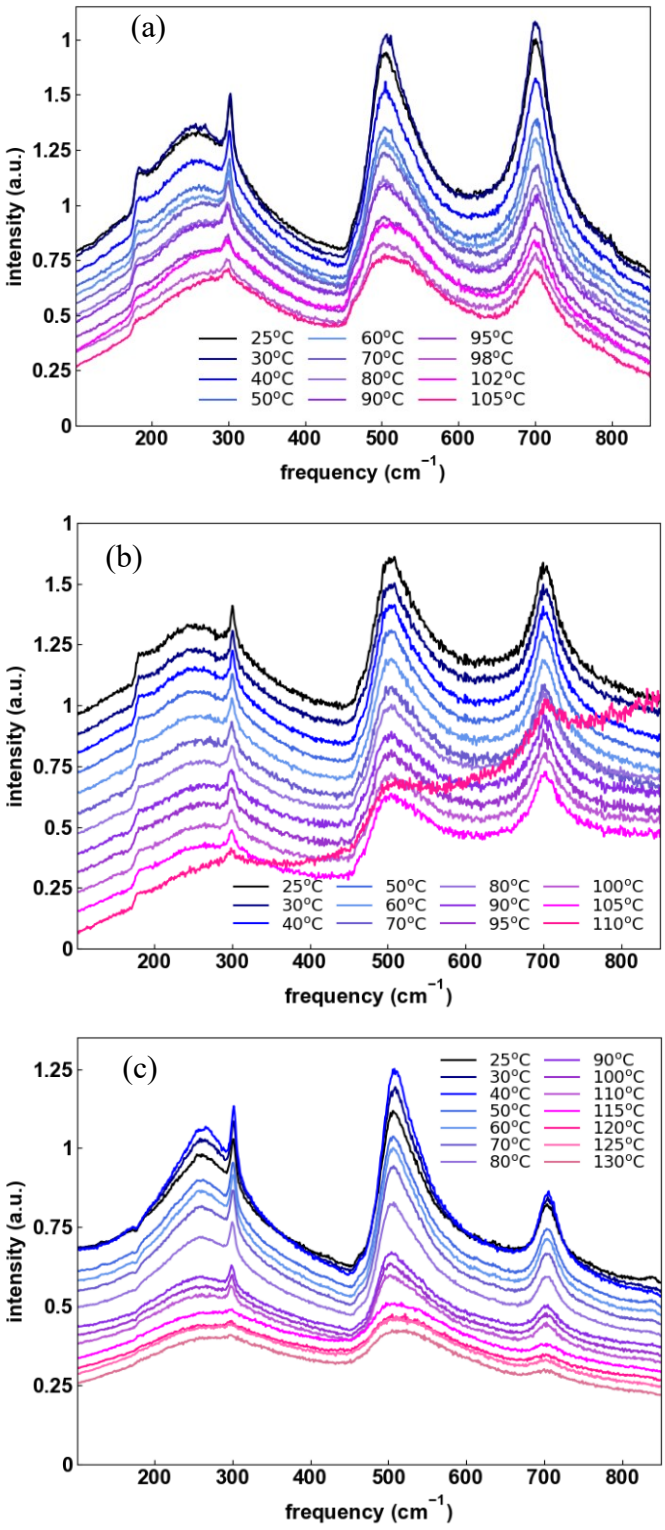

Fig. 4-15 Raman spectra of the powders with the sizes of (a) 50 nm, (b) 100 nm, and (c) 2000 nm at different temperatures,

The corrected Raman spectra for the powder samples at different temperatures are shown in Fig. 4-15. It is observed that the Raman spectra measured at RT for the 50 nm powders are consistent with those reported in the literature [11]. While the cubic phase of $BaTiO_3$ is Raman silent, the tetragonal phase of $BaTiO_3$ exhibit characteristic peaks located at 301 cm^{-1} and 715 cm^{-1}, which are attributed to the B1 + E(TO3 + LO2) and A1 + E(LO3 + LO4) phonon modes, responsible for Ti-O torsional vibration in the TiO_6 octahedra. The measured peaks located at 507 cm^{-1} is attributed to TO3 of the A1 symmetry. In addition, there are two peaks located at 180 cm^{-1} and 267 cm^{-1}, which are assigned to TO1 and TO2 modes of the A1 symmetry, respectively. The corresponding results obtained from the powders with the sizes of 100 nm, and 2 μm can be seen in Fig. 4-15 (b) and (c). It is noticed that the peak at 180 cm^{-1} for the nanoparticles is not present in the Raman spectrum of the quasi-bulk 2 μm powder (Fig. 4-15 (b)). Instead, there is a dip observed at this position that has been reported to be representative of bulk $BaTiO_3$ [132]. The effect of the increase in temperature is clearly visible on the aforementioned characteristic modes (i.e. B1 + E and A1 + E) indicative of the tetragonality, as their peak intensities get reduced and asymmetrically broadened. Fig. 4-16 (a) shows the normalized peak intensity (the ratio of the peak intensity at 301 cm^{-1} to the one at 507 cm^{-1}, which is supposed to be temperature-independent, divided by the room temperature intensity) for the B1 + E mode. As seen from the Fig. 4-15 (a), the intensity decreases as the temperature increases. This is an indication that the room temperature tetragonal phase is affected thermally and structurally transforms to the high-temperature cubic phase above a certain critical temperature, known as the Curie temperature (T_c). For the 50 nm, 100 nm and the 2 μm, the T_c obtained are 102, 113, and 124 ºC, respectively. It has to be noted here that the normalized intensity displayed in Fig. 4-16 (a) indicates the tetragonality of the $BaTiO_3$ structure. One supposition suggests that there exists a direct correlation between the qualitative notion of tetragonality and the quantitative c/a ratio value. Indeed, knowing the room temperature crystal distortion (*c/a*) from XRD results, if we assume a linear relationship between the normalized peak intensities defined above and *c/a*, the tetragonality of each crystal at different temperatures can be obtained from the Raman data, as shown in Fig. 4-16 (a). The critical temperature in ferroelectric or ferromagnetic materials has been studied as a function of size in different researches [133, 134]. Among these models, Yang model that has been stablished based on the form of the size dependent cohesive energy model is

widely used for the ferroelectric materials [135]. The simplest form of this model can be written as below:

$$T_c(d) = T_c(\infty)(1 - \frac{d_2}{d-d_2})exp(-\frac{B}{d-d_2}) \qquad (4\text{-}9)$$

where $T_c(\infty)$ is the Curie temperature of the bulk, B is a fitting parameter and d_2 is the critical size to be determined. The fitting curve used to estimate d_2 is shown in Fig. 4-16 (b), and it yields a value of d_2 = 7.2 ±2.8 nm, denoting the critical size at which a tetragonal crystallite would undergo a structural phase transformation when heated. This critical size is consistent with the critical size d_1 ~ 11 ±3 nm obtained from XRD analysis.

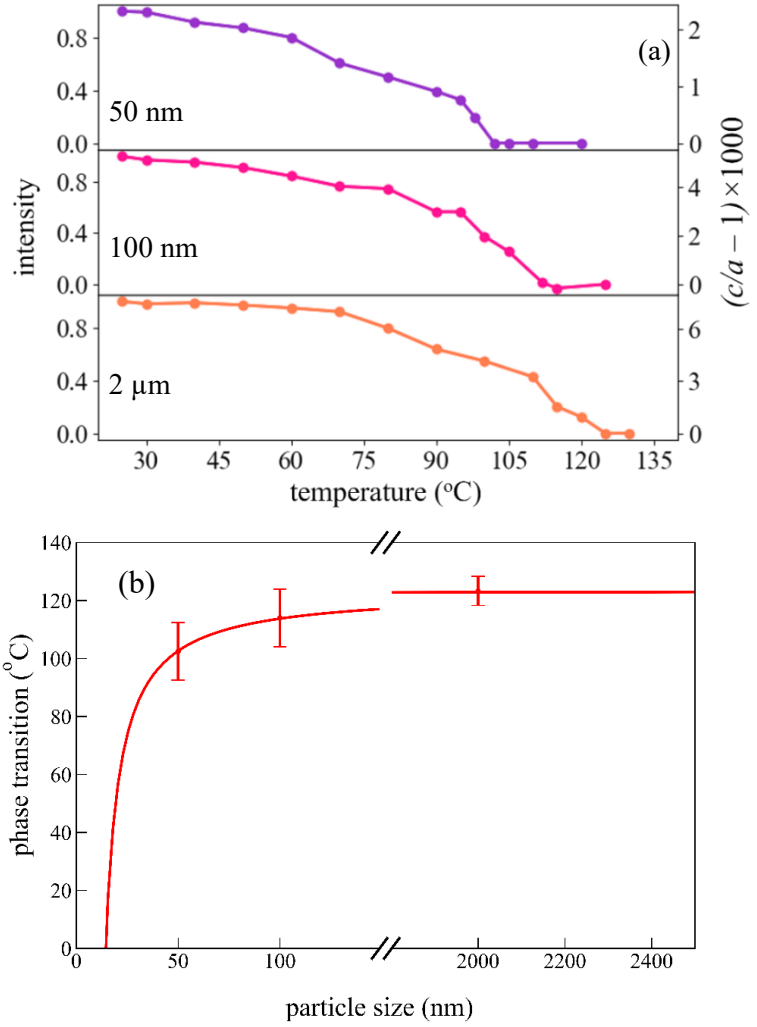

Fig. 4-16 (a) Normalized peak intensity of the line at 301 cm^{-1} at different temperatures, obtained for powders of different sizes, and (b) Empirical fitting function obtained from the tetragonal-cubic phase transition temperatures obtained from the temperature-dependant Raman spectra.

4-3-4 Piezocatalysis characterizations

The ultrasound-assisted catalytic properties of $BaTiO_3$ particles were investigated using the degradation of the organic dye methyl orange. The concentration of the catalytic materials in each measurement was fixed to 1 g/L. According to the literature, this concentration is the optimal value, and increasing it has been reported to not noticeably improve the catalytic performance [12, 13]. Our own experiments do indeed confirm that increasing the catalyst particles concentration beyond 1g/L doesn't significantly improve their catalytic performance. The absorption of monochromatic light with a wavelength of 405 nm, which is well within the absorption band of MO, gives us a quantitative indication of the decomposition of this organic compound after different ultrasonication times, the more MO decomposition, the less light absorption. It is evident that the gradual disappearance of MO can be assessed with naked eye as the solution color is changing and becoming less intense, and eventually transparent. We observed that as well ultrasonication without the presence of catalyst material and the presence of catalyst material without ultrasonication do not result in any changes and therefore that the simultaneous presence of both ultrasounds and catalyst material (such as $BaTiO_3$ particles) is necessary for the decomposition of organic dyes. The experiment for each sample was done at six different temperatures from 25 to 70 ^oC and the results are shown in Fig. 4-17 (a)-(c). Among different sizes of $BaTiO_3$ powders, the samples with the powder of sizes 50 nm show the best catalytic results at RT, while the sizes 2 μm of $BaTiO_3$ yields the lowest catalytic performance. Assuming a direct relationship between the light absorption and the concentration of the MO present in the solution, it is observed that this powder degrades more than 90% of the organic dyes after 4 hours of ultrasonic vibrations (Fig. 4-17 (a)). It has also been observed for all samples that the dye degradation rate decreases when the temperature increases. The reaction rate of the dye degradation has been obtained from equation (4-7). The results of K_{obs} obtained by this fitting method are shown in Fig. 4-18 (a) as a function of temperature for different powder sizes. It is striking that the catalytic activity assessed from the experimentally measured ratio ($C_t/C_{0)}$ decreases by more than 80% for the 50 nm $BaTiO_3$ powder when the temperature increases, while for the $BaTiO_3$ 2 μm powders and even for the 100 nm $BaTiO_3$ powders having much lower catalytic activities at RT, the reaction rate does not decrease so drastically with increasing temperature. The catalytic MO decomposition reactions of non-piezoelectric TiO_2 nanoparticles with a size of 100 nm, which are often used as a reference in catalytic reactions,

has been investigated in our previous study [14]. We have reported a better catalytic reaction rate for $BaTiO_3$ nanoparticles than for TiO_2 nanoparticles with the same size and morphologies for the degradation of MO under ultrasonication, which was attributed to piezocatalytic activity in $BaTiO_3$ not available in its TiO_2 counterpart. The catalytic reaction rates for the anatase TiO_2 nanocatalysts has been added to Fig. 4-18 (a) for comparison. According to these results, the K_{obs} decrease with temperature for all $BaTiO_3$ powders. This is in contrast with the reaction rate for the TiO_2 nanopowder that slightly increases with temperature. This slight increases for TiO_2 when increasing the temperature, has also been previously reported in the literature [15]. This stark difference in the temperature dependence of the catalytic reaction rates of $BaTiO_3$ and TiO_2 powders shows that the physical phenomena at the origin of the catalytic reactions in $BaTiO_3$ and TiO_2 nanoparticles are different. The temperature dependence of the catalytic activity of $BaTiO_3$ particles can be explained well by the temperature dependence of the piezoelectric properties of tetragonal $BaTiO_3$. Since the magnitude of the piezoelectric effect of $BaTiO_3$ is dependent on the magnitude of the distortion of its crystal structure from its centrosymmetric cubic structure, which in the tetragonal phase is characterized by the *c*/*a* ratio, it is therefore interesting to investigate the correlation between the catalytic reaction rates and the *c*/*a* ratio of the $BaTiO_3$ particles of different sizes. The *c*/*a* ratio at room temperature has been obtained for each sample from the XRD and the Raman characterization discussed above (Fig. 4-16), and we know that it drops down to 1 at the phase transition temperature.

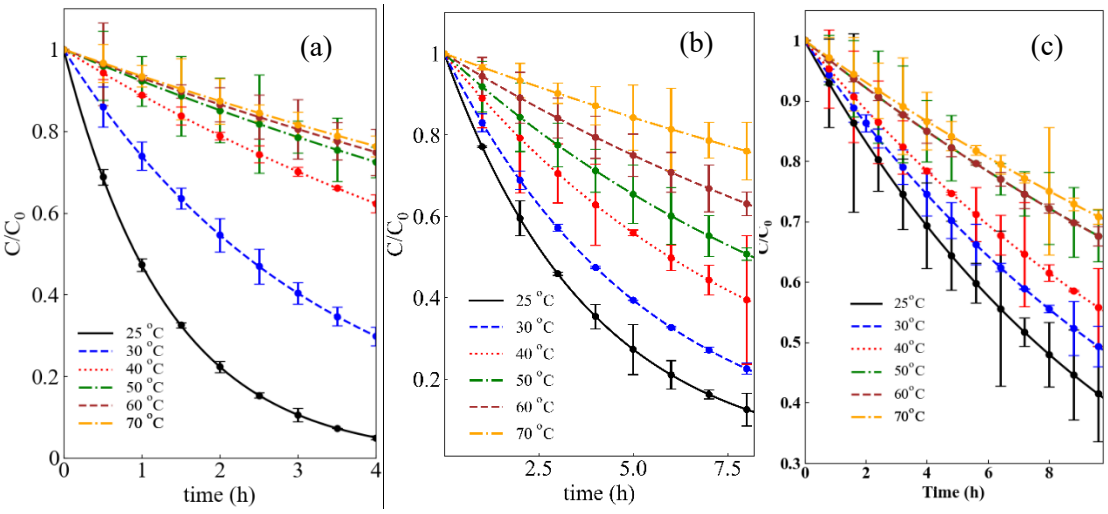

Fig. 4-17 Methyl orange dye degradation at different temperatures using the $BaTiO_3$ with a size of (a) 50 nm, (b)100 nm, (c) 2000 nm.

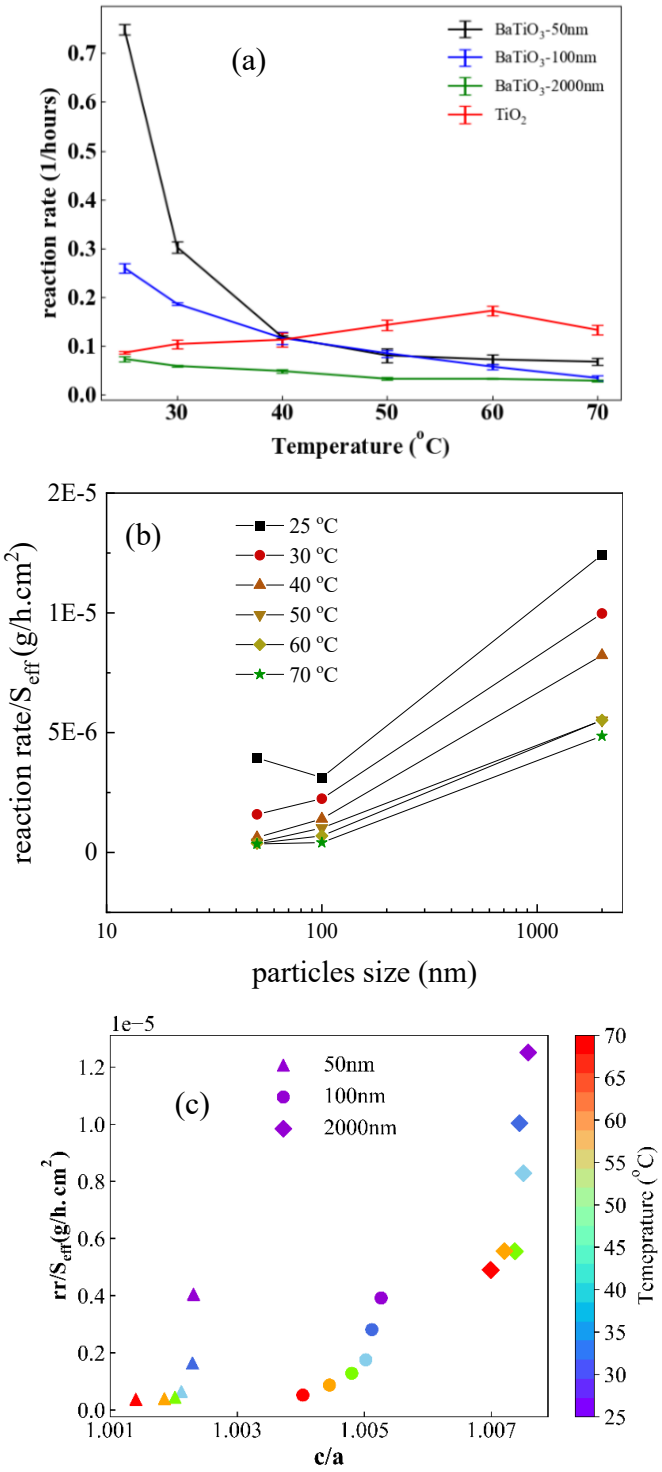

Fig. 4-18 (a) Temperature dependency of the catalytic reaction rates powders of $BaTiO_3$ of different size and TiO_2 particles. (b) The effective reaction rates plotted for each individual temperature as the function of particle size, (c) Effective reaction rate of the different powders as a function of the tetragonality c/a obtained from the Raman spectra at different temperatures (rr/S_{eff} is the reaction rate divided by the effective surface of catalyst particles).

Fig. 4-18 (a) shows that the catalytic activity of the smaller sizes $BaTiO_3$ particles in an ultrasonic bath is larger and more sensitive to the temperature. It is obvious that with the same weight concentration of the catalysts dispersed in contaminated water, the effective surface available for the catalytic reaction is larger for smaller particles, which was not considered in our results so far. In order to discuss the relation between the catalytic reaction rate and the piezoelectric potential, we therefore calculated a reaction rate per unit surface by dividing the reaction rates obtained by the effective surface of the catalyst particles used in each measurement (the particles were assumed spherical with a diameter corresponding to the average sizes obtained from the TEM image analysis). According to this definition, S_{eff} is, for each corresponding powder, the net surface of the catalyst particles for 1 gr of weight. These results together with the *c/a* obtained from the Raman spectra at different temperatures can gives us a relation between the kinetic reaction rates vs. structural parameters (e.g. tetragonality) for each particle size. These *effective reaction rates* plotted for each individual temperature that clearly shows the same behavior when plotted in function of particle size as are shown in Fig. 4-18 (b), namely a decrease with temperature and an increase with particle size. These values have also been plotted in Fig. 4-18 (c) in function of the *c*/*a* ratio describing the tetragonality of the $BaTiO_3$ crystalline grains. In contrast to the reaction rates of Fig. 4-18 (a), the *effective reaction rates* obtained from different powder sizes are now comparable and are larger in the largest particles. This is due to the size dependency of the ferroelectric spontaneous polarization and of the piezoelectric coefficients which are larger in bigger particles (because, at the temperature of the measurement, they are further away from the transition temperature), and therefore yield higher piezopotential for the catalytic chemical reactions [5].

4-3-5 Discussion

Indeed, piezocatalysis is dependent on the piezoelectric coefficients of the material used as catalyst. It has been reported that among different piezoelectric coefficients, this is the shear stress coefficient (d_{15}) that is the most important one to promote the piezocatalytic activities of $BaTiO_3$ [19, 20]. According to the theory of Landau–Ginzburg–Devonshire (LGD) [21], the different dielectric coefficients of $BaTiO_3$ can be written as follows:

$$d_{33} = 2\varepsilon_0 Q_{11} \eta_{33} P_s \qquad (4\text{-}10)$$

$$d_{31} = 2\varepsilon_0 Q_{12}\eta_{33}P_s \quad (4\text{-}11)$$

$$d_{15} = \varepsilon_0 Q_{44}\eta_{11}P_s \quad (4\text{-}12)$$

In which P_s is the spontaneous polarization, η_{ij} is the dielectric susceptibilities, and Q_{ij} are the electrostrictive coefficients. It has been shown that for the tetragonal $BaTiO_3$ in the temperature range of 20-100°C, d_{15} dominates the two other coefficients, and more importantly, it decreases when the temperature increases up to the tetragonal-cubic phase transition temperature [22]. It has been shown that increasing the temperature up to 90°C decreases the d_{15} piezoelectric coefficient of $BaTiO_3$ ceramics by about 50% compared to that at RT [23]. We also know that the piezoelectric coefficient is size dependent so that it increases significantly by about two orders of magnitude when the size of the $BaTiO_3$ particles increases from a few nanometers to a few micrometers [24, 25]. Like for any electrochemical reaction, there is a minimum electrochemical potential for the catalytic reactions to occur [26]. With lower piezopotential, this threshold is likely to be reached when the temperature increases for the smaller powders. This explains well that why the catalytic reaction rates quench drastically with the smaller $BaTiO_3$ nanoparticles when the temperature increases (Fig. 4-19). The screening charge model, which predicts that surface potentials below a threshold won't be able to perform chemical reactions, provides a good explanation for the cutoff in the catalytic reaction rate process depicted in this image. The screening charge model, which predicts that surface potentials below a threshold won't be able to perform chemical reactions, provides a good explanation for the cut-off in the catalytic reaction rate process depicted in this image. The screening charge model, which predicts that surface potentials below a threshold won't be able to perform chemical reactions, provides a good explanation for the cutoff in the catalytic reaction rate process depicted in this image. According to these results, one can say that our results are consistent with the 'charge screening effect' model to explain the piezocatalysis process. However, due to the complexity of the system the electron-hole redox reaction process may still exist partially which is mostly dominated by the sonocatalysis process.

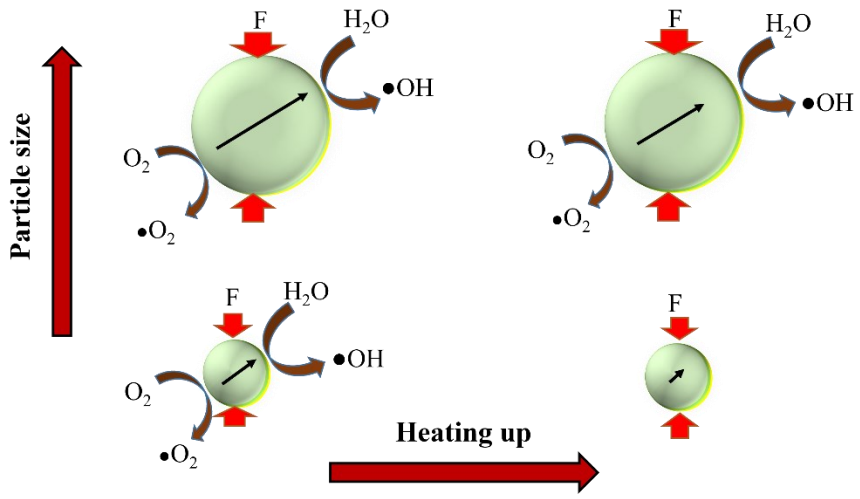

Fig. 4-19 The variations of the piezopotential with temperature in particles with different sizes

The temperature dependency of the catalytic activities of $BaTiO_3$ confirms its strong relationship with its piezoelectric properties. Such a behavior has not been observed in non-piezoelectrics such as TiO_2. Sonocatalytic and tribocatalytic effects have different behaviors when the temperature of the medium increases. Increasing the temperature can help the tribocatalysis to proceed as the probability of the particles frictions increases at higher temperatures [27]. The sonocatalysis is also positively affected by the temperature, as it is basically the temperature of the local bubbles that causes electrons jumps up to the conducting band when the bubbles collapse and thus increasing the medium temperature would help sonocatalysis to proceed, as reported in the literature [28]. The pyroelectric effect is typically observed when there is a time-dependent variation in temperature. It should be noted that this effect arises from the presence of a temperature gradient, which induces polarization in the particles. However, in the experiments conducted in this study, the temperature was maintained at a fixed value during each measurement. Therefore, it can be concluded that the observed process cannot be attributed to the pyroelectric effect. Thus, in general it can be said that the catalytic activities of $BaTiO_3$ particles are dominated by their piezocatalyst properties. Although 70 ^oC is lower than the tetragonal-to-cubic phase transition temperature of $BaTiO_3$ and the nanoparticles should thus still exhibit piezoelectric properties at this temperature, the piezopotential of $BaTiO_3$ nanoparticles seems to be too small to make a significant contribution to their catalyst activity anymore. At 70 °C, the catalytic rates measured for the $BaTiO_3$ particles with sizes of 50 nm and 100 nm correspond to catalytic rates measured for TiO_2 nanoparticles of similar sizes, which could

therefore rather be assigned - for both TiO_2 and $BaTiO_3$ nanoparticles - to sonocatalysis with no contribution of piezocatalysis.

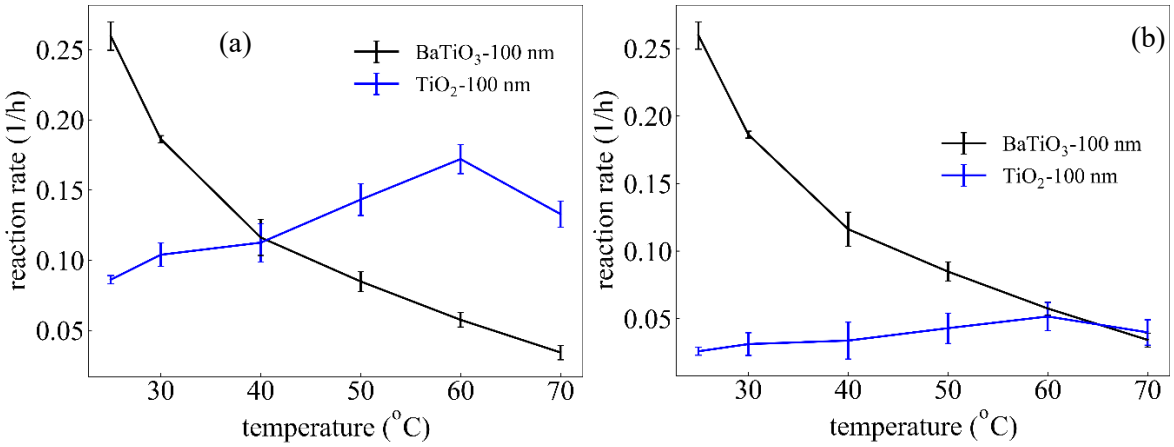

Fig. 4- 20 The catalytic reaction rate of the TiO_2 compared to the $BaTiO_3$ nanoparticles (a) before and (b) after the exerting the effective surface and density corrections.

The difference between the catalytic rates measured at room temperature and temperature lower than 70°C with the reaction rates measured at 70 ºC should then provide a quantitative measure of the contribution of the pure piezocatalysis using these piezoelectric powders. Quantitatively speaking, comparing 1g/L of TiO_2 and $BaTiO_3$ nanopowders with a size of 100 nm in solution needs some corrections. We should consider that we assumed that half of the free surfaces of the $BaTiO_3$ particles are BaO-terminated and half are TiO_2-terminated, and that only the latter are catalytically active. Also, with the same mass of these two catalysts, since TiO_2 has smaller density, the number of dispersed catalyst particles will be 40 % more than that of $BaTiO_3$. The catalytic reaction rate of the 100 nm TiO_2 compared to the $BaTiO_3$ nanoparticles before and after the corrections has been shown in Fig. 4- 20. This clearly shows that the corrected catalytic reaction rete of TiO_2 never exceeds the minimum value measured for the $BaTiO_3$ that confirms our assumption about the estimation of the active surface area of the $BaTiO_3$.

Although 70 oC is still lower than the $BaTiO_3$ tetragonal-cubic phase transition, it appears that the BaTiO3 piezopotential does not play a significant role in catalyst activity at this temperature, at least for the smallest nanoparticles. In other words, the catalytic reaction at 70 ºC is based on sonocatalysis rather than the piezoelectric effect. With the lower tetragonal phase transition, the 50 nm catalyst of $BaTiO_3$ better shows the contribution of each effect. Fig. 4-21 shows the

contribution of the piezo- and sonocatalytic reactions obtained based on these discussions. The catalytic rates of $BaTiO_3$ "corrected" for the effective reactive surface are as follows: the reaction rate for 50 nm $BaTiO_3$ is 0.07 1/h, which is around 10% of the catalytic activities of the same $BaTiO_3$ sizes at RT. In other words, the portion of sonocatalysis (and triboelectric effects) contributing in the catalytic activities in such as experiment is to be around 10 %, and the rest is allocated to its piezocatalytic activities.

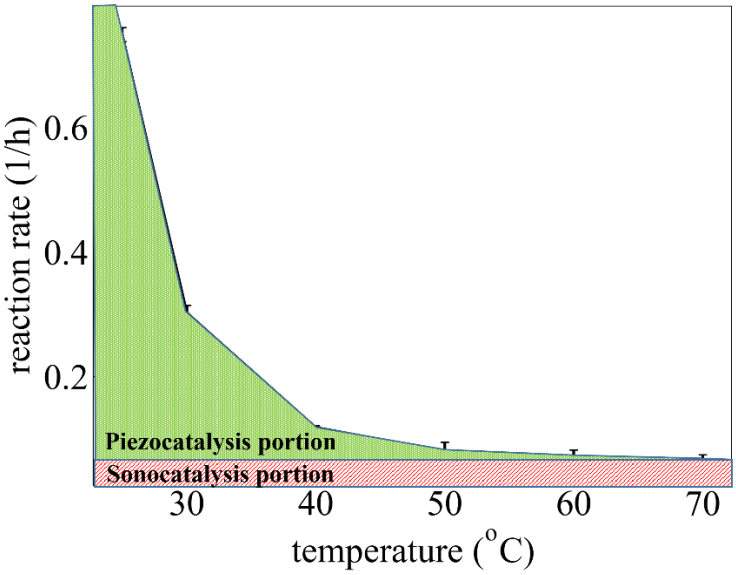

Fig. 4- 21 The contribution of the piezoelectric effect in the dye degradation catalytic reaction of $BaTiO_3$ with the size of 50 nm.

Finally, it is important to discuss more in detail the origin of the degradation of organic dyes in water produced by effect of ultrasonic waves. As discussed in this thesis, together with sonocatalysis, ultrasonic waves generate, via the piezoelectric effect, a piezopotential across the piezoelectric particles used as catalyst, which in turn may produce free radicals in the solution containing the organic dyes as the electric field generated exceeds the breakdown voltage. It must be emphasized here that the piezoelectric effect inside the catalyst crystal only produces *bound* charges at the internal surface of the piezoelectric particles, unlike in the case of photocatalysis, where *free* charges are produced that are transferred to the solution. These bound charges, *via the electric field* they produce, interact with the free charges that are available in the solution, outside of the solid piezoelectric catalyst surface (more precisely within the Helmholtz double layer). Provided they have enough energy, these free charges, in turn, produce free

radicals. Under steady state conditions, these free radicals present in the Helmholtz double layer promote catalytic reactions similarly to the cases of photocatalysis or electrocatalysis [50]. The complex nature of the system, which includes ultrasound as well as shock waves produced by cavitation, causes the free radicals to continuously move within the double layer and eventually diffuse towards the organic dyes (the model contaminant agent) in the solution. In an ideal piezocatalysis system, where there are no free charges on the piezocatalyst surface, the production of free radicals within the Helmholtz double layer and their motion towards the diffuse layer and the bulk of the solution is the sole origin of the catalytic reaction. Moreover, in a non-ideal and not perfectly insulating piezocatalysis system, where some free electrons are present, some charge transfer to the electrolyte is possible, complexifying the catalytic process, possibly enhancing the catalytic reaction. To achieve optimal piezocatalysis performance and maximize efficiency, all these factors should be considered.

Chapter 5

Conclusions and Perspectives

5-1 Conclusions

In this research, we introduced some approaches to discriminate between piezocatalysis and other possible catalytic reactions such as sonocatalysis and/or tribocatalysis, which are likely to occur simultaneously during the degradation of organic dyes using $BaTiO_3$ catalysts. The first approach was to investigate and compare the catalytic activities of piezoelectric $BaTiO_3$ and non-piezoelectric TiO_2 nanopowders during ultrasonication experiments where organic dyes dissolved in water were catalytically degraded using an ultrasonic bath. It has been assumed that half the free surfaces of the $BaTiO_3$ particles were BaO- terminated and the other half TiO_2 terminated, and that only the TiO_2-terminated free surfaces were catalytically active. It has also been assumed that, with the same particles size, structure and morphology, the non-piezoelectric part of the catalytic activity of the TiO_2-terminated surfaces of $BaTiO_3$ particles is similar to the catalytic activity of TiO_2 particles. Using free radical scavenger experiments, the active species in the catalytic reactions of organic dyes degradation were identified to be electrons and holes that lead to the generation of •OH and $\bullet O_2^-$ radicals. A catalytic reaction pathway has been

proposed based on the intermediate products identified with liquid chromatography – mass spectrometry (LC-MS). Kinetic studies of the catalytic reactions for both $BaTiO_3$ and TiO_2 at different temperatures also revealed that the former decreased while the latter increased when the temperature of the ultrasonic bath increased, suggesting a different origin of the catalytic reaction in these two materials. With the low concentrations of particle catalysts chosen in our experiments, it has been shown that the triboelectric effect is negligible, ruling out any contribution of tribocatalysis. The catalytic activity of TiO_2 was entirely attributed to sonocatalysis, whereas the $BaTiO_3$ catalytic activity was shown to have both sonocatalytic and piezocatalytic contributions (Figure 5-1). Comparing the catalytic reaction kinetics of $BaTiO_3$ and TiO_2, our simple model, which postulate that the sonocatalytic contribution of the active free surfaces of $BaTiO_3$ (i.e. the TiO_2-terminated surfaces) is very similar to that of TiO_2, allowed us to estimate the contribution of the pure piezocatalytic activity of $BaTiO_3$, which was found to be around 90% of the overall catalytic activity at room temperature. These results can then be extrapolated to estimate the contribution of the piezoelectric properties to the catalytic activity of any non-centrosymmetric nanocatalysts.

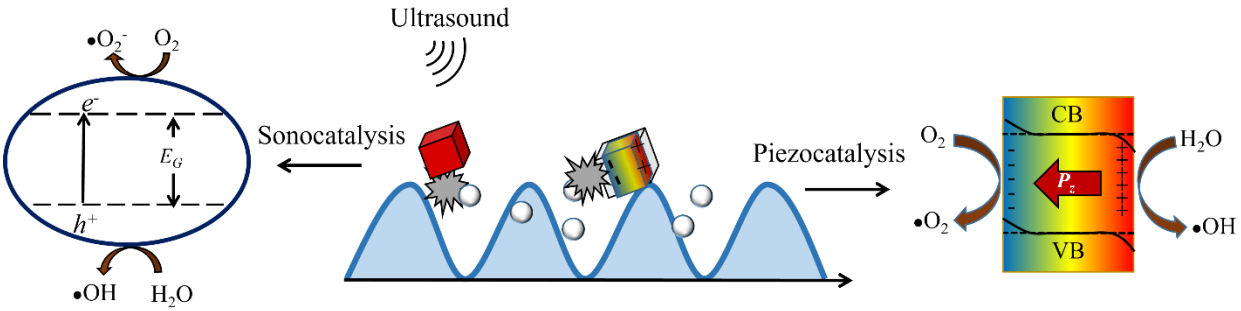

Fig. 5- 1 The mechanism of piezocatalysis and sonocatalysis that occur simultaneously at the same time in an ultrasonic bath.

The second approach used to estimate the contribution of piezocatalysis to the overall catalytic activity of $BaTiO_3$ particles catalysts was to study at different temperatures the catalytic activities of $BaTiO_3$ particles having different sizes. Indeed, it is known that for particles of smaller sizes, the tetragonal distortion of the crystal structure decreases, as does the Curie temperature, at which the piezoelectric properties vanish. As for our first approach, the efficacy of the catalytic reaction of organic dyes degradation were determined by monitoring the optical absorption of the model pollutant, methyl orange (MO) in water after ultrasonication of the solution containing the

dispersed piezoelectric $BaTiO_3$ particle catalysts. A clear correlation has been found between the catalytic reaction rates for the degradation of the MO organic model pollutant and the tetragonal distortion of the $BaTiO_3$ crystal structure, the latter being known to be affected by the size of the particles. The temperature-dependent Raman spectroscopy measurements revealed that the tetragonal piezoelectric to cubic centrosymmetric and non-piezoelectric phase transition temperature of $BaTiO_3$ decreases from 124 ^oC for the quasi-bulk particles of 2 μm to 102 ^oC for the particles of 50 nm. The study also revealed that as the temperature rises, the catalytic reaction rates of $BaTiO_3$ to degrade the MO organic dye decreases, becoming very small as well as less temperature dependent around 70 °C. The catalytic activity behaviour with temperature is consistent with the temperature dependence of the dominant $BaTiO_3$ shear-force piezoelectric coefficient d_{15}, strongly suggesting that the dominant contribution to the catalytic activity below 70 °C is piezocatalysis. It is believed that above 70 °C, the piezoelectric potential generated across the particles by the ultrasonic vibrations is too weak to promote the catalytic reactions degrading MO for the smaller nanoparticles (Figure 5-2). The use of free radical scavengers suggested that the active species in the (piezo)catalytic reactions are holes and possibly superoxides, which may in turn generate hydroxyl radicals. Our findings show that, at temperatures below 70 °C, more than 90% of the catalytic reactions promoted by $BaTiO_3$ nanoparticles are closely related to the piezoelectric properties of $BaTiO_3$ and the piezopotential induced to the nanoparticles' surfaces and are thus mostly piezo-driven.

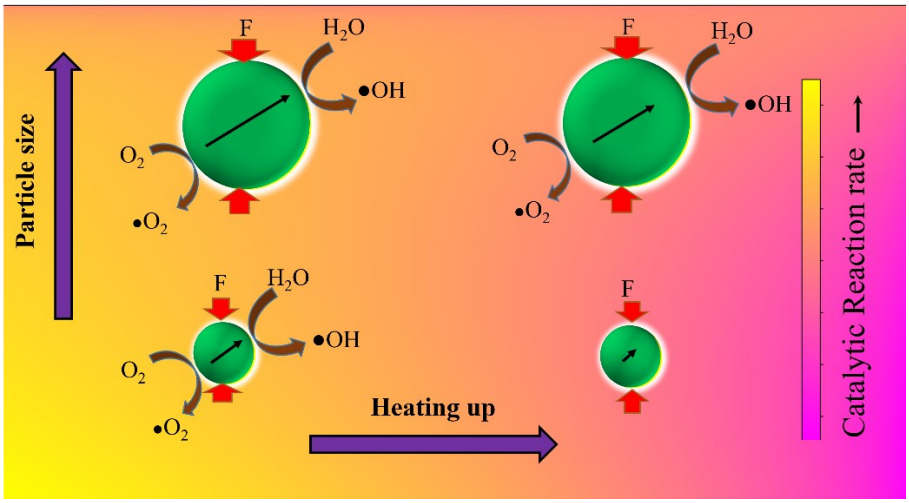

Fig. 5- 2 The summary results of the size and temperature effects on the piezocatalysis activities of $BaTiO_3$.

5-2 Perspectives of the Future works

Generally, the major perspective resulting from this work would be to develop, and design more efficient piezocatalysis systems. The development of more efficient materials, as well as engineering their morphology, size, and structures can enhance the piezopotential characteristics and improve the performance of piezocatalysis. Wastewater treatment using $BaTiO_3$ nanoparticle catalysts through a piezo-sonocatalysis process, which was investigated and documented in this research, is promising and shine some light on new aspects of the piezoelectric effect under-investigated so far. The temperature studies that have been performed in this research can also be further extended to different morphologies and sizes of $BaTiO_3$ particles. In the model that was proposed in this research, two piezoelectric and non-piezoelectric catalysts were compared together to determine the sonocatalysis contribution of the piezoelectric catalyst. These two catalysts should have the maximum morphology and structural similarities. Since the synthesis of very small size nanoparticles using microwave-assisted hydrothermal method has been reported in the literature, it should be possible to decrease the phase transition of $BaTiO_3$ further down, even as much as close to room temperature. This would allow the synthesis of both tetragonal and cubic $BaTiO_3$ at the same temperature, albeit in different sizes. The piezoelectric contribution of tetragonal $BaTiO_3$ vs. non-piezoelectric cubic $BaTiO_3$ could then be measured by manipulating the tetragonal phase transition temperature of $BaTiO_3$ using particle size control and comparing their catalytic response. Owing to the fact that the same material would be compared in both its piezoelectric and paraelectric phase, this method would be the most reliable approach to precisely and quantitatively determine the actual contribution of the piezoelectric properties to the catalytic process.

The approach and methodology used for our studies could be extended to other piezocatalyst candidates. To the best of our knowledge, ZnO, a piezoelectric material often reported to exhibit piezocatalystic properties, would be a good candidate for such an extension of our investigations. ZnO is a promising piezocatalyst semiconductor, not only due to its piezoelectric properties, but also due to its simple preparation, low cost, non-toxicity, good chemical stability, and strong redox ability. Like other II-VI compounds, ZnO possesses two possible crystal structures depending on the synthesis process: hexagonal wurtzite and cubic zinc blende. According to the literature, the wurtzite structure is the most stable phase in the ambient conditions. Due to its non-centrosymmetric structure, this phase is known to have piezoelectric and pyroelectric

properties. The piezocatalytic activity of this phase have been reported to have good efficiency for the degradation of anionic and cationic dyes. Because the zincblende phase is not piezoelectric, comparing its catalytic activities can provide useful information in distinguishing the sonocatalyst portion from the piezoresponse of the wurtzite phase. However, it should be noted here that the zincblende phase is difficult to synthesize. It is generally epitaxially stabilized in the thin film form when grown on appropriate cubic substrates. The synthesis of the piezoelectric ZnO phase as thin films can be worthwhile too, since it does enable accurate measurements of the piezoelectric coefficients for this phase using piezoresponse force microscopy (PFM). The fact that ZnO can be synthesized to be an insulator, a semiconductor, or a transparent conductive electrode, makes ZnO an ideal material to study the contributions and modes of action of the catalyst bound charges and free charges to the catalytic reactions.

References

[1] T. Yamamoto, H. Niori, and H. Moriwake, "Particle-size dependence of crystal structure of BaTiO3 powder," *Japanese Journal of Applied Physics,* vol. 39, no. 9S, p. 5683, 2000.

[2] S. Ramakanth and K. James Raju, "Band gap narrowing in $BaTiO_3$ nanoparticles facilitated by multiple mechanisms," *Journal of Applied Physics,* vol. 115, no. 17, p. 173507, 2014, doi: https://doi.org/10.1063/1.4871776.

[3] Q. Li and J. A. Lewis, "Nanoparticle inks for directed assembly of three-dimensional periodic structures," *Advanced Materials,* vol. 15, no. 19, pp. 1639-1643, 2003, doi: https://doi.org/10.1002/adma.200305413.

[4] D. Damjanovic, F. Brem, and N. Setter, "Crystal orientation dependence of the piezoelectric d_{33} coefficient in tetragonal $BaTiO_3$ as a function of temperature," *Applied physics letters,* vol. 80, no. 4, pp. 652-654, 2002, doi: https://doi.org/10.1063/1.1445481.

[5] T. Yamamoto, K. Urabe, and H. Banno, "$BaTiO_3$ particle-size dependence of ferroelectricity in $BaTiO_3$/polymer composites," *Japanese journal of applied physics,* vol. 32, no. 9S, p. 4272, 1993, doi: 10.1143/JJAP.32.4272.

[6] V. Buscaglia and C. A. Randall, "Size and scaling effects in barium titanate. An overview," *Journal of the European Ceramic Society,* vol. 40, no. 11, pp. 3744-3758, 2020, doi: https://doi.org/10.1016/j.jeurceramsoc.2020.01.021.

[7] K. Ishikawa, T. Nomura, N. O. N. Okada, and K. T. K. Takada, "Size effect on the phase transition in $PbTiO_3$ fine particles," *Japanese journal of applied physics,* vol. 35, no. 9S, p. 5196, 1996, doi: 10.1143/JJAP.35.5196

[8] I. C. Amaechi, R. Katoch, G. Kolhatkar, S. Sun, and A. Ruediger, "Particle size effect on the photocatalytic kinetics of barium titanate powders," *Catalysis Science & Technology,* vol. 10, no. 18, pp. 6274-6284, 2020.

[9] M. B. Smith *et al.*, "Crystal structure and the paraelectric-to-ferroelectric phase transition of nanoscale $BaTiO_3$," *Journal of the American Chemical Society,* vol. 130, no. 22, pp. 6955-6963, 2008, doi: https://doi.org/10.1021/ja0758436.

[10] Y. J. Jiang, L. Z. Zeng, R. P. Wang, Y. Zhu, and Y. L. Liu, "Fundamental and Second-Order Raman Spectra of $BaTiO_3$," *Journal of Raman spectroscopy,* vol. 27, no. 1, pp. 31-34, 1996, doi: https://doi.org/10.1002/(SICI)1097-4555(199601)27:1<31::AID-JRS920>3.0.CO;2-K.

[11] M. DiDomenico Jr, S. Wemple, S. Porto, and R. Bauman, "Raman spectrum of single-domain $BaTiO_3$," *Physical Review,* vol. 174, no. 2, p. 522, 1968, doi: https://doi.org/10.1103/PhysRev.174.522.

[12] J. Wu, W. Mao, Z. Wu, X. Xu, H. You, and Y. Jia, "Strong pyro-catalysis of pyroelectric BiFeO 3 nanoparticles under a room-temperature cold–hot alternation," *Nanoscale,* vol. 8, no. 13, pp. 7343-7350, 2016.

[13] J. Wu *et al.*, "Insights into the role of ferroelectric polarization in piezocatalysis of nanocrystalline $BaTiO_3$," *ACS applied materials & interfaces,* vol. 10, no. 21, pp. 17842-17849, 2018.

[14] H. Kalhori, A. H. Youssef, A. Ruediger, and A. Pignolet, "Competing Contributions to the Catalytic Activity of Barium Titanate Nanoparticles in the Decomposition of Organic Pollutants," *Journal of Environmental Chemical Engineering,* p. 108571, 2022, doi: https://doi.org/10.1016/j.jece.2022.108571.

[15] J. Wang, B. Guo, X. Zhang, Z. Zhang, J. Han, and J. Wu, "Sonocatalytic degradation of methyl orange in the presence of TiO_2 catalysts and catalytic activity comparison of rutile and anatase," *Ultrasonics sonochemistry,* vol. 12, no. 5, pp. 331-337, 2005, doi: https://doi.org/10.1016/j.ultsonch.2004.05.002.

[16] Q. Liu *et al.*, "Piezo-photoelectronic coupling effect of $BaTiO_3$@ TiO_2 nanowires for highly concentrated dye degradation," *Nano Energy,* vol. 92, p. 106702, 2022, doi: https://doi.org/10.1016/j.nanoen.2021.106702.

[17] J. Kaur and S. Singhal, "Facile synthesis of ZnO and transition metal doped ZnO nanoparticles for the photocatalytic degradation of Methyl Orange," *Ceramics international,* vol. 40, no. 5, pp. 7417-7424, 2014, doi: https://doi.org/10.1016/j.ceramint.2013.12.088.
[18] B. Yuan, J. Wu, N. Qin, E. Lin, and D. Bao, "Enhanced piezocatalytic performance of (Ba, Sr) TiO_3 nanowires to degrade organic pollutants," *ACS Applied Nano Materials,* vol. 1, no. 9, pp. 5119-5127, 2018, doi: https://doi.org/10.1021/acsanm.8b01206.
[19] J. Wu, N. Qin, and D. Bao, "Effective enhancement of piezocatalytic activity of $BaTiO_3$ nanowires under ultrasonic vibration," *Nano Energy,* vol. 45, pp. 44-51, 2018, doi: https://doi.org/10.1016/j.nanoen.2017.12.034.
[20] W. Qian, W. Yang, Y. Zhang, C. R. Bowen, and Y. Yang, "Piezoelectric materials for controlling electro-chemical processes," *Nano-Micro Letters,* vol. 12, no. 1, pp. 1-39, 2020, doi: https://doi.org/10.1007/s40820-020-00489-z.
[21] A. Devonshire, "CIX. Theory of barium titanate—Part II," *The London, Edinburgh, and Dublin Philosophical Magazine and Journal of Science,* vol. 42, no. 333, pp. 1065-1079, 1951, doi: https://doi.org/10.1080/14786445108561354.
[22] D. Damjanovic, F. Brem, and N. Setter, "Crystal orientation dependence of the piezoelectric d 33 coefficient in tetragonal BaTiO 3 as a function of temperature," *Applied physics letters,* vol. 80, no. 4, pp. 652-654, 2002.
[23] C. Zhao, Y. Huang, and J. Wu, "Multifunctional barium titanate ceramics via chemical modification tuning phase structure," *InfoMat,* vol. 2, no. 6, pp. 1163-1190, 2020, doi: https://doi.org/10.1002/inf2.12147.
[24] K. Tanaka, K. Suzuki, D. Fu, K. Nishizawa, T. Miki, and K. Kato, "Grain size effect on dielectric and piezoelectric properties of alkoxy-derived $BaTiO_3$-based thin films," *Japanese journal of applied physics,* vol. 43, no. 9S, p. 6525, 2004, doi: 10.1143/JJAP.43.6525.
[25] H. Takahashi, Y. Numamoto, J. Tani, and S. Tsurekawa, "Piezoelectric properties of $BaTiO_3$ ceramics with high performance fabricated by microwave sintering," *Japanese journal of applied physics,* vol. 45, no. 9S, p. 7405, 2006, doi: 10.1143/JJAP.45.7405.
[26] Y. Liu, S. Shrestha, and W. E. Mustain, "Synthesis of nanosize tungsten oxide and its evaluation as an electrocatalyst support for oxygen reduction in acid media," *ACS Catalysis,* vol. 2, no. 3, pp. 456-463, 2012, doi: https://doi.org/10.1021/cs200657w.
[27] P. Li *et al.*, "Strong tribocatalytic dye decomposition through utilizing triboelectric energy of barium strontium titanate nanoparticles," *Nano Energy,* vol. 63, p. 103832, 2019, doi: https://doi.org/10.1016/j.nanoen.2019.06.028.
[28] M. Zhou, H. Yang, T. Xian, R. Li, H. Zhang, and X. Wang, "Sonocatalytic degradation of RhB over LuFeO3 particles under ultrasonic irradiation," *Journal of hazardous materials,* vol. 289, pp. 149-157, 2015.
[29] P. C. Van Metre, D. A. Alvarez, B. J. Mahler, L. Nowell, M. Sandstrom, and P. Moran, "Complex mixtures of Pesticides in Midwest US streams indicated by POCIS time-integrating samplers," *Environmental Pollution,* vol. 220, pp. 431-440, 2017.
[30] A. A. Godoy, F. Kummrow, and P. A. Z. Pamplin, "Occurrence, ecotoxicological effects and risk assessment of antihypertensive pharmaceutical residues in the aquatic environment-A review," *Chemosphere,* vol. 138, pp. 281-291, 2015.
[31] "Pharmaceuticals in Drinking-Water," *World Health Organization: France,* 2012.
[32] F. A. Caliman and M. Gavrilescu, "Pharmaceuticals, personal care products and endocrine disrupting agents in the environment–a review," *CLEAN–Soil, Air, Water,* vol. 37, no. 4-5, pp. 277-303, 2009.
[33] E. R. Jones, M. T. van Vliet, M. Qadir, and M. F. Bierkens, "Country-level and gridded estimates of wastewater production, collection, treatment and reuse," *Earth System Science Data,* vol. 13, no. 2, pp. 237-254, 2021.

[34] G. Singh, M. Sharma, and R. Vaish, "Transparent ferroelectric glass–ceramics for wastewater treatment by piezocatalysis," *Communications Materials,* vol. 1, no. 1, pp. 1-8, 2020, doi: https://doi.org/10.1038/s43246-020-00101-2.
[35] R. Djellabi, M. F. Ordonez, F. Conte, E. Falletta, C. L. Bianchi, and I. Rossetti, "A review of advances in multifunctional XTiO3 perovskite-type oxides as piezo-photocatalysts for environmental remediation and energy production," *Journal of Hazardous Materials,* vol. 421, p. 126792, 2022.
[36] K.-S. Hong, H. Xu, H. Konishi, and X. Li, "Direct water splitting through vibrating piezoelectric microfibers in water," *The journal of physical chemistry letters,* vol. 1, no. 6, pp. 997-1002, 2010.
[37] M. Karaca, M. Kıranşan, S. Karaca, A. Khataee, and A. Karimi, "Sonocatalytic removal of naproxen by synthesized zinc oxide nanoparticles on montmorillonite," *Ultrasonics sonochemistry,* vol. 31, pp. 250-256, 2016, doi: https://doi.org/10.1016/j.ultsonch.2016.01.009.
[38] V. Paramarta, Y. Kristianto, A. Taufik, and R. Saleh, "Improve sonocatalytic performance using modified semiconductor catalyst SnO_2 and ZrO_2 by magnetite materials," in *IOP Conference Series: Materials Science and Engineering*, 2017, vol. 188, no. 1: IOP Publishing, p. 012042, doi: https://doi.org/10.1088/1757-899X/188/1/012042.
[39] E. Brillas and C. A. Martínez-Huitle, "Decontamination of wastewaters containing synthetic organic dyes by electrochemical methods. An updated review," *Applied Catalysis B: Environmental,* vol. 166, pp. 603-643, 2015.
[40] A. Fujishima, K. Honda, and S. Kikuchi, "Kogyo Kagaku Zasshi," 1969.
[41] H. Liu, C. Wang, and G. Wang, "Photocatalytic advanced oxidation processes for water treatment: recent advances and perspective," *Chemistry–An Asian Journal,* vol. 15, no. 20, pp. 3239-3253, 2020.
[42] R. Andreozzi, V. Caprio, A. Insola, and R. Marotta, "Advanced oxidation processes (AOP) for water purification and recovery," *Catalysis today,* vol. 53, no. 1, pp. 51-59, 1999.
[43] A. Hassani, A. Khataee, S. Karaca, C. Karaca, and P. Gholami, "Sonocatalytic degradation of ciprofloxacin using synthesized TiO2 nanoparticles on montmorillonite," *Ultrasonics sonochemistry,* vol. 35, pp. 251-262, 2017.
[44] E. B. Flint and K. S. Suslick, "The temperature of cavitation," *Science,* vol. 253, no. 5026, pp. 1397-1399, 1991, doi: https://doi.org/10.1126/science.253.5026.1397.
[45] D. Li, G. Wu, G. Gao, J. Shen, and F. Huang, "Ultrafast coloring-bleaching performance of nanoporous WO_3–SiO_2 gasochromic films doped with Pd catalyst," *ACS Applied Materials & Interfaces,* vol. 3, no. 12, pp. 4573-4579, 2011, doi: https://doi.org/10.1021/am200781e.
[46] P. Gholami, A. Khataee, R. D. C. Soltani, and A. Bhatnagar, "A review on carbon-based materials for heterogeneous sonocatalysis: fundamentals, properties and applications," *Ultrasonics Sonochemistry,* vol. 58, p. 104681, 2019.
[47] M. Dastborhan, A. Khataee, S. Arefi-Oskoui, and Y. Yoon, "Synthesis of flower-like MoS2/CNTs nanocomposite as an efficient catalyst for the sonocatalytic degradation of hydroxychloroquine," *Ultrasonics Sonochemistry,* p. 106058, 2022.
[48] Y. L. Pang and A. Z. Abdullah, "Comparative study on the process behavior and reaction kinetics in sonocatalytic degradation of organic dyes by powder and nanotubes TiO2," *Ultrasonics sonochemistry,* vol. 19, no. 3, pp. 642-651, 2012.
[49] E. Weidner, E. Karbassiyazdi, A. Altaee, T. Jesionowski, and F. Ciesielczyk, "Hybrid Metal Oxide/Biochar Materials for Wastewater Treatment Technology: A Review," *ACS omega,* vol. 7, no. 31, pp. 27062-27078, 2022.
[50] M. B. Starr and X. Wang, "Fundamental analysis of piezocatalysis process on the surfaces of strained piezoelectric materials," *Scientific reports,* vol. 3, no. 1, pp. 1-8, 2013, doi: https://doi.org/10.1038/srep02160.
[51] X. Cui *et al.*, "Greatly enhanced tribocatalytic degradation of organic pollutants by TiO2 nanoparticles through efficiently harvesting mechanical energy," *Separation and Purification Technology,* vol. 289, p. 120814, 2022.

[52] B. Yang *et al.*, "Insights into the tribo-/pyro-catalysis using Sr-doped BaTiO3 ferroelectric nanocrystals for efficient water remediation," *Chemical Engineering Journal,* vol. 416, p. 128986, 2021.
[53] B. Yang *et al.*, "Enhanced tribocatalytic degradation using piezoelectric CdS nanowires for efficient water remediation," *Journal of Materials Chemistry C,* vol. 8, no. 42, pp. 14845-14854, 2020.
[54] K. Nakata and A. Fujishima, "TiO2 photocatalysis: Design and applications," *Journal of photochemistry and photobiology C: Photochemistry Reviews,* vol. 13, no. 3, pp. 169-189, 2012.
[55] R. Berenguer, J. M. Sieben, C. Quijada, and E. Morallón, "Electrocatalytic degradation of phenol on Pt-and Ru-doped Ti/SnO_2-Sb anodes in an alkaline medium," *Applied Catalysis B: Environmental,* vol. 199, pp. 394-404, 2016, doi: https://doi.org/10.1016/j.apcatb.2016.06.038.
[56] S. Rachmilovich-Calis, A. Masarwa, N. Meyerstein, D. Meyerstein, and R. Van Eldik, "New mechanistic aspects of the Fenton reaction," *Chemistry–A European Journal,* vol. 15, no. 33, pp. 8303-8309, 2009.
[57] M. Wang *et al.*, "Remarkably enhanced hydrogen generation of organolead halide perovskites via piezocatalysis and photocatalysis," *Advanced Energy Materials,* vol. 9, no. 37, p. 1901801, 2019.
[58] P. Zhu, Y. Chen, and J. Shi, "Piezocatalytic tumor therapy by ultrasound-triggered and $BaTiO_3$-mediated piezoelectricity," *Advanced Materials,* vol. 32, no. 29, p. 2001976, 2020, doi: https://doi.org/10.1002/adma.202001976.
[59] Y. Wang *et al.*, "Piezo-catalysis for nondestructive tooth whitening," *Nature communications,* vol. 11, no. 1, pp. 1-11, 2020, doi: https://doi.org/10.1038/s41467-020-15015-3.
[60] R. Su *et al.*, "Strain-Engineered Nano-Ferroelectrics for High-Efficiency Piezocatalytic Overall Water Splitting," *Angewandte Chemie International Edition,* vol. 60, no. 29, pp. 16019-16026, 2021.
[61] C. A. Martínez-Huitle and L. S. Andrade, "Electrocatalysis in wastewater treatment: recent mechanism advances," *Quimica Nova,* vol. 34, pp. 850-858, 2011.
[62] X. Wang, "Piezoelectric nanogenerators—Harvesting ambient mechanical energy at the nanometer scale," *Nano Energy,* vol. 1, no. 1, pp. 13-24, 2012.
[63] J. Bard Allen and R. Faulkner Larry, "Electrochemical methods: fundamentals and applications," ed: Wiley New York, 2001.
[64] J. Wu, W. Wang, Y. Tian, C. Song, H. Qiu, and H. Xue, "Piezotronic effect boosted photocatalytic performance of heterostructured BaTiO3/TiO2 nanofibers for degradation of organic pollutants," *Nano Energy,* vol. 77, p. 105122, 2020.
[65] S. V. Kalinin and D. A. Bonnell, "Screening phenomena on oxide surfaces and its implications for local electrostatic and transport measurements," *Nano Letters,* vol. 4, no. 4, pp. 555-560, 2004.
[66] K. Wenderich and G. Mul, "Methods, mechanism, and applications of photodeposition in photocatalysis: a review," *Chemical reviews,* vol. 116, no. 23, pp. 14587-14619, 2016.
[67] S. Tu *et al.*, "Piezocatalysis and piezo-photocatalysis: catalysts classification and modification strategy, reaction mechanism, and practical application," *Advanced Functional Materials,* vol. 30, no. 48, p. 2005158, 2020, doi: https://doi.org/10.1002/adfm.202005158.
[68] X. Huang *et al.*, "Insight into the piezo-photo coupling effect of PbTiO3/CdS composites for piezo-photocatalytic hydrogen production," *Applied Catalysis B: Environmental,* vol. 282, p. 119586, 2021.
[69] J. M. Wu, W. E. Chang, Y. T. Chang, and C. K. Chang, "Piezo-catalytic effect on the enhancement of the ultra-high degradation activity in the dark by single-and few-layers MoS2 nanoflowers," *Advanced Materials,* vol. 28, no. 19, pp. 3718-3725, 2016.
[70] P. Wang *et al.*, "Impact of oxygen vacancy occupancy on piezo-catalytic activity of BaTiO3 nanobelt," *Applied Catalysis B: Environmental,* vol. 279, p. 119340, 2020.

[71] C. Hu *et al.*, "Exceptional cocatalyst-free photo-enhanced piezocatalytic hydrogen evolution of carbon nitride nanosheets from strong in-plane polarization," *Advanced Materials,* vol. 33, no. 24, p. 2101751, 2021.
[72] W. Tian *et al.*, "Efficient piezocatalytic removal of BPA and Cr (VI) with SnS2/CNFs membrane by harvesting vibration energy," *Nano Energy,* vol. 86, p. 106036, 2021.
[73] K. S. Suslick, S. Doktycz, and E. Flint, "On the origin of sonoluminescence and sonochemistry," *Ultrasonics,* vol. 28, no. 5, pp. 280-290, 1990.
[74] A. Zhang *et al.*, "Vibration catalysis of eco-friendly Na0. 5K0. 5NbO3-based piezoelectric: an efficient phase boundary catalyst," *Applied Catalysis B: Environmental,* vol. 279, p. 119353, 2020.
[75] J. Shi *et al.*, "Piezocatalytic foam for highly efficient degradation of aqueous organics," *Small Science,* vol. 1, no. 2, p. 2000011, 2021.
[76] Y. Wei, Y. Zhang, W. Geng, H. Su, and M. Long, "Efficient bifunctional piezocatalysis of Au/BiVO4 for simultaneous removal of 4-chlorophenol and Cr (VI) in water," *Applied Catalysis B: Environmental,* vol. 259, p. 118084, 2019.
[77] R. Su *et al.*, "Nano-ferroelectric for high efficiency overall water splitting under ultrasonic vibration," *Angewandte Chemie International Edition,* vol. 58, no. 42, pp. 15076-15081, 2019.
[78] D. Shao, L. Zhang, S. Sun, and W. Wang, "Oxygen Reduction Reaction for Generating H2O2 through a Piezo-Catalytic Process over Bismuth Oxychloride," *ChemSusChem,* vol. 11, no. 3, pp. 527-531, 2018.
[79] I. Amaechi, A. Hadj Youssef, A. Dörfler, Y. Gonzalez, R. Katoch, and A. Ruediger, "Catalytic Applications of Non-Centrosymmetric Oxide Nanomaterials," *Angewandte Chemie*.
[80] M. A. Ainslie and J. G. McColm, "A simplified formula for viscous and chemical absorption in sea water," *The Journal of the Acoustical Society of America,* vol. 103, no. 3, pp. 1671-1672, 1998.
[81] Y. Zheng *et al.*, "Sm-Doped (1–x) Pb (Mg1/3Nb2/3) O_{3-x} PbTiO3 Nanostructures for Piezocatalytic Dye Degradation," *ACS Applied Nano Materials,* vol. 5, no. 1, pp. 277-287, 2021.
[82] V. Hasija *et al.*, "Recent advances in noble metal free doped graphitic carbon nitride based nanohybrids for photocatalysis of organic contaminants in water: a review," *Applied Materials Today,* vol. 15, pp. 494-524, 2019.
[83] K. Mistewicz, M. Kępińska, M. Nowak, A. Sasiela, M. Zubko, and D. Stróż, "Fast and efficient piezo/photocatalytic removal of methyl orange using SbSI nanowires," *Materials,* vol. 13, no. 21, p. 4803, 2020.
[84] S. Kumar Kuila, P. Kumbhakar, C. Sekhar Tiwary, and T. Kumar Kundu, "Photon and vibration synergism on planar defects induced 2D-graphitic carbon nitride for ultrafast remediation of dyes and antibiotic ampicillin," *Journal of Materials Science,* vol. 57, no. 19, pp. 8658-8675, 2022.
[85] Y. Fu *et al.*, "Synthesis of ternary ZnO/ZnS/MoS2 piezoelectric nanoarrays for enhanced photocatalytic performance by conversion of dual heterojunctions," *Applied Surface Science,* vol. 556, p. 149695, 2021.
[86] D. Hong *et al.*, "High piezo-photocatalytic efficiency of CuS/ZnO nanowires using both solar and mechanical energy for degrading organic dye," *ACS Applied Materials & Interfaces,* vol. 8, no. 33, pp. 21302-21314, 2016.
[87] S. Lan, C. Yu, E. Wu, M. Zhu, and D. D. Dionysiou, "Self-powered water flow-triggered piezocatalytic generation of reactive oxygen species for water purification in simulated water drainage," *ACS ES&T Engineering,* vol. 2, no. 1, pp. 101-109, 2021.
[88] Y. Wang *et al.*, "Ultrasonic activation of inert poly (tetrafluoroethylene) enables piezocatalytic generation of reactive oxygen species," *Nature communications,* vol. 12, no. 1, pp. 1-8, 2021.
[89] Y.-M. You *et al.*, "An organic-inorganic perovskite ferroelectric with large piezoelectric response," *Science,* vol. 357, no. 6348, pp. 306-309, 2017.
[90] A. Leguy *et al.*, "The dynamics of methylammonium ions in hybrid organic–inorganic perovskite solar cells," *Nature communications,* vol. 6, no. 1, pp. 1-11, 2015.

[91] J. Gao, D. Xue, W. Liu, C. Zhou, and X. Ren, "Recent progress on $BaTiO_3$-based piezoelectric ceramics for actuator applications," in *Actuators*, 2017, vol. 6, no. 3: Multidisciplinary Digital Publishing Institute, p. 24, doi: https://doi.org/10.3390/act6030024.
[92] M. Acosta *et al.*, "$BaTiO_3$-based piezoelectrics: Fundamentals, current status, and perspectives," *Applied Physics Reviews,* vol. 4, no. 4, p. 041305, 2017, doi: https://doi.org/10.1063/1.4990046.
[93] H.-Y. Tan, L. Zhan, C.-F. Yan, L. K. Abeykoon, N. L. De Silva, and J. Bandara, "Enhancement of the conversion of mechanical energy into chemical energy by using piezoelectric KNbO3− x with oxygen vacancies as a novel piezocatalyst," *Nano Express,* vol. 1, no. 3, p. 030036, 2020.
[94] H. You *et al.*, "Harvesting the vibration energy of BiFeO3 nanosheets for hydrogen evolution," *Angewandte Chemie,* vol. 131, no. 34, pp. 11905-11910, 2019.
[95] M. Ashokkumar, "The characterization of acoustic cavitation bubbles–an overview," *Ultrasonics sonochemistry,* vol. 18, no. 4, pp. 864-872, 2011.
[96] M. P. Brenner, S. Hilgenfeldt, and D. Lohse, "Single-bubble sonoluminescence," *Reviews of modern physics,* vol. 74, no. 2, p. 425, 2002.
[97] Z. L. Wang, "Catch wave power in floating nets," *Nature,* vol. 542, no. 7640, pp. 159-160, 2017.
[98] Y. Feng *et al.*, "Enhanced photocatalytic degradation performance by fluid-induced piezoelectric field," *Environmental science & technology,* vol. 52, no. 14, pp. 7842-7848, 2018.
[99] Y. Feng *et al.*, "Engineering spherical lead zirconate titanate to explore the essence of piezo-catalysis," *Nano Energy,* vol. 40, pp. 481-486, 2017.
[100] M. B. Starr, J. Shi, and X. Wang, "Piezopotential-driven redox reactions at the surface of piezoelectric materials," *Angewandte Chemie International Edition,* vol. 51, no. 24, pp. 5962-5966, 2012.
[101] D. Pletcher, *A first course in electrode processes*. Royal Society of Chemistry, 2019.
[102] S. Farhadi, Z. Momeni, and M. Taherimehr, "Rapid synthesis of perovskite-type LaFeO3 nanoparticles by microwave-assisted decomposition of bimetallic La [Fe (CN) 6]· 5H2O compound," *Journal of alloys and compounds,* vol. 471, no. 1-2, pp. L5-L8, 2009.
[103] C. Srilakshmi, R. Saraf, V. Prashanth, G. M. Rao, and C. Shivakumara, "Structure and catalytic activity of Cr-doped BaTiO3 nanocatalysts synthesized by conventional oxalate and microwave assisted hydrothermal methods," *Inorganic Chemistry,* vol. 55, no. 10, pp. 4795-4805, 2016.
[104] G. Canu and V. Buscaglia, "Hydrothermal synthesis of strontium titanate: thermodynamic considerations, morphology control and crystallisation mechanisms," *CrystEngComm,* vol. 19, no. 28, pp. 3867-3891, 2017.
[105] S. H. Jhung, J.-S. Chang, J. S. Hwang, and S.-E. Park, "Selective formation of SAPO-5 and SAPO-34 molecular sieves with microwave irradiation and hydrothermal heating," *Microporous and Mesoporous Materials,* vol. 64, no. 1-3, pp. 33-39, 2003.
[106] B. Cullity, S. Stock, and S. Stock, "Elements of X-ray Diffraction, 3rd editionPrentice Hall," *New Jersey,* 2001.
[107] G. S. Bumbrah and R. M. Sharma, "Raman spectroscopy–Basic principle, instrumentation and selected applications for the characterization of drugs of abuse," *Egyptian Journal of Forensic Sciences,* vol. 6, no. 3, pp. 209-215, 2016.
[108] F. Settle, "Handbook of instrumental techniques for analytical chemistry, 1/e, National Science Foundation, Arlington, Virginia Published June, 1997 by Prentice Hall PTR (ECS Professional)," *Cloth ISBN 0-13-177338-0,* 1997.
[109] D. A. Skoog, F. J. Holler, and S. R. Crouch, *Principles of instrumental analysis*. Cengage learning, 2017.
[110] D. Cialla-May, M. Schmitt, and J. Popp, "Theoretical principles of Raman spectroscopy," *Physical Sciences Reviews,* vol. 4, no. 6, 2019.
[111] E. Smith and G. Dent, *Modern Raman spectroscopy: a practical approach*. John Wiley & Sons, 2019.
[112] B. Schrader, *Infrared and Raman spectroscopy: methods and applications*. John Wiley & Sons, 2008.

[113] J. Kawai, H. Adachi, Y. Kitajima, K. MAEDA, S. HAYAKAWA, and Y. GoHSHI, "Inelastic mean free path of photoelectrons in Ag determined by total reflection X-ray photoelectron spectroscopy," *Analytical sciences,* vol. 13, no. 5, pp. 797-801, 1997.
[114] K. V. Kumar, K. Porkodi, and Rocha, "Langmuir–Hinshelwood kinetics–a theoretical study," *Catalysis Communications,* vol. 9, no. 1, pp. 82-84, 2008.
[115] M. Yashima *et al.*, "Size effect on the crystal structure of barium titanate nanoparticles," *Journal of applied physics,* vol. 98, no. 1, p. 014313, 2005, doi: https://doi.org/10.1063/1.1935132.
[116] T. Hoshina, S. Wada, Y. Kuroiwa, and T. Tsurumi, "Composite structure and size effect of barium titanate nanoparticles," *Applied Physics Letters,* vol. 93, no. 19, p. 192914, 2008, doi: https://doi.org/10.1063/1.3027067.
[117] T.-C. Huang, M.-T. Wang, H.-S. Sheu, and W.-F. Hsieh, "Size-dependent lattice dynamics of barium titanate nanoparticles," *Journal of Physics: Condensed Matter,* vol. 19, no. 47, p. 476212, 2007, doi: https://doi.org/10.1088/0953-8984/19/47/476212.
[118] M. DiDomenico Jr, S. Wemple, S. Porto, and R. Bauman, "Raman spectrum of single-domain BaTi O 3," *Physical Review,* vol. 174, no. 2, p. 522, 1968.
[119] F. A. Rabuffetti and R. L. Brutchey, "Structural evolution of $BaTiO_3$ nanocrystals synthesized at room temperature," *Journal of the American Chemical Society,* vol. 134, no. 22, pp. 9475-9487, 2012, doi: https://doi.org/10.1021/ja303184w.
[120] I. C. Amaechi, A. Hadj Youssef, D. Rawach, J. P. Claverie, S. Sun, and A. Ruediger, "Ferroelectric Fe–Cr codoped $BaTiO_3$ nanoparticles for the photocatalytic oxidation of azo dyes," *ACS Applied Nano Materials,* vol. 2, no. 5, pp. 2890-2901, 2019, doi: https://doi.org/10.1021/acsanm.9b00336.
[121] J. L. Bribes, M. El Boukari, and J. Maillols, "Application of Raman spectroscopy to industrial membranes. Part 2–Perfluorosulphonic membrane," *Journal of Raman spectroscopy,* vol. 22, no. 5, pp. 275-279, 1991, doi: https://doi.org/10.1002/jrs.1250220507.
[122] T. Ohsaka, F. Izumi, and Y. Fujiki, "Raman spectrum of anatase, TiO_2," *Journal of Raman spectroscopy,* vol. 7, no. 6, pp. 321-324, 1978, doi: https://doi.org/10.1002/jrs.1250070606.
[123] F. Bößl and I. Tudela, "Piezocatalysis–Can catalysts really dance?," *Current Opinion in Green and Sustainable Chemistry,* p. 100537, 2021, doi: https://doi.org/10.1016/j.cogsc.2021.100537.
[124] M. F. Kabir, E. Vaisman, C. H. Langford, and A. Kantzas, "Effects of hydrogen peroxide in a fluidized bed photocatalytic reactor for wastewater purification," *Chemical Engineering Journal,* vol. 118, no. 3, pp. 207-212, 2006.
[125] A. M. Silva, E. Nouli, N. P. Xekoukoulotakis, and D. Mantzavinos, "Effect of key operating parameters on phenols degradation during H2O2-assisted TiO2 photocatalytic treatment of simulated and actual olive mill wastewaters," *Applied Catalysis B: Environmental,* vol. 73, no. 1-2, pp. 11-22, 2007.
[126] J. Lee *et al.*, "A micro-fabricated force sensor using an all thin film piezoelectric active sensor," *Sensors,* vol. 14, no. 12, pp. 22199-22207, 2014, doi: https://doi.org/10.3390/s141222199.
[127] J. Cao *et al.*, "Strong tribocatalysis of strontium titanate nanofibers through harvesting friction energy for dye decomposition," *Ceramics International,* vol. 48, no. 7, pp. 9651-9657, 2022, doi: https://doi.org/10.1016/j.ceramint.2021.12.164.
[128] C. Sun *et al.*, "Strong tribocatalytic dye degradation by tungsten bronze $Ba_4Nd_2Fe_2Nb_8O_{30}$," *Ceramics International,* vol. 47, no. 4, pp. 5038-5043, 2021.
[129] H. Lei *et al.*, "Tribo-catalytic degradation of organic pollutants through bismuth oxyiodate triboelectrically harvesting mechanical energy," *Nano Energy,* vol. 78, p. 105290, 2020, doi: https://doi.org/10.1016/j.nanoen.2020.105290.
[130] Y. Su *et al.*, "Enhanced photodegradation of methyl orange with TiO_2 nanoparticles using a triboelectric nanogenerator," *Nanotechnology,* vol. 24, no. 29, p. 295401, 2013, doi: https://doi.org/10.1088/0957-4484/24/29/295401.

[131] C. Wu, A. C. Wang, W. Ding, H. Guo, and Z. L. Wang, "Triboelectric nanogenerator: a foundation of the energy for the new era," *Advanced Energy Materials,* vol. 9, no. 1, p. 1802906, 2019, doi: https://doi.org/10.1002/aenm.201802906.

[132] Y. Shiratori, C. Pithan, J. Dornseiffer, and R. Waser, "Raman scattering studies on nanocrystalline $BaTiO_3$ Part II—consolidated polycrystalline ceramics," *Journal of Raman Spectroscopy: An International Journal for Original Work in all Aspects of Raman Spectroscopy, Including Higher Order Processes, and also Brillouin and Rayleigh Scattering,* vol. 38, no. 10, pp. 1300-1306, 2007, doi: https://doi.org/10.1002/jrs.1763.

[133] W.-L. Zhong, B. Jiang, P. Zhang, J. Ma, H. Cheng, and Z. Yang, "Phase transition in $PbTiO_3$ ultrafine particles of different sizes," *Journal of Physics: Condensed Matter,* vol. 5, no. 16, p. 2619, 1993, doi: 10.1088/0953-8984/5/16/018.

[134] F. Huang, G. Mankey, M. Kief, and R. Willis, "Finite-size scaling behavior of ferromagnetic thin films," *Journal of applied physics,* vol. 73, no. 10, pp. 6760-6762, 1993, doi: https://doi.org/10.1063/1.352477.

[135] C. Yang and Q. Jiang, "Size and interface effects on critical temperatures of ferromagnetic, ferroelectric and superconductive nanocrystals," *Acta Materialia,* vol. 53, no. 11, pp. 3305-3311, 2005, doi: https://doi.org/10.1016/j.actamat.2005.03.039.